PLASMA RESISTIVITY MEASUREMENTS

IN THE WISCONSIN LEVITATED OCTUPOLE

by

David Allen Brouchous

A thesis submitted in partial fulfillment of the

requirements for the degree of

DOCTOR OF PHILOSOPHY

(Physics)

at the

University of Wisconsin

1979

PLASMA RESISTIVITY MEASUREMENTS

IN THE WISCONSIN LEVITATED OCTUPOLE

David Allen Brouchous

(Under the supervision of Professor Donald W. Kerst)

Resistivity measurements parallel to the magnetic field were made on gun injected plasmas ranging in density from 10^9 cm^{-3} to 10^{12} cm^{-3} in the Wisconsin levitated octupole with toroidal and poloidal magnetic fields. The 10^9 cm^{-3} plasma was collisionless with $\lambda_{mfp} > 100$ mirror lengths, had $T_e = 10$ eV, $T_i = 30$ eV and was found to have anomalous resistivity scaling like $\eta = \sqrt{T_e}/n_e$ when $E_\parallel > E_c$ where E_c is the Dreicer critical field. The 10^{12} cm^{-3} plasma was collisional with $\lambda_{mfp} <$ mirror length, had $T_e = T_i \approx .2$ eV and was found to have Spitzer resistivity when $E_\parallel < E_c$.

The inductive electric field parallel to the magnetic field lines was calculated and was used to investigate single particle motion of trapped and circulating particles in the octupole geometry. The calculated $E_\parallel$ was used to determine plasma resistivity from the measured value of $J_\parallel/B$ on a flux surface.

Plasma densities and electron temperatures were measured with Langmuir probes. Ion temperatures were measured with skimmer probes which allowed local measurements in the high field bridge region. An E x B energy analyzer was developed for measuring electron velocity

distributions. Current and density fluctuations were observed in the low density plasmas which exhibited anomalous resistivity. ω and k measurements of the fluctuations are best explained as ion Bernstein modes and current-driven drift waves.

Small angle electron-wave scattering was examined in the presence of deep magnetic mirrors and was found to extend the range of applicability of Plateau resistivity determined from neoclassical transport theory. The anomalous resistivity observed in the low density plasmas agrees in scaling and magnitude with Plateau resistivity.

Donald M. Karfunkel

Table of Contents

Chapter I

Introduction

Plasma resistivity in an octupole geometry has been studied by University of Wisconsin plasma researchers since the 60's. Lencioni[1] noted anomalous resistivity scaling like $\eta \alpha \sqrt{T_e}/n_e$ in the little octupole filled with a gun injected plasma. Etzweiler[2] expanded the resistivity studies on the little octupole by using microwave generated plasmas which allowed a larger range of n_e and T_e to be examined. The big octupole results presented in this thesis were obtained at the same time as Etzweiler's work.

Until 1974 the big octupole and little octupole were linked by the $\sqrt{T_e}/n_e$ resistivity scaling and efforts were made to explain why this scaling should occur. Little octupole efforts were devoted mainly to extending the ranges of n_e, T_e, and machine parameters such as mirror length and electric field strength. Big octupole efforts were concentrated on the current and density fluctuations which were observed to accompany the anomalous resistivity.

In 1974 a new plasma gun (big gun) was installed on the big octupole which gave high density, low temperature plasmas which exhibited Spitzer resistivity. In 1976 another gun (intermediate gun) was installed on the big octupole which showed Spitzer resistivity at injection time and $\sqrt{T_e}/n_e$ resistivity 10 msec later. Current fluctuations were observed to turn on at the time of the switch from Spitzer to anomalous resistivity. The new plasma guns showed a connection between the

fluctuations (current-driven instabilities) and the anomalous resistivity, and also extended the parameter range of n_e and T_e scaling.

The scaling of the conductivity can be related to microscopic effects such as scattering of electrons off of other charged particles, scattering off of neutrals, scattering off of fluctuating electric fields, and trapping of electrons in certain regions of velocity space due to spatial variations in the confining magnetic field strength. The macroscopic effects of conductivity make it one of the most important transport properties of the plasma. The conductivity determines the amount of current which will flow in response to an applied electric field and thus how much energy can be added to the plasma by ohmic heating.

In order to calculate the ohmic heating power that can be coupled to a plasma one needs to know the applied electric field and the plasma conductivity. Neither of these quantities is simple to determine for the octupole geometry. The following chapters will hopefully acquaint the reader with some of the complexities which arise.

Chapters II, III, and IV contain descriptions of the experimental apparatus, plasma sources, and diagnostics which were used to study the conductivity. Chapter V explains the method used to calculate the inductive parallel electric fields. Chapter VI deals with the single particle motion in response to an applied electric field in an octupole geometry. Chapter VII is a review of theoretical conductivities and how they apply to the octupole. Chapter VIII is a summary of the conductivity measurements made on the octupole and the scaling of the conductivity versus density and electron temperature. Chapter IX reviews current

driven instabilities and their effects on plasma conductivity. Chapter X is a summary of fluctuations observed in the electron current. Chapter XI contains a summary of results and a possible explanation of the results in terms of a turbulent-mirror mechanism.

References for Chapter I

1. D. E. Lencioni, Univ. of Wisc. Ph.D. Thesis, PLP 276 (1969)

2. J. F. Etzweiler, Univ. of Wisc. Ph.D. Thesis, PLP 738 (1977)

Chapter II

Machine description

A. Wisconsin levitated octupole

Figure 1 is an illustration of the Wisconsin levitated octupole[1,2,3] on which the experiments to be described were performed. The confining magnetic field is produced by a 90:1 turn transformer. Four sets of primary windings are wound in series around the four legs of a 60 ton laminated iron core. The primary windings are interleaved with continuity windings which carry the wall image currents around the core so that the vacuum vessel does not link any magnetic flux. The secondary consists of four one turn secondary windings (hoops) in parallel which are contained inside the vacuum vessel. 700 kA of current is induced in the hoops at peak field when the B_p capacitor bank is initially charged to 2.5 kV. A summary of machine parameters is given in Table 1.

The hoop currents all flow in the same direction and produce the poloidal magnetic field illustrated in Figure 2. Figure 2a shows the lines of constant flux which are also the field lines. The field lines are labeled in Dory units[4] from 0 to 10 with the ψ=0 field line located at the hoop and the ψ=10 field line located at the wall. 10 Dory units are equal to the flux in Webers inside the machine. The flux is contained inside the vacuum vessel by image currents flowing in the wall. Because the walls have a finite resistivity the image currents are not able to perfectly image the flux at the walls and the flux is able to diffuse into the walls and hoops.[5]

The flux is divided into two regions, private and common. The private

flux circles only one hoop. The common flux circles all four hoops. The two regions are separated by the separatrix field line which is the dashed field line in Figure 2a.

Figure 2b shows lines of constant B_p magnitude. B_p=0 at each of three points on the midcylinder where the separatrix field lines cross. B_p increases in all directions from the field nulls. This magnetic configuration is referred to as a minimum B magnetic well.[6] The octupole has shown itself to be stable to the flute or interchange instability.[7] This is due to the favorable curvature of the field lines. Field lines curve in toward the plasma more than they curve out and thus satisfy the relation $\delta V<0$ in the direction of decreasing plasma density, where V is the volume of the flux tube. The last field line having average good curvature is called ψ_{crit} and is indicated by the dot-dash line in Figure 2a. ψ_{crit} satisfies the condition

$$\oint \frac{d\ell}{B} \geq 0 \qquad \text{increasing } \psi \text{ direction}$$

where the integral is taken once around in the poloidal direction.

B. Poloidal magnetic field

Figure 3a illustrates the poloidal field circuitry. The main .048 F capacitor bank may be charged as high as 5 kV when running in the sine wave mode but is normally charged to 2.5 kV. In the sine wave mode the poloidal magnetic field varies as a sine wave with a half period of 43 msec. In the crowbar mode the 6 F crowbar bank is fired at peak field (22 msec) and the magnetic field decays with a much longer period; τ=90

msec near the hoops to τ=150 msec on the midcylinder.[8]

C. Toroidal magnetic field

The octupole has a 40:1 turn toroidal transformer which drives current around the vacuum vessel the short way around in order to produce a toroidal magnetic field. The B_θ transformer may be driven in series with the poloidal field by opening switch S2 and closing switches S3 and S4 illustrated in Figure 3a. B_p and B_θ may then be run in series with the same time dependence, either sine wave or crowbarred. The B_θ field also has a separate capacitor bank and power crowbar which allows B_θ to operate independently of B_p. The B_θ circuit is illustrated in Figure 3b. The main bank may be charged as high as 400 Volts. The charge on the main bank is approximately equal to the B_θ field in Gauss on the midcylinder (i.e. 100 Volts ≈ 100 Gauss). 300 Volts on the B_θ bank produces approximately the same B_θ field as running B_p and B_θ in series with 2.5 kV on the B_p bank.

D. Sequencing of fields

Figure 4 illustrates field timing and gun injection. The poloidal and toroidal fields can be triggered independently. The normal operating mode is to trigger B_p and B_θ at the same time and crowbar at peak field as illustrated in Figure 4a. This mode gives long plasma confinement time and slowly changing magnetic fields. It is ideal for studying diffusion processes since plasma motion due to field line motion has been reduced to a minimum. Due to the finite conductivity of the walls and hoops there is a small amount of field line motion due to soak in. This field line

motion induces electric fields parallel to the magnetic field lines which are on the order of .1 V/m.

The sine wave case is illustrated in Figure 4b. Field line motion occurs due to flux entering the vacuum vessel through the poloidal and toroidal gaps. $E_\parallel \approx .1$ V/m at peak field and increases to ≈ 1 V/m late in the pulse when field lines are rapidly leaving the machine.

Figure 4c illustrates a poloidal ohmic heating mode of operation.[9] The poloidal field is crowbarred at peak field and then the B_θ field is fired. The rapidly changing B_θ field induces a strong electric field in the poloidal direction. Parallel electric fields on the order of 5 V/m can be obtained in this manner.

Figure 4d illustrates gun injection time. The gun is normally fired 2 msec after peak field in order to be clear of voltages glitches due to crowbars turning on. Measurements of density, temperature, and conductivity are made on the decaying plasma.

References for Chapter II

1. J. Steben, J. Appl. Phys., 43, 1211(1972)
2. T. Ohkawa and D. W. Kerst, Nuovo Cimento, 22, 784(1961)
3. J. R. Drake, et. al., Sixth IAEA conf. on Plasma Physics and Controlled Nuclear Fusion Research, 2, 333(1976)
4. R. A. Dory, PLP 27 (1964)
5. J. Schmidt, PLP 181 (1968)
6. H. P. Furth, Advances in Plasma Physics (Interscience publishers, N.Y., 1968), Vol. 1, p.67
7. J. Schmidt, Univ. of Wisc. Ph. D. Thesis, PLP 250 (1969)
8. G. A. Navratil, PLP 629 (1975)
9. J. Twichell, Bull. Am. Phys. Soc., 23, 835(1978)

Table II-1

Levitated Octupole Parameters

5 kV on B_p cap bank

	Wall	Inner Hoop	Outer Hoop
Current I	1.418 MA	.462 MA	.248 MA
B_{max} (at surface)	10 kG	13.7 kG	6.6 kG
B_{min} (at surface)	1.7 kG	6.4 kG	4.3 kG
Force Constant		11400 lb/cm	6530 lb/cm

Energy of pulse	.6 MJ
Total flux Φ	.846 W
Inductance L: $L=N^2L_1$, N=90, L_1=	.596 uH
Capacitance: C_{bank}	.048 F
Approx. half-sine-wave period	47.7 msec calculated
	43 msec observed
Volume of vacuum region	8.6 m^3
Volume of flux region (δ = 2.17 cm)	10.3 m^3
Min. # ion gyroradii (near outer wall)	23 at 100 eV

Figure II-1

Wisconsin Levitated Octupole

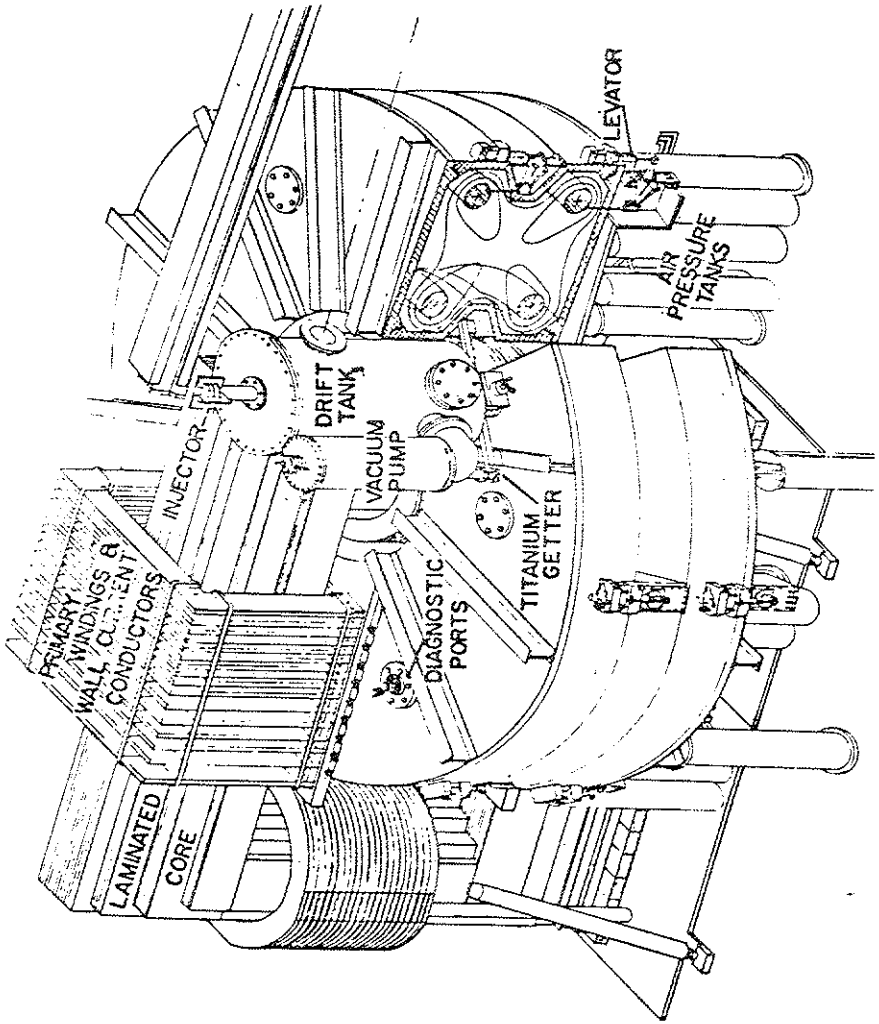

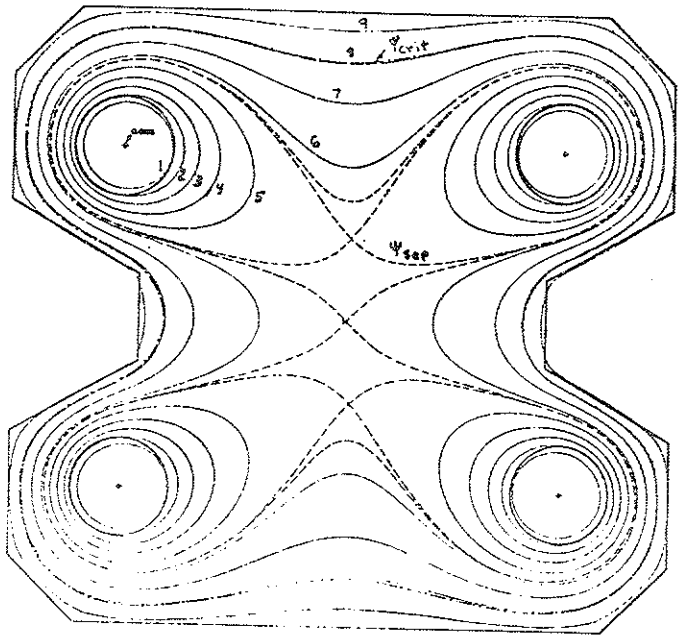

Figure II-2a

ψ surfaces, 20 msec

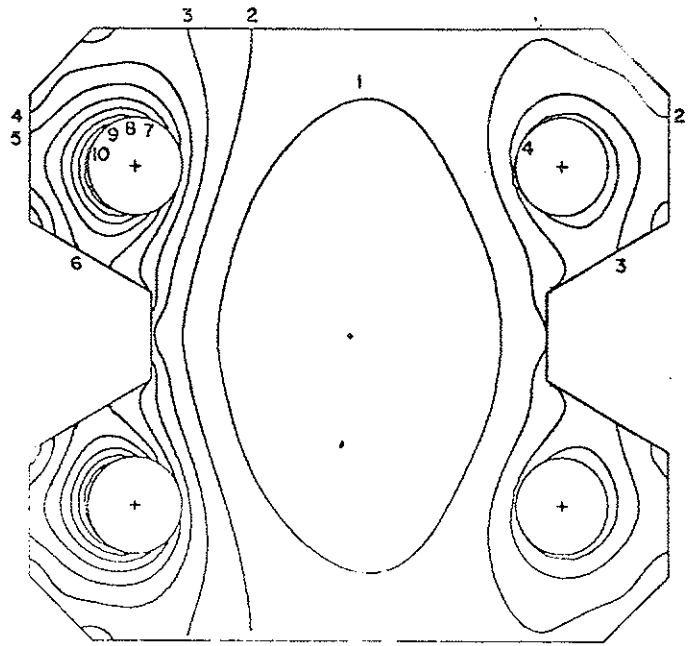

Figure II-2b

Constant B_p surfaces in kG

5 kV on cap bank

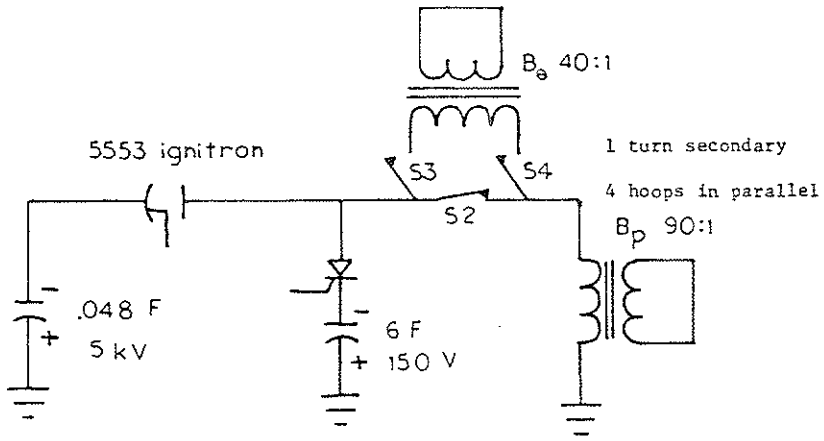

a. Poloidal field circuit

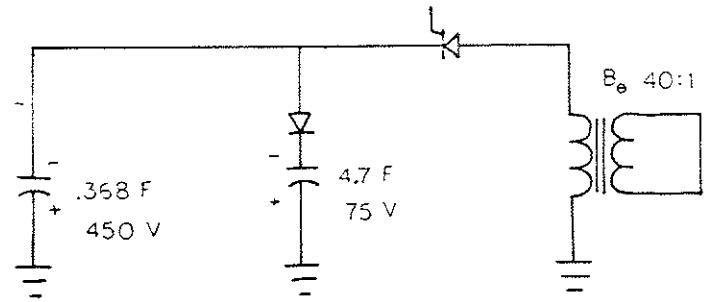

b. Toroidal field circuit

Figure II-3

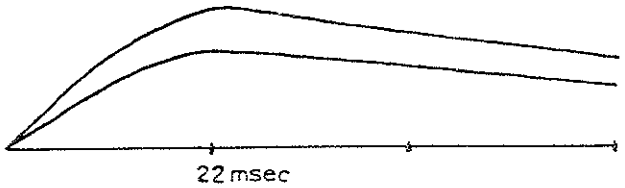

a. Crowbar $E_{\parallel} \simeq .1$ V/m

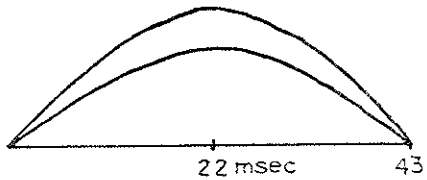

b. Sine wave $E_{\parallel} = .1 - 1$ V/m

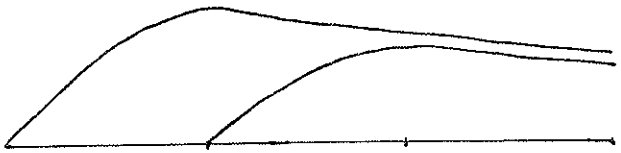

c. poloidal ohmic hearing $E_{\parallel} \simeq 5$ V/m

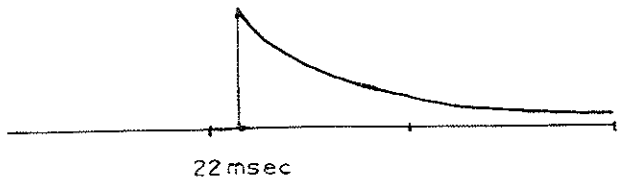

d. Injection time

Figure II-4

Chapter III

Plasma sources

Three coaxial plasma guns were used on the octupole for generating plasmas with varying densities, temperatures, and background neutrals.

A. Little gun

The little gun plasma has been extensively studied and described.[1,2,3] It is constructed out of two coaxial copper cylinders. The outer cylinder is 40 cm long and 7.5 cm outer diameter. The inner cylinder is 2.5 cm diameter. .5 cm^3 of hydrogen gas is puffed into the space between the cylindrical electrodes at the rear of the gun by a fast acting electromagnetic valve. The gas is allowed to diffuse for approximately 300 μsec during which time it distributes itself uniformly between the electrodes and then a 15 kV potential is applied to the electrodes causing the gas to ionize and expelling it from the gun by J x B forces.

The little gun is mounted on top of a drift tank of volume .3 m^3. Any un-ionized hydrogen from the gun pulse is differentially pumped in the drift tank and doesn't affect the toroid pressure until 100 msec after the gun has fired. The little gun produces a hot ion, collisionless plasma with $\lambda_{mfp} > 100$ mirror lengths. Initial density on the separatrix is $n \simeq 5 \times 10^9$ cm^{-3}. T_e and T_i are plotted versus time in Figure 1. T_i is greater than T_e for the first 20 msec after injection.

B. Intermediate gun

The intermediate gun has dimensions similar to those of the little gun. Unlike the little gun, the intermediate gun is mounted on the bottom lid and fires directly into the octupole without an intervening drift region. The little gun density is highly attenuated by passing through a 4" gate valve connecting the drift tank to the toroid.[4] The initial density of the intermediate gun is high, $n \simeq 5 \times 10^{11}$ cm^{-3} on the separatrix. T_i and T_e for the intermediate gun plasma are plotted versus time in Figure 2. Initially, T_i and T_e are similar to the values of the little gun but the ions cool rapidly and $T_e > T_i$ after about 5 msec.

C. Big gun

The big gun was constructed by G. A. Navratil in order to investigate diffusion coefficient scaling in a high density, low temperature plasma.[3] The outer electrode is a stainless steel tube 75 cm long and 8.25 cm outer diameter. The inner electrode is a copper tube 2.5 cm diameter. The big gun is mounted on the bottom lid and fires directly into the toroid. The big gun was operated in a low background regime and a high background regime.

(1) Low background pressure ($\simeq 10^{-7}$ Torr) Helium plasma

The big gun produces an initial plasma density of $n \simeq 10^{12}$ cm^{-3} on the separatrix. Since it is mounted directly on the toroid any un-ionized gas from the gun enters the vacuum vessel shortly after the plasma slug. Measurements with a fast ion gauge[5] indicate that the background neutral pressure remains low ($< 10^{-6}$ Torr) for the first 20 msec after the gun

is fired and then rises to $\simeq 10^{-5}$ Torr in the next 20 msec.

In the first 20 msec after gun injection the plasma is collisional with $\lambda_{mfp} <$ mirror length. The small collisional mean free path is due to Coulomb collisions. Neutral collisions play a minor role in the first 20 msec. T_e and T_i versus time are plotted in Figure 3a.

(2) High background pressure (5×10^{-6} Torr) Helium plasma

If the octupole is cycled continuously the neutral Helium background pressure rises because the vacuum pumps attached to the toroid have a hard time pumping the small Helium atoms. On a minute and a half cycle the background pressure rises to 5×10^{-6} Torr. When the big gun is fired into the toroid with a high background pressure the ions and electrons cool quickly to about .2 eV and then remain fairly constant in temperature. T_e and T_i versus time are plotted in Figure 3b.

In general, the ions can be cooled by firing the gun into an existing high background pressure or by puffing a known quantity of gas into the toroid after the gun is fired by means of the puff valve attached to the wall of the octupole. The puff valve method gives reproducible results. Relying on the background pressure is risky since it can vary from shot to shot.

References for Chapter III

1. R. A. Breun, Univ. of Wisc. Ph.D. Thesis (Physics), PLP 634 (1975)

2. C. J. Armentrout, Univ. of Wisc. Ph.D. Thesis (Physics) PLP 794 (1977)

3. G. A. Navratil, Univ. of Wisc. Ph.D. Thesis (Nuc. Eng.) PLP 693 (1976)

4. G. A. Navratil, PLP 629 (1975)

5. D. A. Brouchous, PLP 648 (1975)

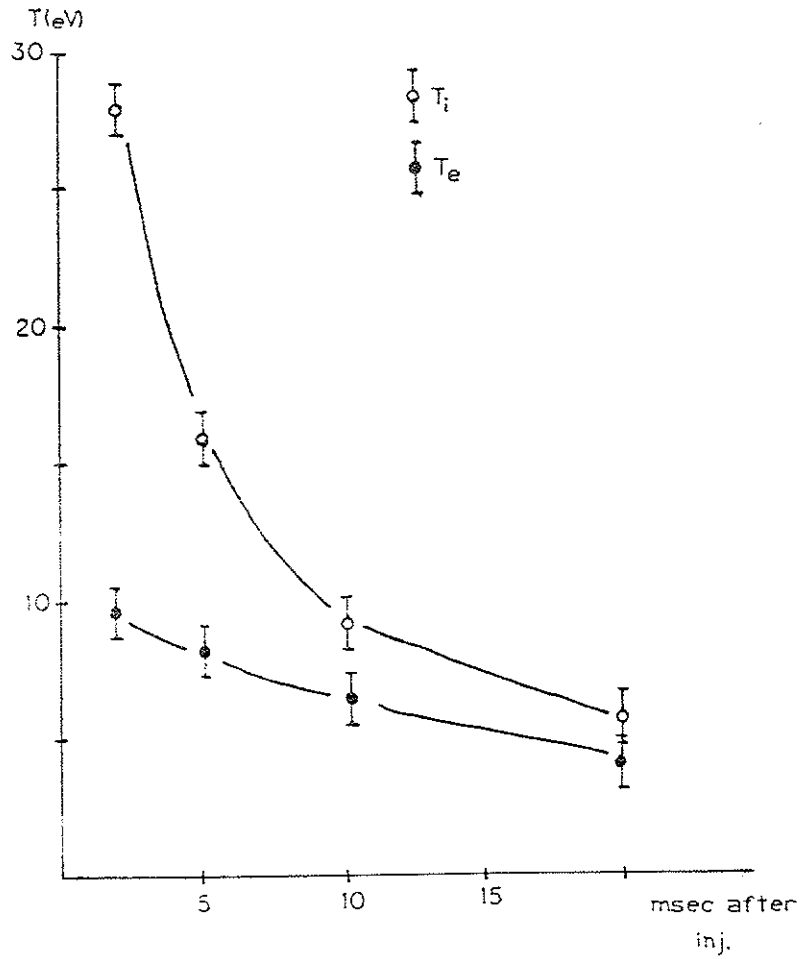

Figure III-1

T_i and T_e versus time for the little gun plasma. T_i obtained from skimmer probe, T_e from swept Langmuir probe.

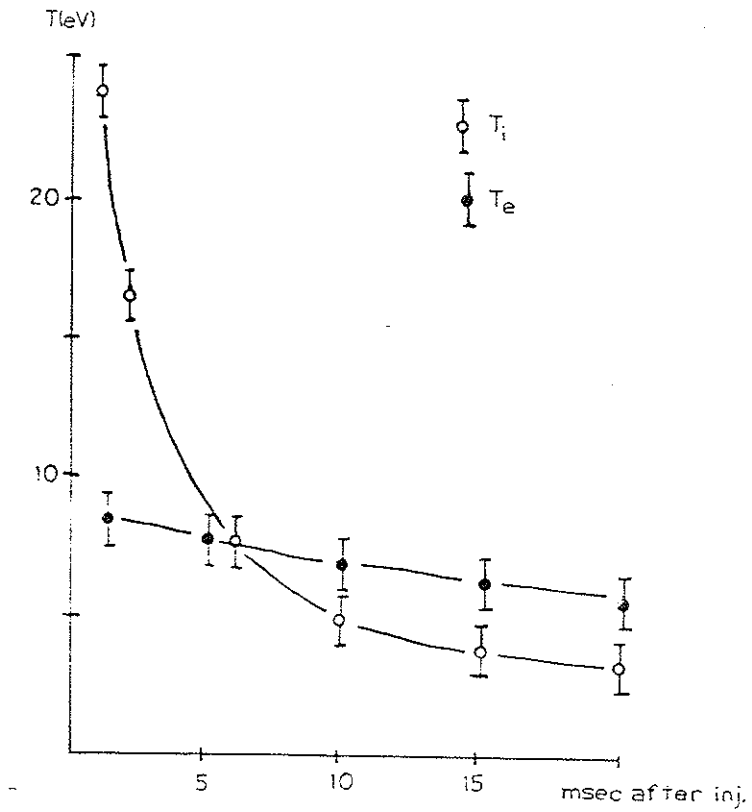

Figure III-2

T_i and T_e versus time for the intermediate gun plasma. T_i obtained from skimmer probe, T_e from swept Langmuir probe.

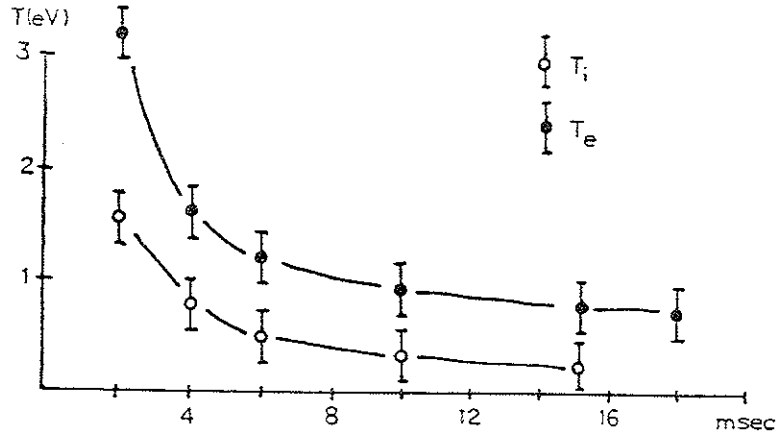

a. Big gun, He plasma fired into low neutral background

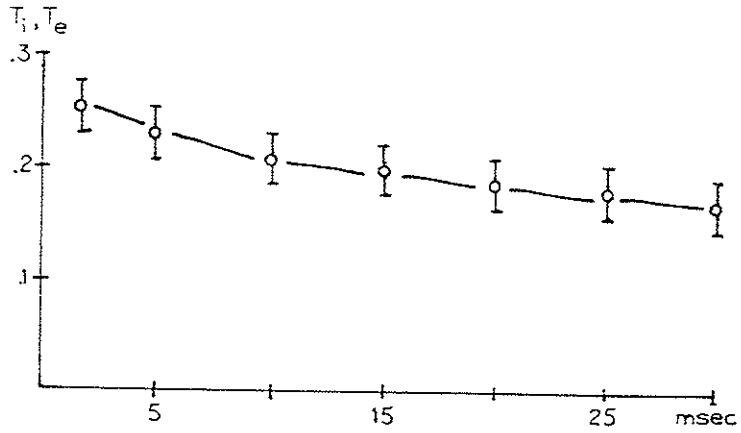

b. Big gun, He plasma fired into high neutral background, $T_e \approx T_i$

Figure III-3

Chapter IV

Diagnostics

A. Langmuir probes

Langmuir probes[1,2] were used extensively in this research to measure local values of plasma density and electron temperature. An experimental IV plot is illustrated in Figure 1a. The abscissa is the voltage applied to the probe with the octupole wall being the ground reference (0 Volts). For a large negative bias on the probe all the electrons are repelled and the current to the probe tip consists of ions. The ion saturation current is on the order of the ion diffusion current. I_i tends to increase slowly as higher negative voltages are applied to the probe.

As the probe potential approaches V_f energetic electrons are able to reach the probe. At the point V_f the flux of electrons to the probe equals the flux of ions and the net current is zero. This voltage is called the floating potential and is the voltage which an isolated object assumes when placed in the plasma.

In the transition region of voltages the probe collects an increasing number of the less energetic electrons until the point V_p (plasma potential) is reached where electrons of all energies are collected. The plasma potential for the little gun plasma is about 40 Volts 5 msec after injection. The plasma potential is difficult to determine from the IV characteristic since the change in slope between the transition region and the electron saturation region is not very sharp and leads to an uncertainty of ±5 Volts. An alternative method of measuring the

plasma potential is to use the relation

$$V_p = V_f + T_e \ell n(v_e/c_i) \qquad \text{IV-1}$$

where v_e is the electron thermal speed and $c_i = (8kT'/\pi m_i)$ is the ion sound speed. T' is the larger of T_e and T_i. Since V_f and T_e can be determined accurately, eqn. 1 can be used to determine V_p more precisely than the deflection point method.

When a probe is biased at the plasma potential the ions and electrons move to the probe at their thermal velocities. Since electrons move much faster than ions because of their small mass the current collected at the plasma potential is mainly electron current.

If the velocity distribution of the electrons is Maxwellian, then the electron current in the transition region is given by

$$J(V) = J(V_p)\exp\left[\frac{e(V-V_p)}{kT_e}\right] \qquad \text{IV-2}$$

Solving for the electron temperature gives[3]

$$\frac{kT}{e}e = \left[\frac{d\ \ell nJ(V)}{dV}\right]^{-1} \qquad \text{IV-3}$$

In practice, the determination of electron current versus potential requires several shots to be fired. The probe potential is varied between shots. Each IV point should be the average of 3-5 shots at the same probe potential. The IV points plotted on semi-log paper will determine a straight line if the electron velocity distribution is Maxwellian. T_e is the slope of the line.

Plasma density was determined by biasing the probe to -45 Volts in order to collect ion saturation current. The current to the probe tip is given by

$$\frac{I_{oi}}{A} = \frac{1}{4} nev^* \qquad \text{IV-4}$$

A is the surface area of the probe. The factor of 1/4 in eqn. 4 comes from two factors of 1/2. Assuming an isotropic velocity distribution only 1/2 of the ions are heading toward the probe. The other factor of 1/2 is the average of the direction cosine over a hemisphere. If $T_i > T_e$ then v* in eqn. 4 is given by

$$v^* = \left(\frac{8kT_i}{\pi m_i}\right)^{1/2} \qquad \text{IV-5}$$

If $T_i < T_e$ then v* is given by

$$v^* = \left(\frac{8kT_e}{\pi m_i}\right)^{1/2} \qquad \text{IV-6}$$

This satisfies the sheath criterion which requires cold ions to stream into the sheath boundary with an energy greater than 1/2 kT_e.

Effect of collisions on probe characteristics

The probe theory described above is valid for an unmagnetized plasma where the mean free path of the electrons and ions is much greater than the dimensions of the probe and where the sheath dimensions are much smaller than the probe dimensions. The response of a probe in a plasma

depends on a number of governing parameters. Table 1 lists the mean free path, Debye length, ion gyroradius, electron gyroradius, and probe radius for the 3 different gun plasmas used in this research.

It is seen that the little gun and intermediate gun satisfy the requirement $\lambda_{mfp} >> R >> \lambda_D$. A probe operating under these conditions

Table 1

	λ_{mfp}(m)	λ_D(m)	ρ_i(m)	ρ_e(m)	R(m)
Big gun	$.5 \times 10^{-3}$	2.4×10^{-6}	4.3×10^{-4}	1×10^{-5}	1×10^{-3}
int. gun	6.3	4.4×10^{-5}	4.8×10^{-3}	6×10^{-5}	1×10^{-3}
little gun	500	3.3×10^{-4}	5.3×10^{-3}	7×10^{-5}	1×10^{-3}

B = 1.5 kGauss

is said to be in the conventional thin sheath regime and the probe theory just discussed is applicable. The big gun does not satisfy the requirement $\lambda_{mfp} >> R$. The collisional mean free path is the same order of magnitude as the probe dimension. This leads to a decrease in the ion saturation current from eqn. 4. Figure 2 illustrates how this occurs. Figure 2a shows the collisionless case. R is the probe radius and λ is the collisional mean free path. The probe radius determines an area A_R while the mean free path determines an area A_λ. If $A_\lambda >> A_R$ the velocity distribution of ions at the edge of λ is isotropic and the random flux of ions to the probe surface is $J_r = 1/4\ nv$ from which eqn. 4 is obtained. In the collisional case where $A_R \rightarrow A_\lambda$ the distribution of velocities at A_λ is no longer isotropic since the probe blocks ≈1/2 the particle flux

to the surface. The random flux to the probe in this case is $J_r = 1/2\ nv$. In general, the ion saturation current is given by

$$\frac{I_i}{A} = \frac{nev^*}{4K} \qquad \text{IV-7}$$

where K = 1 for a collisionless plasma and K = 1/2 for a collisional plasma.

Effect of magnetic field on probe characteristics:

The effective mean free path across the magnetic field is of the order of a gyroradius. Particles cannot travel any further than this transversely without making a collision. From Table 1 it is seen that the electron gyroradius is much smaller than the probe radius in all three cases. Thus the electrons do not obey collisionless probe theory. In the absence of a magnetic field the ratio of electron saturation current to ion saturation current is the ratio of electron to ion thermal velocities.

$$\frac{I_e}{I_i} = \left(\frac{m_i T_e}{m_e T_i}\right)^{1/2} \qquad \text{IV-8}$$

which is approximately 25 for the little gun. From Figure 1 it is seen that the experimental value is $I_e/I_i = 10$. The electron saturation current is depressed in a magnetic field due to the small size of the electron gyroradius.

Another effect of a magnetic field is to destroy electron saturation. The electron current drawn to the probe increases as higher and higher

Ions ok for collisionless probe theory
Electrons - no good if $\rho_e < \lambda_{mfp}$
- what about the ions?

voltages are applied. This effect is not completely understood but has been tentatively explained in terms of sheath expansion at high bias voltages.[2,4] The nonsaturation of electron current makes the determination of V_p hard to accomplish from the IV plot. In the presence of a magnetic field it is more reliable to determine V_p from eqn. 1.

Physical construction of probes:

Figure 3a is an illustration of a typical probe used to monitor plasma density. The probe is biased to -45 Volts in order to collect ion saturation current. The probe tip is a cylinder machined from stainless steel. A coaxial cable connects the probe tip to the bias capacitor. The cutoff frequency of the probe is given by

$$f = \frac{1}{2\pi RC} \qquad \text{IV-9}$$

where R is the load resistor and C is the cable capacitance and oscilloscope input capacitance. Using $C_{input} = 20$ pF and $C_{cable} = 100$ pF gives f = 10 MHz for R = 100Ω.

Surface contamination:

The probe theory just discussed is valid only for a fully catalytic probe surface. At such a surface all positive ions immediately recombine with electrons and the neutralized species then return to the plasma. For a positive bias on the probe the surface acts as a perfect absorber of electrons. If the probe surface becomes contaminated with an oxide layer or vacuum grease picked up from the probe port the probe charact-

eristics are liable to change.

Deposits of insulating material on portions of the probe surface will decrease the collecting area of the probe and cause the probe to give lower saturation current readings. Armentrout has shown that a contaminated probe effects the measurement of floating potential.[4] Seeman and Thornton show probe characteristics in the transition region for a contaminated probe and a clean probe.[5] As illustrated in Figure 3b the contaminated probe shows a decrease in the current slope near the floating potential which gives an erroneously high value for T_e.

Contaminated probes affect measurements of n, V_f and T_e. It is essential to clean a probe thouroughly in order to obtain reliable measurements of these parameters. All probes used in this research were constructed of nonmagnetic stainless steel. Probe tips were de-greased with alcohol and acetone and then abraded with 600 grit silicon carbide paper prior to use. Probes were not used in regions of the machine subject to direct getter shine. Contrary to expectations a deposit of titanium acts like an insulator and depresses the saturation current. Swift and Schwar[5] recommend biasing the probe deep into the ion saturation region (100 - 200 Volts) in order to bombard the probe surface with energetic ions. They suggest this technique be used at intervals to sputter off contaminants which may have accumulated on the probe tip.

B. Ion temperatures

Ion temperatures were the most difficult measurements to make on the octupole. Breun[7] and Erickson[8] used curved plate electrostatic energy analyzers to measure the ion velocity distribution. These analyzers required a hypernick extractor pipe which extended down to the midcylinder separatrix. This extractor pipe acted as a large obstacle to the plasma equal in area to all 16 of the hoop supports. This type of analyzer was not able to detect ions with energies less than 3 eV.

Navratil[9] used a gridded electrostatic analyzer for measuring ion temperature. This analyzer was also restricted to operating on the midcylinder separatrix. The main advantages of Navratil's analyzer were its small size and its ability to measure ion temperatures as low as .1 eV. A disadvantage was that it could only be used on the midcylinder separatrix. Other experimenters had trouble with negative currents when large biases were applied to the grids of the device. The negative currents were ~10% of the magnitude of the ion saturation current and were attributed to secondary electrons being knocked off the grids and walls of the analyzer.[10]

Figure 4 is an illustration of an ion energy analyzer which is referred to as a skimmer probe.[11,12,13] The device can be constructed so that it is less than 1/4" in diameter and thus is able to fit through any probe port on the octupole. The electrodes were machined from stainless steel. The grids are 2 mil 90 mesh stainless steel with 80% transparency. The probe must be oriented so that the magnetic field is perpendicular to the probe axis as illustrated in Figure 4. The collector electrode is located .3 mm behind the outer grid. This

distance was chosen so that the outer grid would skim off electrons but ions (with their larger gyroradius) would be able to reach the collector. Figure 5 shows the motivation behind the .3 mm spacing. For a magnetic field of 1.5 kG (B_p = 1.5 kG on bridge separatrix at peak field) all electrons up to T_e = 100 eV have gyroradii less than .3 mm and will be skimmed off by the outer grid. All hydrogen and helium ions with T_i > .1 eV have gyroradii greater than .3 mm and can reach the collector. Thus the collector sees only ions.

The grids and collectors are biased as shown in Figure 4. The outer grid is allowed to float. The collector is biased 45 Volts negative with respect to the outer grid and collects ion saturation current. The inner grid is swept positive with respect to the outer grid in order to discriminate in ion energy. Figure 4b shows the collector current versus inner grid voltage. If the ion velocities satisfy a Maxwellian distribution the collector current will give a straight line when plotted on semi-log paper with the slope of the line equal to the ion temperature. Experimental data obtained with skimmer probes have given straight line plots over two decades of ion current. Negative currents at high biases have not been observed.

The main advantages of this probe are its small size and the fact that it is not limited to one region of the octupole. Ion temperature scans can be made in the bridge region to obtain ion temperature versus position. This is subject to the restriction that ρ_e < .3 mm < ρ_i.

The main disadvantages of this probe are its difficulty in construction and its fragility. Because of the close spacing the grids are subject to arcing and can easily be destroyed at high bias in a dense plasma.

C. Current density

Paddle probes[14] and Rogowsky loops[15] were used to measure the local value of the plasma current density. A paddle probe is illustrated in Figure 6a. The probe tips are 4 mm x 4 mm sheets of stainless steel shim stock. The two tips are insulated on one side with mylar and epoxy. The insulated sides face each other. The uninsulated sides face in opposite directions and are biased so as to collect electron saturation current. The electrons, being more mobile than the ions, carry the bulk of the plasma current. The signals from the two electrodes are fed into a differential amplifier and the output from the differential amplifier gives the net plasma current flowing in the direction perpendicular to the probe tips. In practice the probe tips are oriented so as to measure the plasma current parallel to the magnetic field.

Lencioni[14] has shown that the difference in currents collected by the two electrodes is given by

$$I(V) = eA\left[\int_{\sqrt{2e(V_p-V)/m}}^{\infty} f(v)vdv \; - \int_{-\sqrt{2e(V_p-V)/m}}^{-\infty} f(v)vdv\right] \qquad \text{IV-10}$$

where A is the electrode area, V is the bias on the electrode, and V_p is the plasma potential. If the electrons have a shifted Maxwellian velocity distribution then

$$f(v) = n\left(\frac{m}{2\pi kT}\right)^{1/2} e^{-m(v-v_o)^2/2kT} \qquad \text{IV-11}$$

where v_o is the electron drift caused by the induced electric field parallel to the magnetic field.

$$J = nev_o \qquad \text{IV-12}$$

Substituting eqn. 11 into eqn. 10 gives

$$\frac{\Delta I(V)}{A} = J = nev_o\left[1 + \frac{\sinh(2\sqrt{\eta}\nu)}{\sqrt{\pi}\nu}\, e^{-\eta-\nu^2}\right.$$

$$\left. -\frac{1}{2}\left[\mathrm{erf}(\sqrt{\eta} + \nu) + \mathrm{erf}(\sqrt{\eta} - \nu)\right]\right] \qquad \text{IV-13}$$

where $$\eta = \frac{e(V_p - V)}{kT_e} \qquad \text{IV-14}$$

and $$\nu = \frac{v_j}{\sqrt{2kT_e/m}} \qquad \text{IV-15}$$

Eqn. 13 was evaluated for $\nu = 1$ and $\nu = .03$ and the results are plotted in Figure 6b assuming $V_p = 45$ Volts and $T_e = 10$ eV. Also plotted are experimentally obtained values of J versus bias on the paddle probe. The experimental data are seen to lie in between the calculated curves indicating that $.03 < \nu < 1$ for the experimental electron drift velocity.

Theoretically, the paddle probe current should saturate when bias voltages greater than the plasma potential are applied. Experimentally this is not the case, the paddle probe current continues to rise for bias voltages greater than 45 Volts. Note that nonsaturation of the electron current was also observed for a single tip Langmuir probe as was discussed previously. This nonsaturation is believed to be caused by sheath expansion and gives erroneously high values for current density

if a bias greater than the plasma potential is applied to the paddle probe. All plasma current densities quoted in this work were obtained with the paddle probe biased at the plasma potential.

The paddle probe is directional so that rotating the probe by an angle θ should decrease the collected current by $\cos\theta$. If the probe is rotated 180^0 the current from the paddle probe should reverse direction. This serves as a check on whether or not the probe is working properly. In practice, a two shot average of the current was taken, one with the probe at 0^0 and the other at 180^0. The paddle probe functioned well in low density plasmas and always showed reversed currents when rotated 180^0. This was not always found to be the case in high density plasmas such as those produced by the big gun. Often the scope traces for the rotated positions were found to differ in magnitude and shape and sometimes they were found not to reverse at all. It is not known why the paddle probe functions so poorly in a high density plasma but it may be caused by the highly collisional nature of this plasma as was discussed in section IV-A. Another possibility is that the plasma is shorting the two electrodes together and causing the paddle probe to act like a single tip Langmuir probe.

A Rogowsky loop was built in order to measure the plasma current density in the big gun plasma. Construction details are illustrated in Figure 7. The loop was built small enough so that it was able to fit through a 2" gate valve and was able to measure currents on the midcylinder from the bottom lid to the midcylinder separatrix. These measurements could then be compared with those obtained from a paddle probe.

The winding on the loop was brought back through itself as illustrated in Figure 2 so that the loop does not pick up flux threading the area πR^2 but only flux threading πr^2 where R is the major radius and r is the minor radius. The entire loop was enclosed in an elecrostatic shield made of copper foil with a toroidal gap and a poloidal gap. The outside of the shield was coated with a layer of epoxy so that no metal was exposed to the plasma. In practice the electrostatic shield was grounded to the tank. This prevented the Rogowsky coil from coupling capacitively to the plasma. The gaps in the shield allowed magnetic flux to enter the Rogowsky coil.

Two Rogowsky loops were constructed; one with an air core and one with a ferrite core. The loops were calibrated by discharging a capacitor through a resistor and measuring the current through the resistor with the Rogowsky loop. The current through the resistor was chosen so that it approximately matched in magnitude and time variation the current flowing in the octupole. The induced signal in the air core loop was only a factor of 2 or 3 greater than the background noise. The ferrite core loop gave signal to noise ratio of ≈100.

The ferrite core loop was used to measure current densities in the octupole and was found to give readings a factor of 5 greater than those obtained with a paddle probe. The factor of 5 may be caused by the Rogowsky coil reading high or the paddle probe reading low. The ferrite core may cause the Rogowsky loop to read high as illustrated in Figure 7b. Because of its high permeability the ferrite core bends magnetic field lines in its vicinity and thus guides more current into the throat of the loop. This effectively increases the area of the loop and causes

erroneously high readings. The paddle probe may read low because of the highly collisional nature of the big gun plasma as discussed previously or because the electrodes are being shorted by the plasma.

Using the paddle probe or Rogowsky loop in the big gun plasma can give only an order of magnitude estimate of the current density. In practice the average reading from the two methods is used for the current density and large error bars are employed.

D. E x B energy analyzer

Figure 8 is an illustration of an E x B analyzer which was used for measuring electron velocity distributions.[16] The velocity distribution is an important plasma parameter and uniquely determines temperature, electron drift velocity, and total electron energy. It also provides information about instabilities and dissipative processes in the plasma.

The analyzer walls and end plates were machined from brass. Wall thickness is < 1 mm so that a magnetic field is able to soak through in 50 μsec. The outside of the walls and end plates was covered with a layer of epoxy except for a small area around the entrance aperture. The 1 mm entrance aperture allows electrons to enter the analyzer but excludes ions because of their larger gyroradii.

In operation the analyzer case was biased at the plasma potential. The analyzer was located on the midcylinder separatrix and was oriented so that the toroidal magnetic field was parallel to the analyzer axis. Voltages +V and -V with respect to the analyzer case were placed on two deflector plates to create an electric field E perpendicular to the magnetic field. An electron trajectory is illustrated in Figure 8 for

the case E = 0. The electron enters the analyzer through the entrance aperture, travels through the deflector plates and is collected by a small electrode on the end plate. There are five of these electrodes and they are referred to as channels 1-5 with channel 1 being the electrode which collects the undeflected beam of electrons. Channels 1-5 are at the same potential as the case but are insulated from the case and from each other.

When an electric field is present between the deflector plates the guiding centers of the electrons drift perpendicular to the E and B fields with a velocity v_d.

$$v_d = \frac{E \times B}{B^2} \qquad \text{IV-16}$$

Fast electrons and slow electrons experience the same drift velocity but since the slow electrons are in the deflection region longer they experience more of a deflection than the fast electrons. In this manner the analyzer is able to distinguish between electrons with different parallel velocities. The slower electrons, being deflected more, are collected by higher channels. The fast electrons, being deflected less, are collected by lower channels.

Figure 9 shows experimentally obtained currents from channel 1 versus electric field in the deflection region. When E = 0 electrons of all velocities are collected by channel 1. As higher electric fields are applied, the low energy electrons are deflected to higher numbered channels and the current to channel 1 decreases.

The velocity window seen by each channel can be determined with the

aid of Figure 10. The transit time of an electron through the deflection region is

$$t_{tr} = \frac{L}{v_{\parallel}} \qquad \text{IV-17}$$

where L is the length of the deflector plates and $v_{\parallel}$ is the electron velocity parallel to the magnetic field. The deflection of the electron caused by the E x B drift is

$$d = v_d t_{tr} = \frac{E}{B}\frac{L}{v_{\parallel}} \qquad \text{IV-18}$$

If the positions of the channels are known and if E, B, and L are known then the velocity window can be calculated for each channel by solving eqn. 18 for $v_{\parallel}$. This is illustrated in Figure 10 for channel 3.

$$v_1 = \frac{E}{B}\frac{L}{d_1} \qquad \text{IV-19}$$

$$v_2 = \frac{E}{B}\frac{L}{d_2} \qquad \text{IV-20}$$

where $v_2 < v_1$. The velocity window is

$$\Delta v = v_1 - v_2 \qquad \text{IV-21}$$

The velocity windows for channel 1 for given E and B_θ = 300 Gauss are given in Figure 9. Note that the upper energy bound for channel 1 is ∞.

The current collected by a channel is given by

$$I = \int_{v_o - \Delta v/2}^{v_o + \Delta v/2} ef(v_{\parallel}) v_{\parallel} \, dv_{\parallel} \qquad \text{IV-22}$$

where v_o is the mean velocity of the channel and Δv is the velocity window. Δv is given in eqn. 21 and v_o can be calculated if E and B are known. The electron velocity distribution function is given by

$$ef(v_\parallel) = \frac{\int_{v_o - \Delta v/2}^{v_o + \Delta v/2} ef(v_\parallel) v_\parallel dv_\parallel}{v_o \Delta v} = \frac{I}{v_o \Delta v} \qquad \text{IV-23}$$

A number of plasma parameters can be calculated from the distribution function:

$$n_e = \int_{-\infty}^{+\infty} f(v)dv = \sum_i f(v_i)\Delta v_i \qquad \text{IV-24}$$

$$v_d = \frac{\sum_i f(v_i) v_i \Delta v_i}{n_e} \qquad \text{IV-25}$$

$$J = e n_e v_d \qquad \text{IV-26}$$

$$E = \frac{m_e}{n_e} \sum_i f(v_i) v_i^2 \Delta v_i \qquad \text{IV-27}$$

$$E_d = \frac{m_e}{n_e} (v_d)^2 \qquad \text{IV-28}$$

$$T_e = \frac{E - E_d}{k} \qquad \text{IV-29}$$

Eqn. 24 gives the electron density. The electrons are restricted to motion in one direction, parallel to the magnetic field. The integral has been replaced with a summation. The v_i and Δv_i are determined by

E and can be varied shot by shot to get many points of the distribution function. Eqn. 25 gives the drift velocity of the electrons caused by the induced parallel electric field. The drift velocity is obtained by summing over positive and negative velocities which are obtained by rotating the analyzer 180° so as to measure velocities parallel and antiparallel to the electric field.

Eqn. 26 gives the current density which is obtained from the drift velocity of eqn. 25. This current density can be compared with that obtained by means of a paddle probe or Rogowsky loop. Figure 11 shows the velocity distribution and drift velocity of the intermediate gun plasma 2 msec after injection into sine wave B_p and B_θ fields. The experimental data points agree with a shifted Maxwellian distribution with $T_e = 8$ eV and $v_d = 1 \times 10^5$ m/sec. The drift velocity cannot be determined by merely looking at f(v) versus v because v_d is much smaller than v_e. v_d must be calculated using eqn. 25. v_d can be determined accurately if a large number of $f(v_i)$ points are available. v_d obtained with the E x B analyzer agrees within a factor of 2 with that obtained from a paddle probe. This is not surprising since the E x B analyzer used in this way is just acting like a two step paddle probe with the calculation of eqn. 25 acting as the differential amplifier.

Eqn. 27 gives the energy per electron contained in the random motion. Eqn. 28 gives the electron energy contained in the drift velocity. For the distribution illustrated in Figure 4, $E_d/E \simeq 10^{-2}$. Eqn. 29 gives the electron temperature which can be approximated as $T_e = E/k$ for the low drift velocities considered here.

References for Chapter IV

1. P. M. Chung, Electric probes in stationary and flowing plasmas, (Springer-Verlag, 1975)
2. F. F. Chen, Plasma Diagnostic Techniques, (R. H. Huddlestone and S. L. Leonard, eds., Academic Press, N. Y., 1965), chapter 4
3. J. C. Sprott, PLP 88 (1966)
4. C. J. Armentrout, Univ. of Wisc. Ph.D. Thesis (Physics) 1977
5. G. R. Seeman and J. A. Thornton, AIAA 2nd Fluid and Plasma Dynamics conf., San Francisco, 1969, Paper 69-700
6. J. D. Swift and M. J. R. Schwar, Electric Probes for Plasma Diagnostics, Iliffe Books, Ltd., London, 1971
7. R. A. Breun, Univ. of Wisc. Ph.D. Thesis (Physics), PLP 634 (1975)
8. C. W. Erickson, Univ. of Wisc. Ph.D. Thesis (Physics), PLP 100 (1967)
9. G. A. Navratil, Univ. of Wisc. Ph.D. Thesis (N. Eng.), PLP 693 (1976)
10. E. A. Rose, private communication
11. D. A. Brouchous, PLP 624 (1975)
12. H. W. Motley and T. Kawabe, Phys. of Fluids 14,1019(1971)
13. I. Katsumata and M. Lkazaki, Japan J. Appl. Phys. 6,123(1967)
14. D. E. Lencioni, Univ. of Wisc. Ph.D. Thesis (Physics), PLP 276 (1969)
15. G. Barney and J. Hawxhurst, PLP 32 (1964)
16. W. L. Barr and W. A. Perkins, Rev. Sci. Inst., 37,1354(1966)

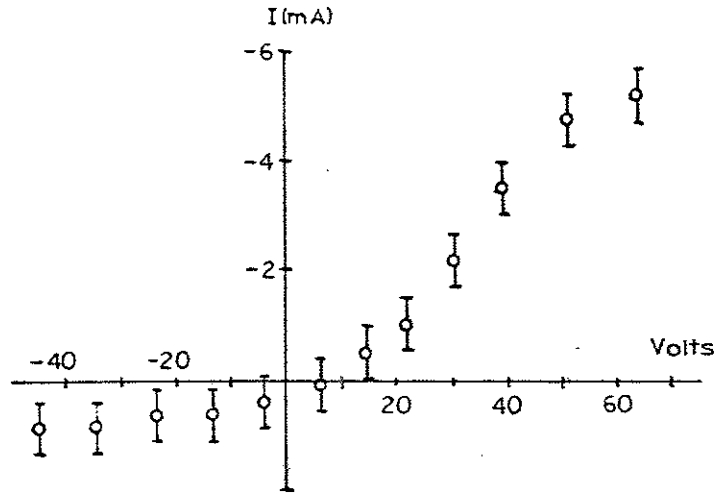

a. Experimental probe characteristic. Little gun plasma 5 msec after inj.

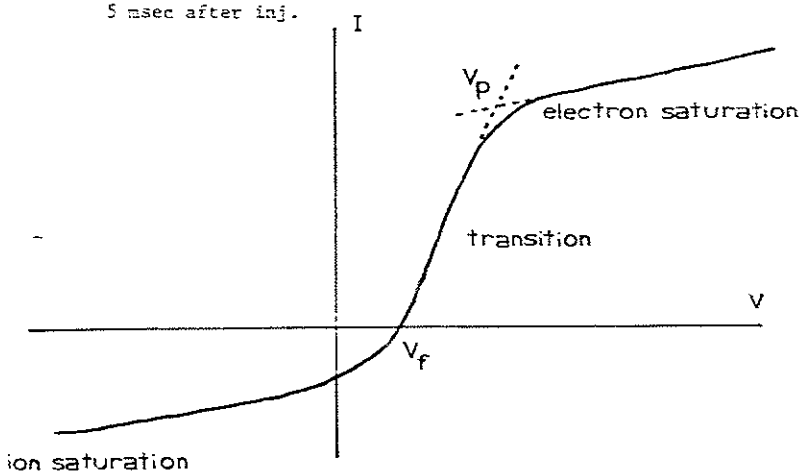

b. Theoretical probe characteristic

Figure IV-1

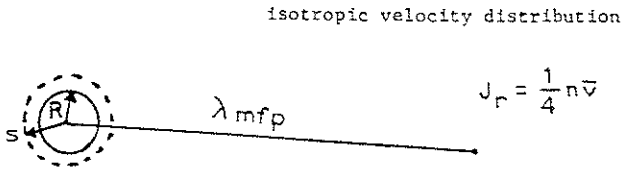

a. Collisionless

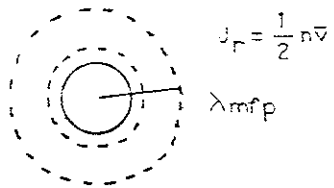

b. Collisional

Figure IV-2

Illustration of the effect of high collisionality on probe characteristics

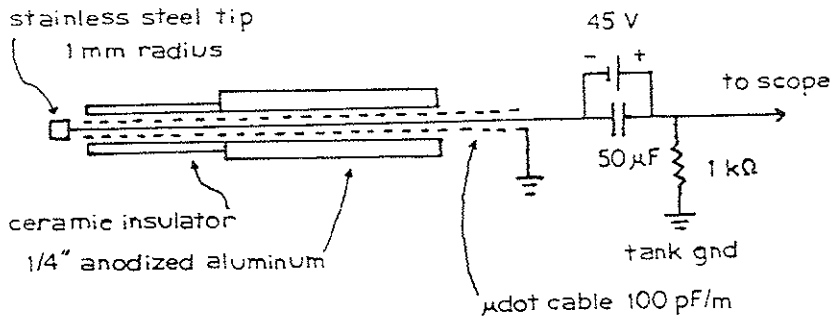

a. Langmuir probe construction details

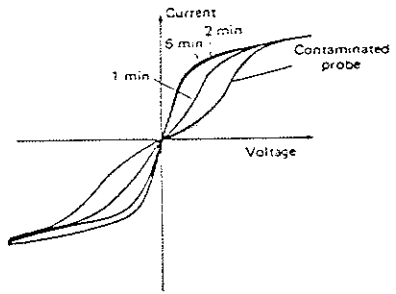

b. Illustration of surface contamination effects on probe characteristics.[5] The clean probe was biased to collect an ion current of 1 mA for 6 min in order to sputter off surface contaminants.

Figure IV-3

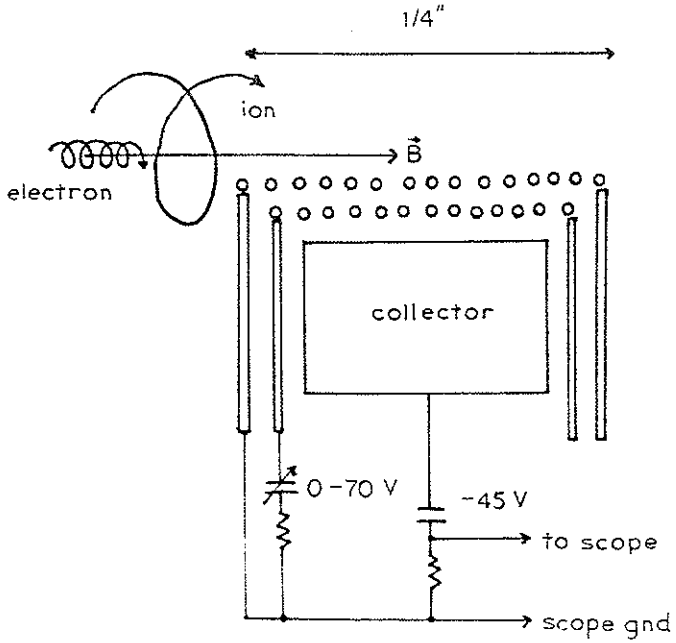

a. Skimmer probe biasing

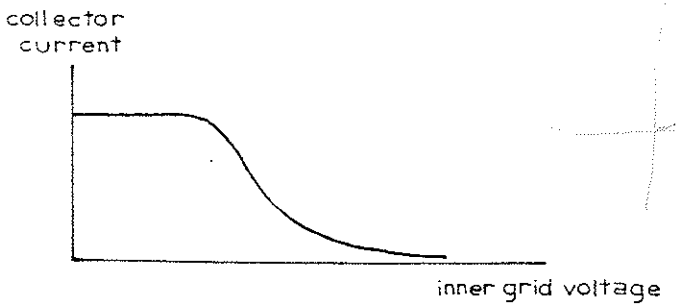

b. Collector current for a Maxwellian ion distribution

Figure IV-4

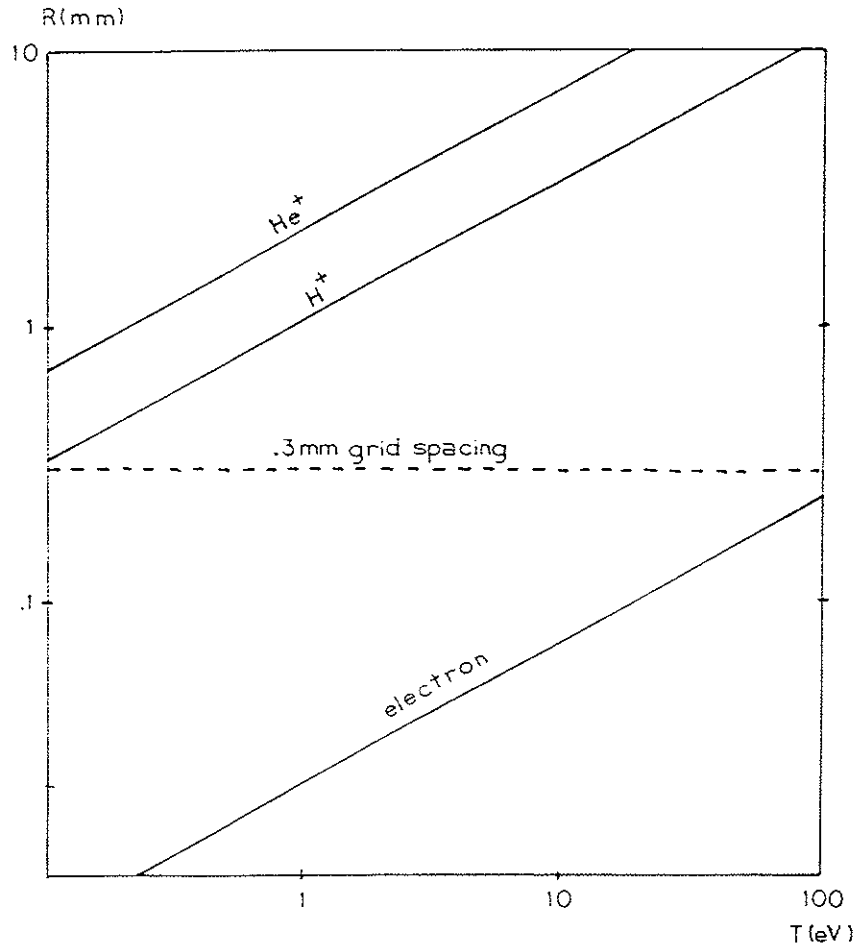

Figure IV-5

Ion and electron gyroradii versus energy. .3mm grid spacing skims off electrons but not ions.

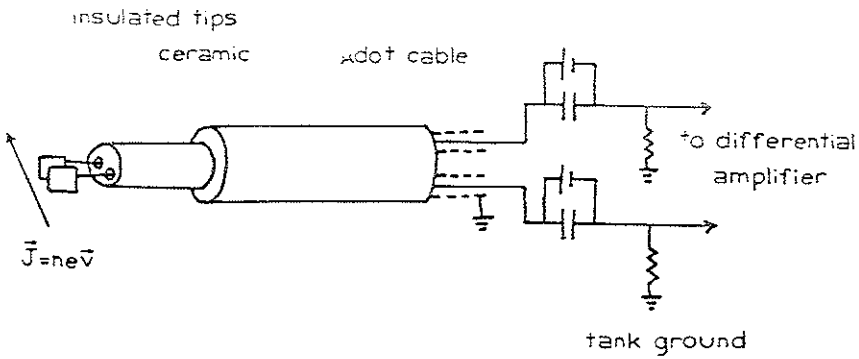

a. Paddle probe construction

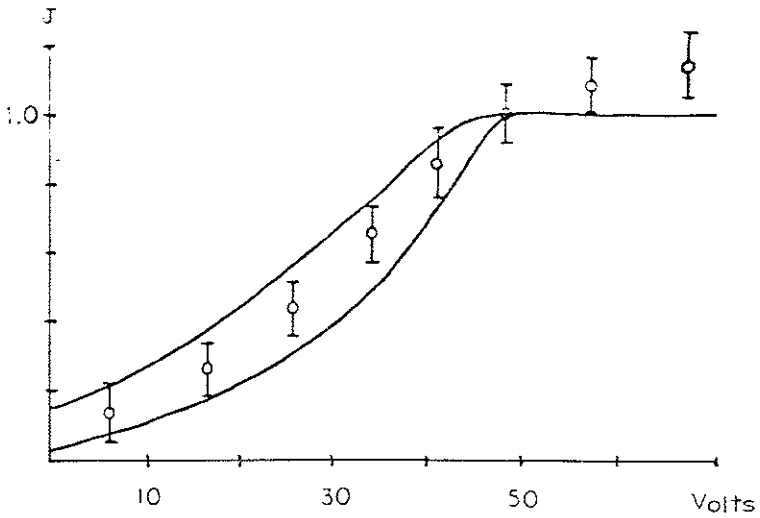

b. Experimental current density versus voltage

Figure IV-6

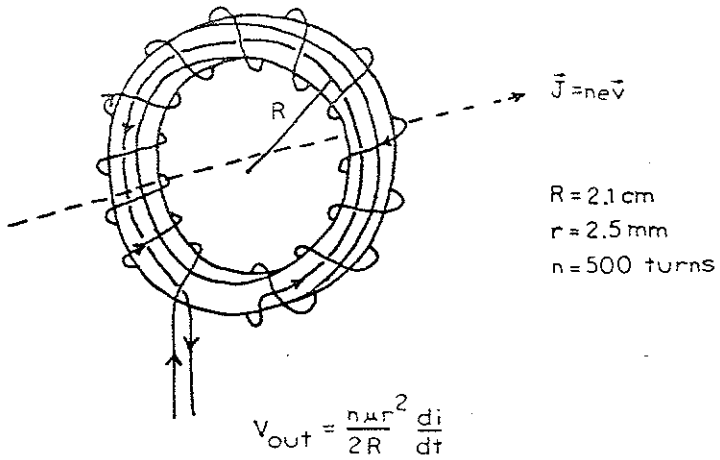

a. Rogowsky coil construction

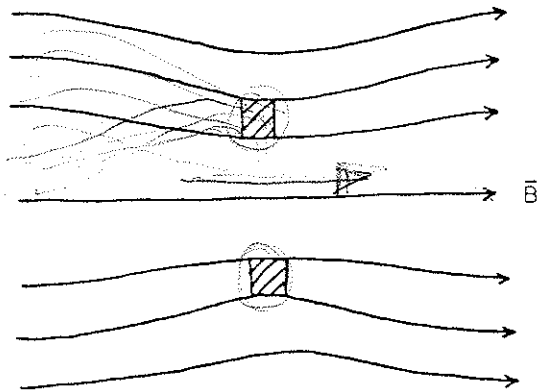

b. Increase in current density seen by Rogowsky coil due to field lines bending into high permeability core.

Figure IV-7

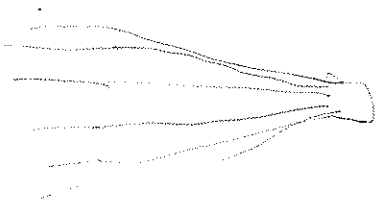

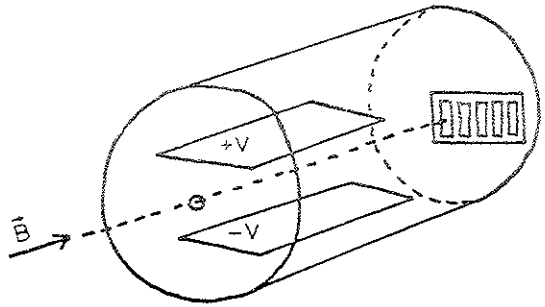

a. Analyzer is aligned parallel to B so that the electron beam strikes channel 1

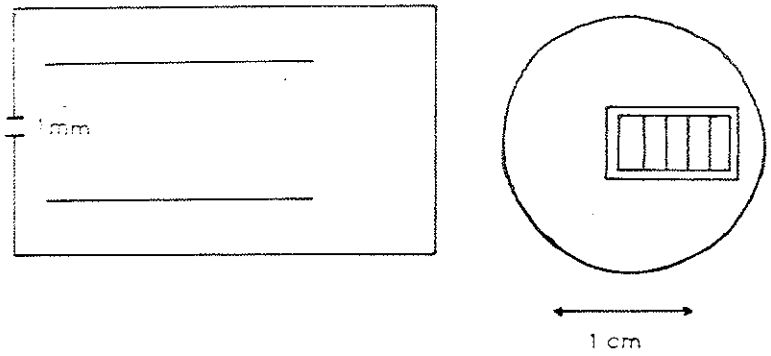

b. Analyzer dimensions

Figure IV-8

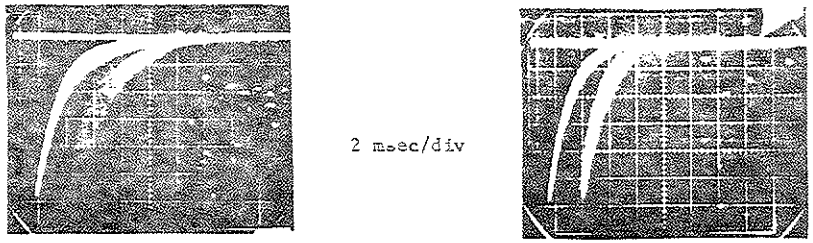

E = 0
v = 0 → ∞
2 mAmp/div

E = 3000 V/m
v = 2 x 10^6 m/sec → ∞
2 mAmp/div

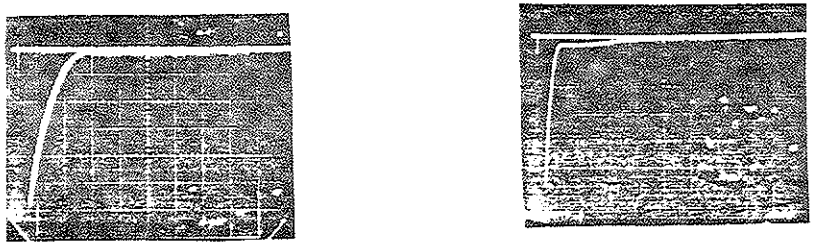

E = 5000 V/m
v = 3 x 10^6 m/sec → ∞
1 mAmp/div

E = 12000 V/m
v = 8 x 10^6 m/sec → ∞
.2 mAmp/div

Figure IV-9

Electron current collected by channel 1

E x B analyzer on midcylinder sep.

B_g = 300 Gauss, B_p 2.5 kV, little gun plasma

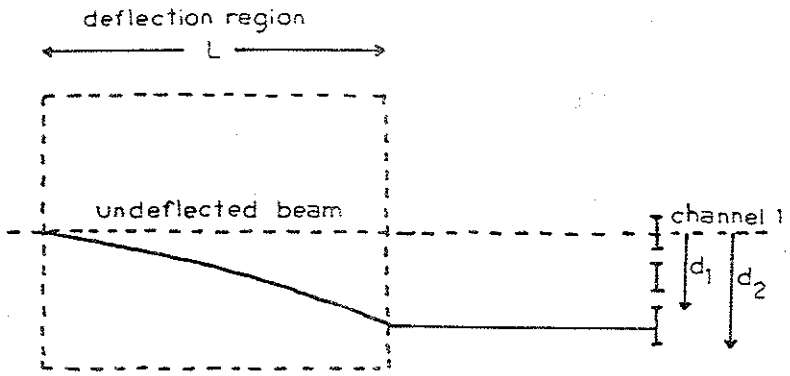

$$t_{tr} = \frac{L}{v_e}$$

$$d = v_d t_{tr} = \frac{E}{B}\frac{L}{v_e}$$

$\Delta v = v_1 - v_2$ energy window

$$v_1 = \frac{E}{B}\frac{L}{d_1}$$

$$v_2 = \frac{E}{B}\frac{L}{d_2}$$

Figure IV-10

Calculation of energy window

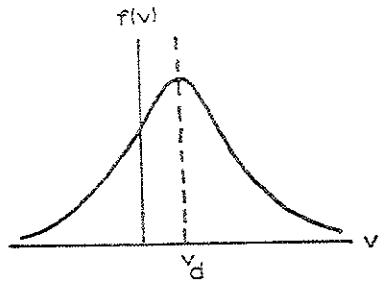

a. Displaced Maxwellian. v_d greatly exaggerated.

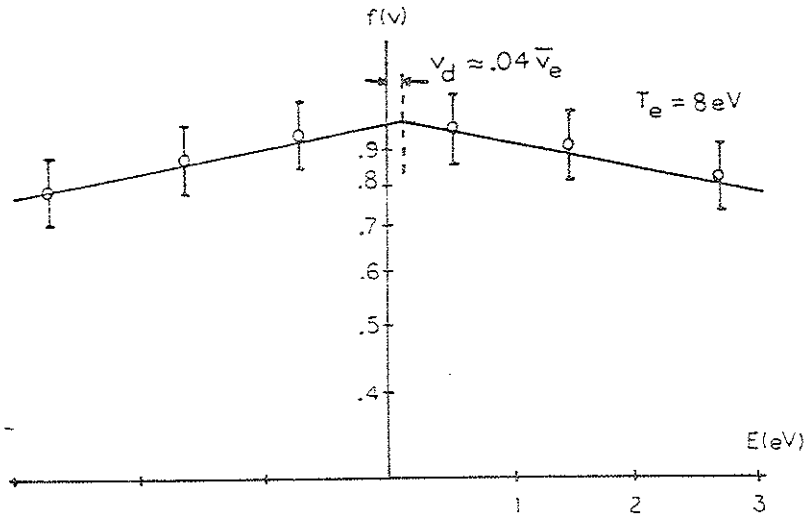

b. Velocity distribution obtained from E x B analyzer.

Int. gun, 2 msec after inj., B_p & B_θ sine wave, 2.5 kV

Figure IV-11

Chapter V

Calculation of Induced Electric Fields

Whenever an electric field exists in a magnetized plasma, there is the possibility of an E x B drift of the plasma as a whole relative to the laboratory frame. We need to determine the transformed electric field in the plasma frame which will be responsible for driving conduction current. In general if $\vec{E}_o = -\dot{\vec{A}}$ in the laboratory frame then $\vec{E} = -\dot{\vec{A}} + \vec{v}_D \times \vec{B}$ in the plasma frame drifting with velocity v_D.

We can have $A(t) = A_p(t) + A_\theta(t)$ where $-A_p(t)$ would produce a toroidal component of electric field and $-A_\theta(t)$ would produce a poloidal component. With the usual E x B drift

$$\vec{v}_D = \frac{\vec{E}_o \times \vec{B}}{B^2} \qquad V\text{-}1$$

giving
$$\vec{E} = -\dot{\vec{A}} + \frac{\vec{E}_o \times \vec{B}}{B^2} \times \vec{B} \qquad V\text{-}2$$

$$= -\dot{\vec{A}} - \vec{E}\frac{\vec{B}\cdot\vec{B}}{B^2} + \vec{B}\frac{(\vec{E}_o \cdot \vec{B})}{B^2}$$

The first two terms cancel each other and we are left with

$$\vec{E} = \frac{\vec{E}_o \cdot \vec{B}}{B^2}\vec{B} \qquad V\text{-}3$$

Eqn. 3 shows that the electric field in the moving frame is parallel to the magnetic field. Thus the E x B drift is the transformation that

removes all the electric field components except that which is parallel to the magnetic field. That the parallel electric field cannot be removed is to be expected since in any frame with velocity v, $\vec{v} \times \vec{B}$ is the change of the electric field for the moving coordinates and $\vec{v} \times \vec{B}$ has no component parallel to $\vec{B}$. Thus no change can be caused in a parallel electric field.

There are some cases of drifting coordinates of special interest. First, if there is no component of E parallel to B then $\vec{E}\cdot\vec{B} = 0$ or

$$E_p B_p + E_\theta B_\theta = 0$$

and
$$\frac{E_\theta}{B_p} = -\frac{E_p}{B_\theta} \qquad V\text{-}4$$

The field lines have fictitious velocities given by $E_\theta/B_p = v_{\psi p}$ and $-E_p/B_\theta = v_{\psi\theta}$ where subscripts refer to poloidal and toroidal components of fields. Eqn. 4 shows that poloidal and toroidal field line velocities are equal when $\vec{E}\cdot\vec{B} = 0$.

If $\vec{E}\cdot\vec{B} \neq 0$ then $E_p/B_\theta \neq -E_\theta/B_p$ and poloidal lines move at a different velocity than toroidal lines. This is generally the case since poloidal topology has non-uniform flux surface shapes compared with toroidal flux surface shapes.

Eqn. 2 can be written as

$$\vec{E} = -\dot{\vec{A}}_\theta - \dot{\vec{A}}_p - \left[\vec{B} \times \frac{\vec{E}_\theta \times \vec{B}}{B_p^2}\frac{B_p^2}{B^2} + \vec{B} \times \frac{\vec{E}_p \times \vec{B}}{B_\theta^2}\frac{B_\theta^2}{B^2}\right]$$

which takes the form

$$\vec{E} = -\dot{\vec{A}}_\theta - \dot{\vec{A}}_p - \vec{B} \times \left[\vec{v}_{\psi p} \frac{B_p^2}{B^2} + \vec{v}_{\psi\theta} \frac{B_\theta^2}{B^2} \right] \qquad \text{V-5}$$

where $\vec{v}_{\psi p}$ and $\vec{v}_{\psi\theta}$ have been inserted as separate fictitious field line velocities. We know that $\vec{v}_{\psi p} = \vec{v}_{\psi\theta}$ when $\vec{E}\cdot\vec{B} = 0$. Thus the bracket, which is v_D, the particle drift is equal to

$$\vec{v}_D = \vec{v}_\psi \left| \frac{B_p^2 + B_\theta^2}{B^2} \right| = \vec{v}_\psi \qquad \text{V-6}$$

The particle drift velocity is equal to the field line velocity. This is an aspect of Newcomb's theorem for the case of $\vec{E}\cdot\vec{B} = 0$ (Chapter II). If $\vec{v}_{\psi p} \neq \vec{v}_{\psi\theta}$ because $\vec{E}\cdot\vec{B} \neq 0$ then the particle drift is given by

$$\vec{v}_D = \vec{v}_{\psi p} \frac{B_p^2}{B^2} + \vec{v}_{\psi\theta} \frac{B_\theta^2}{B^2} \qquad \text{V-7}$$

and differs from the line velocities.

Another special case is the Ware pinch drift frame which moves with the separate fictitious poloidal field line velocity in a toroidal system with both toroidal and poloidal fields.[2]

$$\vec{v}_w = \frac{\vec{E} \times \vec{B}_p}{B_p^2} \qquad \text{V-8}$$

In this drifting coordinate system

$$\vec{E} = -\dot{\vec{A}}_\theta - \dot{\vec{A}}_p + \frac{\vec{E}_\theta \times \vec{B}_p}{B_p^2} \times \vec{B}$$

which takes the form

$$\vec{E} = \vec{E}_\theta + \vec{E}_p - \left| \vec{E}_\theta \frac{(\vec{B}\cdot\vec{B}_p)}{B_p^2} - \vec{B}_p \frac{(\vec{B}\cdot\vec{E}_\theta)}{B_p^2} \right|$$

$$= \vec{E}_p + (\vec{E}_\theta \cdot \vec{B}) \frac{\vec{B}_p}{B_p^2} \qquad \text{V-9}$$

Eqn. 9 shows that in the Ware pinch frame, in which trapped particle banana orbits are carried, the electric field is completely poloidal in direction. This electric field pushes the bananas off the central plane and contributes electrons to the conduction current by untrapping a fraction of the trapped electrons (Chapter VII).

For all these cases of moving field lines and drifting plasma it is only the component of E parallel to B that is needed for evaluation of plasma conductivity.

A. Average parallel electric field[3,4]

The parallel electric field can be calculated in terms of the inductive voltage generated along a field line.

$$V_{ab}(\psi,t) = \int_a^b \vec{E}\cdot d\vec{\lambda} \qquad \text{V-10}$$

The integration in eqn. 10 is carried out along the path illustrated in Figure 1. Because of azimuthal symmetry the integral can be broken up into a toroidal term and a poloidal term as follows

$$V_{ab} = -\int_a^b \dot{\vec{A}}\cdot R d\theta\hat{\theta} - \int_a^b \dot{\vec{A}}\cdot d\ell_p\hat{p}$$

$$= -\int_0^{\Delta\theta} \frac{\partial A_\theta}{\partial t} R d\theta - \oint \frac{\partial A_p}{\partial t} d\ell_p \qquad \text{V-11}$$

$\Delta\theta$ is the distance the field line advances in the θ direction for one loop around poloidally

$$\Delta\theta = \oint \frac{B_\theta d\ell_p}{RB_p} \qquad \text{V-12}$$

$\Delta\theta$ is plotted versus position in Figure 2b. Note that outside the separatrix the field line encloses all four hoops and $\Delta\theta$ is larger than the case of a private field line enclosing only one hoop. A_θ and A_p are the vector potentials defined by

$$\vec{B}_p = \vec{\nabla} \times \vec{A}_\theta$$

$$\vec{B}_\theta = \vec{\nabla} \times \vec{A}_p$$

A_θ can be written in terms of the poloidal flux function $\psi = 2\pi RA_\theta$. Applying Stoke's theorem to the second integral on the right of eqn. 11 gives

$$V(\psi,t) = -\frac{\partial\psi}{\partial t}\frac{\Delta\theta(\psi)}{2\pi} - \frac{\partial\Phi(\psi,t)}{\partial t} \qquad \text{V-13}$$

where Φ is the θ flux inside a ψ line and is illustrated in Figures 1 and 2. The time dependence of the flux functions ψ and Φ can be written

in terms of the magnetic field variation

$$\frac{\partial\psi}{\partial t} = \frac{\dot{B}_p}{B_p}\psi_{core}\frac{\psi}{10}$$

$$\frac{\partial\Phi}{\partial t} = \frac{\dot{B}_\theta}{B_\theta}\Phi(\psi)$$

ψ_{core} = .423 Wb with 2.5 kV on the B_p capacitor bank.[5] Finally, eqn. 10 can be written in the form

$$V(\psi,t) = \frac{\dot{B}_p}{B_p}.423\ \text{Wb}\ \frac{\psi}{10}\frac{\Delta\theta(\psi)}{2\pi} - \frac{\dot{B}_\theta}{B_\theta}\Phi(\psi,t) \qquad \text{V-14}$$

The second term in eqn. 14 retains the minus sign since E_p is anti-parallel to B_p according to the sign convention of Figure 1. The first term is positive because E_θ is parallel to B_θ. Eqn. 14 can be used to determine where and when $V(\psi,t) = 0$. Setting the left side of eqn. 14 equal to zero and rearranging gives the expression below

$$\frac{.423\ \text{Wb}}{\Phi(\psi,t)}\frac{\psi}{10}\frac{\Delta\theta(\psi)}{2\pi} - \frac{\dot{B}_\theta}{B_\theta}\frac{B_p}{\dot{B}_p} = 0 \qquad \text{V-15}$$

The first term of eqn. 15 is plotted in Figure 3 for $t = 25$ msec. The second term varies spatially and temporally and is determined by measuring $\dot{B}_\theta B_p/B_\theta\dot{B}_p$ at different points. The value of $\dot{B}_p/B_p$ depends on the location within the machine. The two terms of eqn. 15 are plotted on the same graph and the intersections of the two curves give the

locations of $V(\psi,t) = 0$. If B_p and B_θ have the same time variations (as when B_p and B_θ are driven in series) then $\dot{B}_\theta B_p / B_\theta \dot{B}_p = 1$ throughout ψ space. This value is plotted as the horizontal dotted line in Figure 3. It is seen that $V = 0$ between $\psi = 3$ and $\psi = 4$ (see also the plot of $E_\parallel$ at $t = 25$ msec in Figure 5).

In general $V(\psi,t)$ will equal zero at only one, two, or three points in ψ space depending on the value of $\dot{B}_\theta B_p / B_\theta \dot{B}_p$. In order for $V(\psi,t)$ to equal zero for all values of ψ the two terms of eqn. 15 would have to cancel at every ψ. This does not occur for any of the field configurations used on the octupole.

The average electric field is obtained by dividing $V(\psi,t)$ by $L(\psi,t)$, where $L(\psi,t)$ is the length of the field line and is determined by the following equations.

$$(d\ell)^2 = (d\ell_p)^2 + (Rd\theta)^2$$

$$= (d\ell_p)^2 + (d\ell_p)^2 \frac{B_\theta^2}{B_p^2}$$

$$L = \oint d\ell_p \left(1 + \frac{B_\theta^2}{B_p^2}\right)^{1/2} \qquad \text{V-16}$$

$$E_{\parallel ave} = V_{ab}/L \qquad \text{V-17}$$

The integral in eqn. 16 is taken once around poloidally. $L(\psi)$ is plotted in Figure 4 for $t = 25$ msec. Figure 5 is a plot of the average $E_\parallel$ versus time and position for B_p and B_θ driven in series with a half

sine wave time dependence. At early times in the pulse (3 msec) the electric field is antiparallel to B. The electric field inside the hoop is zero because very little flux has soaked in. Later in the pulse (15 msec) the electric field has decreased because field lines are entering the machine at a slower rate. Magnetic flux has soaked into the hoop and induces an electric field within the hoop. At peak field (22 msec) the gap voltage is zero and no magnetic field lines are entering or leaving the machine. The electric field within the machine is due entirely to field lines soaking into the hoops and walls. Somewhere between the hoop and the wall the electric field is zero. This point is called the watershed. Later in the pulse (31 msec) the electric field is parallel to B. This is due to magnetic field lines leaving the machine through the gap. Note that field lines are still soaking into the hoops and walls.

B. Local electric fields

In some situations the value of the induced electric field at a point on a ψ surface is needed, rather than the electric field on the ψ surface averaged once around the hoop. The electric field felt by a highly collisional plasma is the local value. The electrons in such a plasma experience many momentum randomizing collisions in a trip once around the hoop. After each collision the parallel velocity is zero and the force on the electron is determined by the local value of $E_\parallel$.

A time changing poloidal magnetic field induces an electric field in the toroidal direction. The magnitude of the field can be calculated from the flux function ψ.[5]

$$\psi = 2\pi R A_\theta$$

$$E = -\frac{1}{2\pi R}\frac{\partial \psi}{\partial t}\hat{\theta} \qquad \text{V-18}$$

Local toroidal electric fields can be calculated from eqn. 18 using computer generated values of ψ versus time and position in the octupole.

A time changing toroidal magnetic field induces an electric field in the poloidal direction. The electric field can be calculated from the time changing vector potential.

$$\vec{A}(x) = \frac{\mu_o}{4\pi}\int \frac{\vec{J}(x')}{|x-x'|}\, d^3x' \qquad \text{V-19}$$

J(x') in eqn. 19 is the current distribution which produces the toroidal magnetic field and is illustrated in Figure 6a. Current flows through the walls of the octupole in the poloidal direction. There are also image currents flowing the short way around the hoop. The vector potential was calculated numerically from eqn. 19 by approximating the current in the walls by 24 filament currents. The vector potential in a constant azimuth plane consists of an r-and a z-component. The toroidal field can be obtained from

$$B_\theta = \vec{\nabla} \times \vec{A} = \frac{\partial A_r}{\partial z} - \frac{\partial A_z}{\partial r} \qquad \text{V-20}$$

Figure 7 is a plot of the calculated B_θ and B_θ measured with a Hall probe at 25 msec and 30 msec. The calculated B_θ agrees reasonably well with the measured B_θ except near the wall where the filament current

is strong and causes azimuthal variations.

With combined toroidal and poloidal magnetic fields there is a component of the induced electric field which is parallel to the magnetic field and causes a plasma current to flow. The parallel electric field is obtained by dotting the total electric field into the normalized magnetic field.

$$E_\parallel = (\hat{r}E_r + \hat{z}E_z + \hat{\theta}E_\theta)\cdot\frac{(\hat{r}B_r + \hat{z}B_z + \hat{\theta}B_\theta)}{(B_r^2 + B_z^2 + B_\theta^2)^{1/2}}$$

$$= (\hat{p}E_p + \hat{\theta}E_\theta)\cdot\frac{\hat{p}B_p + \hat{\theta}B_\theta}{(B_p^2 + B_\theta^2)^{1/2}}$$

The local value of $E_\parallel$ along $\psi = 5$ at 25 msec is plotted in Figure 8. The local $E_\parallel$ ranges from .1 V/m in the high field region to .3 V/m in the low field region. The variation of $E_\parallel$ can be seen more easily in Figure 8b which shows $E_\parallel$ along $\psi = 5$. The thickness of the line is proportional to the parallel electric field. It is evident that $E_\parallel$ is large where B is small and $E_\parallel$ is small where B is large. This is caused by the geometry of the magnetic fields. The flux lines in the low field region move more rapidly and thus induce a higher electric field.

The average parallel electric field can be calculated from the local value as follows

$$E_{\parallel ave} = \frac{\oint \vec{E}_\parallel \cdot d\vec{\ell}}{L} = \frac{\Sigma E_\parallel \Delta\ell}{L} \qquad \text{V-22}$$

where L is the length of the field line given by eqn. 16. The integral

in eqn. 22 is replaced by a sum and is computed numerically. Average parallel electric fields calculated from eqn. 22 were found to agree within 10% with those calculated from eqn. 17.

References for Chapter V

1. W. A. Newcomb, Ann. Phys., 3,347(1958)
2. A. A. Ware, Phys. Rev. Lett., 25,916(1970)
3. D. E. Lencioni, Univ. of Wisc. Ph.D. Thesis, PLP 276 (1969)
4. J. F. Etzweiler, Univ. of Wisc. Ph.D. Thesis, PLP 738 (1977)
5. J. R. Drake, PLP 512 (1973)
6. D. Morin, PLP 523 (1973)

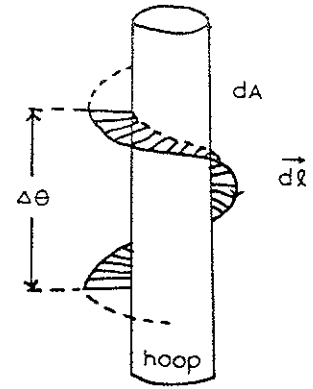

a. Integration along a field line once around the hoop

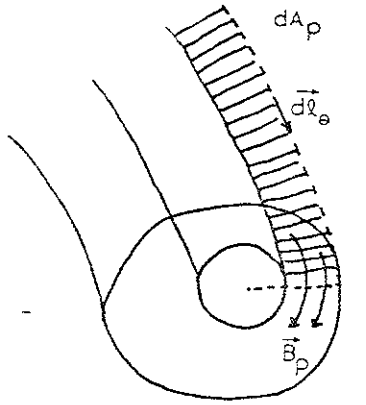

b. Poloidal flux $\Phi_p = \int B_p dA_p$

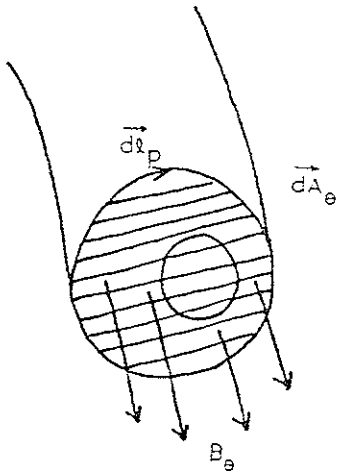

c. Toroidal flux $\Phi_\theta = \int B_\theta dA_\theta$

Figure V-1

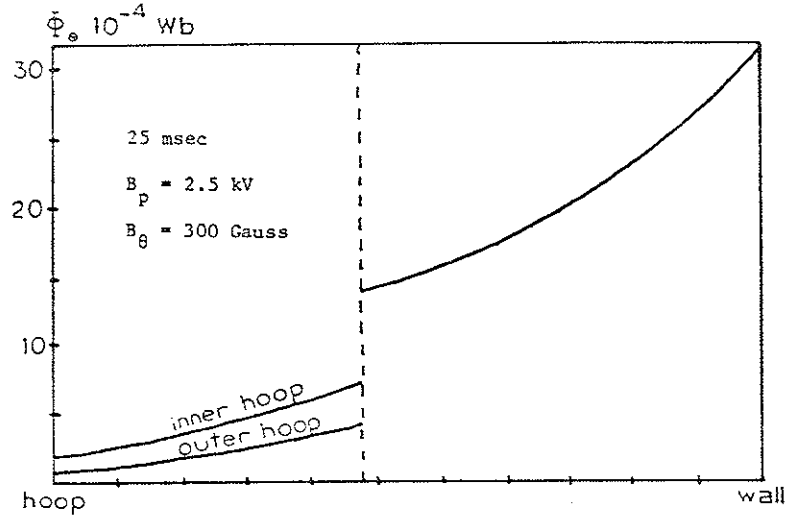

a. Toroidal flux versus position

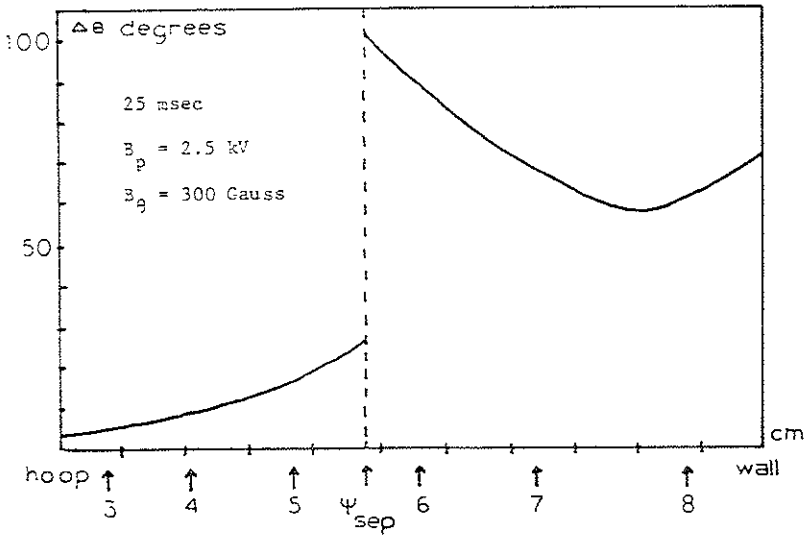

b. Δθ versus position

Figure V-2

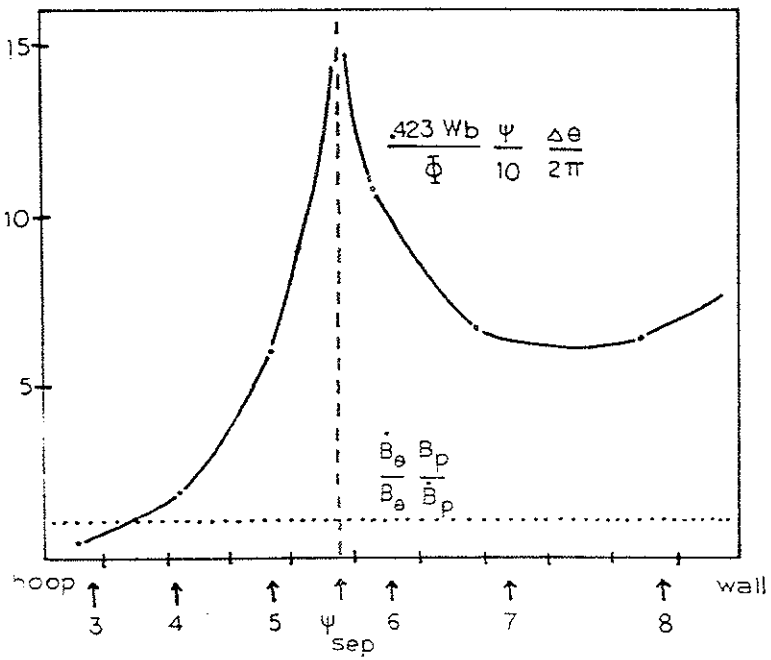

Figure V-3

Plot of $\frac{.423\ \text{Wb}}{\Phi(\psi,t)} \frac{\psi}{10} \frac{\Delta\theta(\psi)}{2\pi} - \frac{\dot{B}_\theta}{B_\theta} \frac{B_p}{\dot{B}_p} = 0$

2.5 kV B_p cap bank, B_θ = 300 Gauss, t = 25 msec

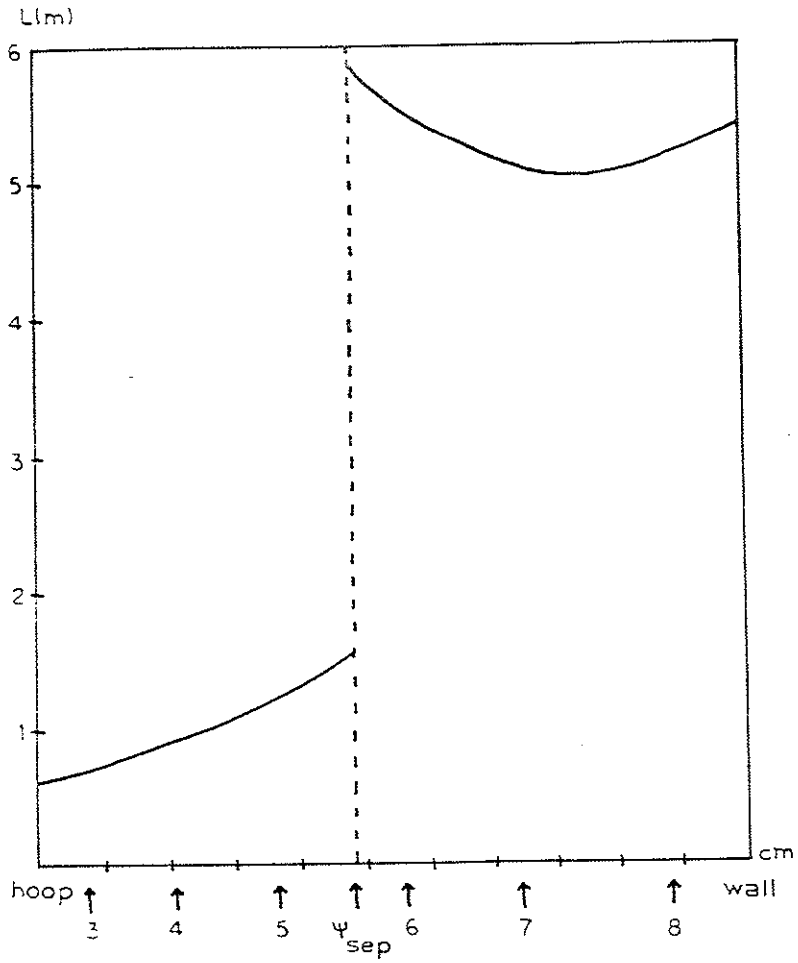

Figure V-4

Length of field line versus position in the bridge region at 25 msec. B_p = 2.5 kV, B_θ = 300 Gauss on midcylinder.

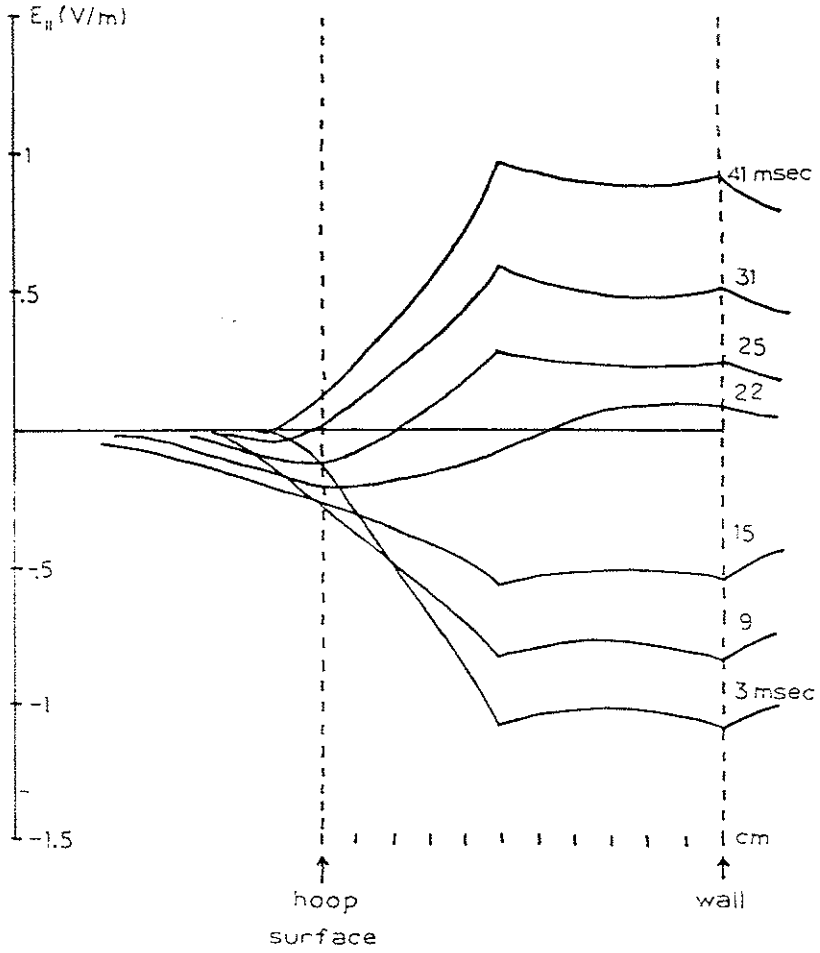

Figure V-5

Average parallel electric field versus position and time. B_p & B_θ sine wave, 2.5 kV

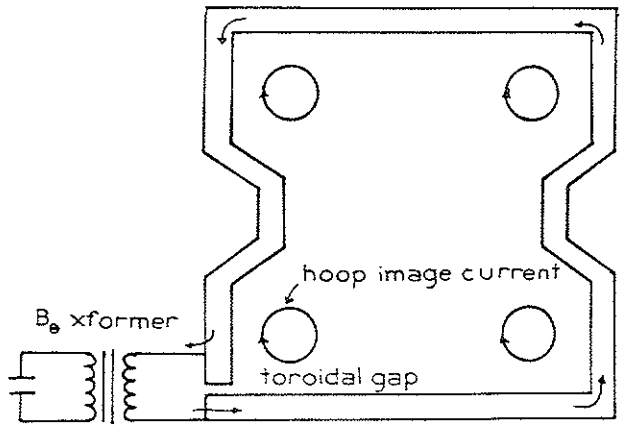

a. Production of B_θ field by driving current through the walls in the poloidal direction.

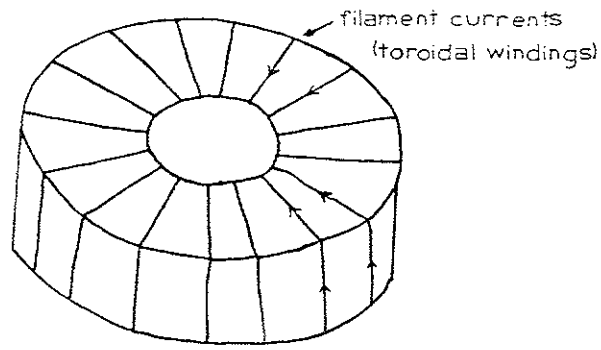

b. Approximating the continuous wall currents with a finite number of filament currents.

Figure V-6

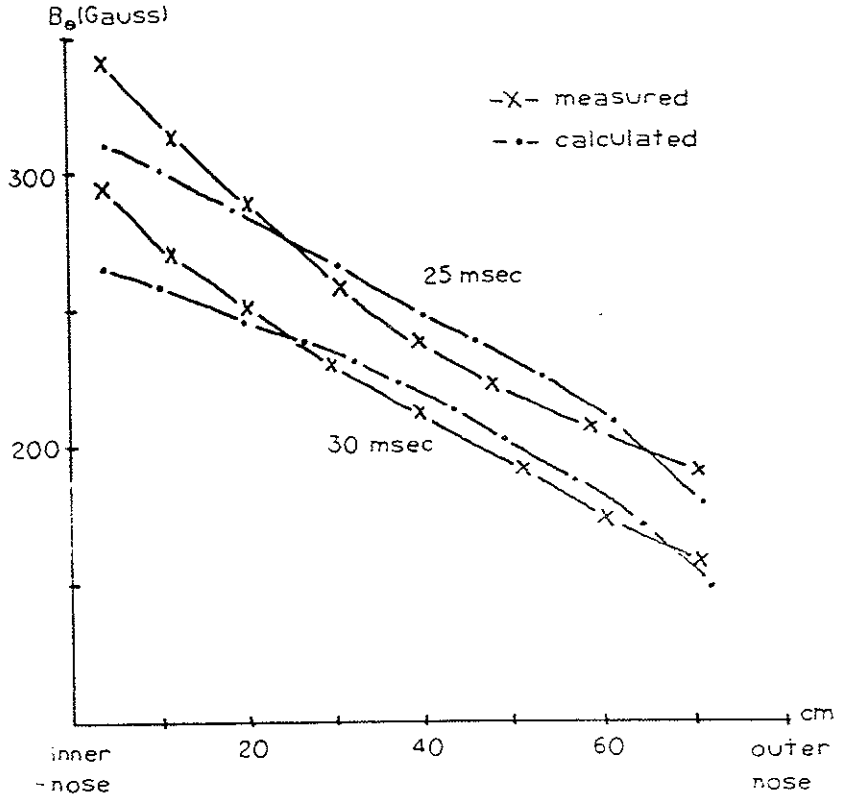

Figure V-7

Comparison between measured and calculated values of B_θ on the midplane. B_θ calculated from eqn. V-5.

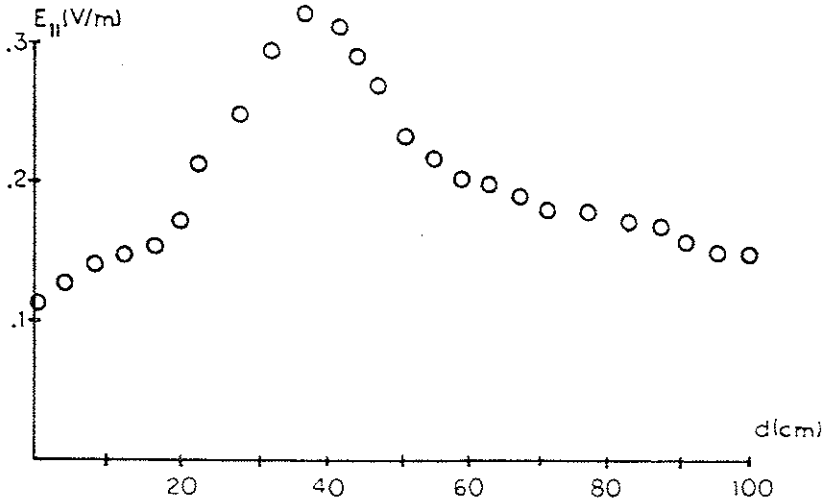

a. Parallel electric field along ψ = 5 at 25 msec

B_p & B_θ sine wave, 2.5 kV

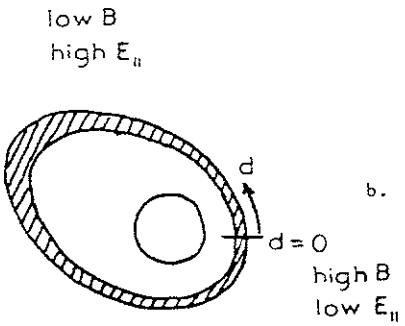

b. Variation in $E_\parallel$ along ψ

Figure V-8

Chapter VI

Single Particle Motion in the Octupole Magnetic Field

The equation of motion of a nonrelativistic particle with charge q and mass m in an electric and magnetic field is

$$m\ddot{\vec{r}} = q(\vec{E} + \dot{\vec{r}} \times \vec{B}) \qquad \text{VI-1}$$

This equation can be iterated to determine the position and velocity of the particle versus time. The iteration steps must be small for it is necessary to follow the particle around its gyro-orbit. The gyrofrequency of an electron in a 1.5 kGauss magnetic field is 4×10^9 Hz which causes the iteration period for eqn. 1 to be less than a nanosecond.

The iteration period can be longer if the particle motion is approximated by the guiding center motion.[1,2] The gyration of the particle around a field line is ignored and the motion of the guiding center is followed. The nonrelativistic guiding center equations of motion are:

$$\frac{dv_\parallel}{dt} = \frac{q}{m}\frac{\vec{E}\cdot\vec{B}}{B} - \mu\frac{\vec{\nabla}B\cdot\vec{B}}{m}\frac{\vec{B}}{B} \qquad \text{VI-2}$$

$$v_\perp = \frac{\vec{E}\times\vec{B}}{B^2} - \mu\frac{\vec{\nabla}B\times\vec{B}}{qB^2} + \frac{mv_\parallel^2}{q}\frac{\vec{B}}{B^2}\times\left(\frac{\vec{B}}{B}\cdot\vec{\nabla}\right)\frac{\vec{B}}{B} \qquad \text{VI-3}$$

The first right hand term of eqn. 2 is the force on the particle due to the component of the electric field parallel to the magnetic field line. The second term is the force due to magnetic mirrors. Since μ is conserved, a particle with a small parallel velocity will be reflected

by the magnetic mirror.

The first term on the right hand side of eqn. 3 is the E x B drift. The second and third terms are drifts due to the nonuniform magnetic field and curvature of the field lines.

Equations 2 and 3 were solved with a Runge-Kutta algorithm. The iteration step was 10^{-9} second. A plot of particle position versus time for an electron is illustrated in Figure 1. The poloidal and toroidal fields were assumed to be crowbarred perfectly so that no electric field was induced. The electron was started in the low field region as indicated in Figure 1. Initial velocity was 2×10^6 m/sec parallel to the field line. This corresponds to a 10 eV electron with $\mu = 0$. Figure 1 shows that the electron circulates around the hoop without being reflected in the high field region. The time between points is 1×10^{-8} sec. Note that the points are equally spaced in distance as the electron circles around the hoop.

Figure 2 is a plot of particle position versus time for an electron started in the low field region with $\mu = 4.6 \times 10^{-18}$ kg m^4/Wb sec^2. This corresponds to a 10 eV electron with the velocity perpendicular to the field line equal to the velocity parallel to the field line initially. The mirror ratio for $\psi = 5$ is $M = B_{min}/B_{max} = .17$. A particle with $v_\perp > .42\ v$ should be trapped. This is indeed the case as illustrated in Figure 2. The time between points is 1×10^{-8} sec. Note that the distance between points decreases as the electron enters the high field region. This is due to parallel velocity being converted to perpendicular velocity in order to conserve μ. The particle is reflected when $v_\parallel = 0$.

Figure 3 is a plot of particle position versus time for a hydrogen ion

started in the low field region with $\mu = 8.4 \times 10^{-19}$ kg m^4/Wb sec^2. This corresponds to a 10 eV ion with $v_{\parallel} = v_{\perp}$ initially. This particle is also expected to be trapped. Figure 3 shows the ion trajectory. The time between points is $.5 \times 10^{-6}$ sec. Note again that the distance between points decreases as the particle nears the high field region. Figure 3 shows that the ion follows a banana orbit due to the ∇B drift. This is not noticeable in Figure 2 for the corresponding electron orbit. The maximum banana width for the 10 eV ion is about .7 cm as can be seen in Figure 3. At the point of maximum banana width the poloidal field is 340 Gauss. The ion gyroradius is 1.3 cm for a 10 eV hydrogen ion in a 340 Gauss field. These observations agree with the fact that absolute containment zones are unaffected by the addition of a toroidal field. Thus the excursion of a particle in ψ-space due to the banana trajectories is no greater than the gyroradius of that particle in the B_p only field.

Notice that the banana opens toward the center of the machine and closes near the wall. This is because the poloidal field strength is stronger near the hoops than at the center of the machine. The toroidal field strength dominates in a tokamak and the bananas behave just the opposite; opening towards the outer wall and closing near the inner wall where the toroidal field strength is highest.[3]

Figure 4 is a plot of particle position versus time for an electron with $\mu = 0$ in a sine wave B_p and B_θ field. Poloidal and toroidal electric fields are induced by the time changing magnetic fields. The full set of eqns. 2 and 3 must be used to determine the particle motion. The electric field perpendicular to the field line causes a drift in addition to the

∇B and curvature drift. Initial velocity of the electron was 1.86×10^6 m/sec parallel to the field line. This corresponds to a 10 eV electron with $\mu = 0$. After one orbit around the loop the parallel velocity has increased to 1.89×10^6 m/sec. The electron has gained approximately .2 eV in energy from the parallel electric field.

A. Orders of magnitude: ∇B drift, curvature drift, E x B drift

A comparison of Figures 1 and 4 shows little difference in the particle trajectories. Figure 1 is the trajectory of a particle in perfectly crowbarred magnetic fields ($E = 0$). Figure 4 is the trajectory of a particle in sine wave B_p and B_θ fields ($E \neq 0$). Any effects due to E x B drifts are not apparent. Similarly ∇B and curvature drifts are not evident in either case, the particle trajectory follows the magnetic field lines. An average value of the E x B drift once around the hoop can be obtained as follows

$$\langle v \rangle = \frac{1}{L} \int_a^b \frac{(E_p \hat{p} + E_\theta \hat{\theta}) \times (B_p \hat{p} + B_\theta \hat{\theta})}{B^2} \, d\ell \qquad \text{VI-4}$$

The integral in eqn. 4 is evaluated once around the hoop poloidally. L is the length of the field line. The integral was evaluated point by point along the field line $\psi = 5$ and the results are plotted in Figure 5a. The drift velocity varies between .4 m/sec and 5 m/sec, being highest in the low field region. The average drift velocity is $\langle v \rangle = 2.2$ m/sec. It takes a 10 eV electron 10^{-6} sec to circle the hoop so the maximum displacement of the electron due to E x B drift is 2.2×10^{-6} m for each transit around the hoop. This distance is not noticeable on the scale

of Figures 1 and 4.

The drift velocity due to ∇B and curved field lines can be written as[4]

$$v_d = \frac{m}{q}\frac{R \times B}{R^2 B^2}\left(v_\parallel^2 + \frac{1}{2}v_\perp^2\right) \qquad \text{VI-5}$$

where R is the radius of curvature of the field line. Eqn. 5 can be split up into two components; one in the theta direction and one perpendicular to the ψ surface. The component perpendicular to ψ averages to zero for a circuit around the hoop if v does not change. The component in the theta direction is plotted in Figure 5b. The average drift velocity is 43 m/sec. A 10 eV electron requires 10^{-6} sec to circle the hoop so the maximum displacement would be 4×10^{-5} m which is not noticeable on the scale of Figures 1 and 4. The theta component of the ∇B drift lengthens or shortens the path of the particle by a negligible amount in one circuit around the hoop.

B. Trapped particle drift - Ware pinch[5]

In the toroidal octupole the vector potential A_θ does not depend on the θ coordinate (axisymmetry).

$$\vec{A}_\theta = \hat{\theta}A_\theta(R,Z) \qquad \text{VI-6}$$

The Hamiltonian of a charged particle in the octupole field is given by

$$H = \frac{1}{2m}\left|P_R^2 + P_Z^2 + \left(\frac{P_\theta}{R} - \frac{e}{c}A_\theta(R,Z)\right)^2\right| \qquad \text{VI-7}$$

Since θ is an ignorable coordinate, the θ canonical momentum is conserved.[6]

$$\frac{dP_\theta}{dt} = 0$$

$$P_\theta = mR^2\dot{\theta} + \frac{e}{c}RA_\theta = \text{constant} \qquad \text{VI-8}$$

$$\frac{d}{dt}\left|R\left(\frac{mv_\parallel B_\theta}{B} + \frac{e}{c}A_\theta\right)\right| = 0 \qquad \text{VI-9}$$

where $v_\parallel$ is the particle velocity parallel to B and R is the radius measured from the major axis. For a trapped particle, $v_\parallel$ will go to zero at the turning points. Consider two consecutive turning points occurring at r and $r + \Delta r$ at times t and $t + \Delta t$. Eqn. 9 can be written as

$$\Delta r\frac{\partial}{\partial r}(RA_\theta) + \Delta t\, R\frac{\partial A_\theta}{\partial t} = 0 \qquad \text{VI-10}$$

where the convective derivative has been used

$$\frac{d}{dt} = \frac{\partial}{\partial t} + \vec{v}\cdot\vec{\nabla} \qquad \text{VI-11}$$

and r is the particle radius measured from the hoop if the particle is on a private flux line or from the midplane-midcylinder intersection if the particle is on a common flux line. Using $\vec{B} = \vec{\nabla} \times \vec{A}$ and $E_\theta = -\partial A_\theta/\partial t$ eqn. 10 can be written as

$$\Delta r B_p + \Delta t E_\theta = 0 \qquad \text{VI-12}$$

$$\frac{\Delta r}{\Delta t} = -\frac{E_\theta}{B_p} \qquad \text{VI-13}$$

From eqn. 13 it is evident that the trapped particle banana orbits drift radially inward toward the hoops or toroid center depending on the flux surface (private or common). The trapped particles are effectively tied to B_p field lines and follow the motion of the B_p field lines with velocity

$$\vec{v}_W = \frac{\vec{E}_\theta \times \vec{B}_p}{B_p^2} \qquad \text{VI-14}$$

This can be seen by writing $\psi(R,Z,t) = 2\pi R A_\theta(R,Z,t)$ and using eqn. 8 to obtain

$$\frac{P_\theta}{R} - \frac{e}{c}\frac{\psi(R,Z,t)}{2\pi R} = mR\dot{\theta} \qquad \text{VI-15}$$

at the bounce point $\theta = 0$, so eqn. 15 becomes

$$P_\theta = \frac{e}{c}\frac{\psi(R,Z,t)}{2\pi} = \text{const.} \qquad \text{VI-16}$$

At later times $\psi(R,Z,t) = \psi(R_o,Z_o,t_o)$, so the ψ function determines the R,Z locus of the bounce points. Thus the trapped particles move with the $\psi_{poloidal}$ surface.

The trapped particle drift velocity is plotted in Figure 5a. Note that the trapped particle drift velocity in the octupole is only about a factor of two greater than the E x B drift velocity of untrapped particles.

Conclusion: To determine the plasma conductivity we need to know how an electron responds to an applied electric field. From the above

calculations of drift velocities and electron transit times it is clear that to first order one can neglect ∇B drift, curvature drift, and E x B drift and assume that an electron follows the magnetic field line while being accelerated by the component of the electric field parallel to the field line. Plasma conductivity is determined by measuring $J_\parallel$ in the lab frame and dividing by $E_\parallel$ as calculated in Chapter V. Trapped electrons contribute to the plasma current only if they are scattered into the loss cone or if the component of E parallel to B_p is strong enough to accelerate them into the loss cone (see Chapter VII).

C. Newcomb's theorem: Field line motion and particle motion[7]

The concept of freezing of lines of force in a perfectly conducting medium is due to Alfven.[8] Although the conductivity of a medium will never be infinite, the applicability of frozen lines was shown to depend on a dimensionless number

$$L = Bd\sigma\sqrt{\mu/n}$$

where B is the magnetic induction in Wb/m^2, d is a linear dimension in meters, σ is electrical conductivity, μ is the permeability of the plasma, and n is the density.

Frozen lines of force are valid when $L \gg 1$. This condition can be satisfied easily in extraterrestrial phenomena because of the large values of d, but is more difficult to satisfy in the laboratory due to finite values of d and σ. Values of $L > 10^3$ can be obtained for laboratory plasmas. $L = 4000$ for the little gun plasma with $n = 5 \times 10^9$ cm^{-3}, $\sigma = 10^2\ \Omega^{-1}m^{-1}$, $d = 1$ m, $B = .1$ Wb/m^2. In a laboratory plasma

the magnetic field lines can diffuse through the plasma so that particle motion and field line motion are different and we can no longer consider the field lines to be frozen in the plasma.

Newcomb has shown that certain conditions are satisfied if particle motion and field line motion are equivalent. A field line is not an observable in itself. Only certain consequences of the concept can be observed. Newcomb describes moving magnetic field lines as follows. There exists a family of lines ℓ, moving with velocity v, such that four properties are satisfied.

(1) Through every point of space passes exactly one of the lines ℓ.

(2) The lines ℓ remain tangent to B in the course of their motion.

(3) The density of lines ℓ is equal to the intensity of the magnetic field.

(4) The emf around a closed curve moving in an arbitrary manner is equal to minus the total number of lines ℓ cut by the circuit per unit time.

The condition for v to be flux preserving is derived by computing the time rate of change of the flux Φ through an arbitrary cycle c moving with velocity v.

$$\frac{d\Phi}{dt} = \int \dot{\vec{B}}\cdot\hat{n}dA + \oint \vec{B}\cdot(\vec{v} \times d\vec{\ell}) \qquad \text{VI-17}$$

The surface integral in eqn. 17 is due to the time variation of B at a fixed point. The line integral is due to flux being included due to the motion of the boundary. Eqn. 17 can be written as

$$\frac{d\Phi}{dt} = -\int |\vec{\nabla} \times (\vec{E} + \vec{v} \times \vec{B})|\cdot\hat{n}dA \qquad \text{VI-18}$$

A necessary and sufficient condition for flux preservation is that v satisfy the following equation.

$$\vec{\nabla} \times (\vec{E} + \vec{v} \times \vec{B}) = 0 \qquad \text{VI-19}$$

The guiding center of a charged particle in electric and magnetic fields will drift with velocity

$$v_d = \frac{E \times B}{B^2} \qquad \text{VI-20}$$

Substituting this drift velocity into eqn. 19 gives the condition for particle motion and field line motion to be identical.

$$\vec{\nabla} \times \left(\vec{E} + \frac{\vec{E} \times \vec{B}}{B^2} \times \vec{B}\right) = 0 \qquad \text{VI-21}$$

$$\vec{\nabla} \times \frac{\vec{B}(\vec{E}\cdot\vec{B})}{B^2} = 0 \qquad \text{VI-22}$$

For the poloidal field only sine wave case eqn. 22 is satisfied identically since $\vec{E}\cdot\vec{B} = 0$. Thus one can say that the particles are tied to the B_p field lines. Motion of the plasma along the field lines is not affected, but as the field lines move transversely the plasma is carried along.

In the B_p and B_θ sine wave case electric fields are induced in the toroidal and poloidal directions. This leads to a component of E which is parallel to B and eqn. 17 is no longer satisfied. Figure 6 is a plot of the magnitude of $\vec{\nabla} \times \vec{B}(\vec{E}\cdot\vec{B})/B^2$ versus position for the field line $\psi = 5$ at 25 msec. Figure 6 shows that eqn. 17 is not satisfied at any

point on the field line. For the B_p and B_ϑ sine wave case we cannot apply Newcomb's theorem. To determine what the particle motion is in this case we must proceed as in section VI-A and solve the guiding center equations of motion point by point using values of magnetic fields and electric fields calculated at these points.

References for Chapter VI

1. G. Schmidt, Physics of High Temperature Plasmas, Academic Press, N.Y., 1966
2. L. L. Lao, R. W. Conn, and J. Kesner, Single particle orbits in a tandem mirror, UWFDM-245 (1978)
3. A. A. Galeev and R. Z. Sagdeev, Sov. Phys. - JETP, 26,233(1968)
4. F. F. Chen, Introduction to Plasma Physics, Plenum Press, N.Y., 1974
5. A. A. Ware, Phys. Rev. Lett., 25,916(1970)
6. H. Goldstein, Classical Mechanics, Addison-Wesley Publishing Co., Reading, Mass., 1950
7. W. A. Newcomb, Ann. Phys., 3,347(1958)
8. H. Alfven and G. G. Falthammer, Cosmical Electrodynamics, 2nd ed., Oxford Univ. Press, London, 1963

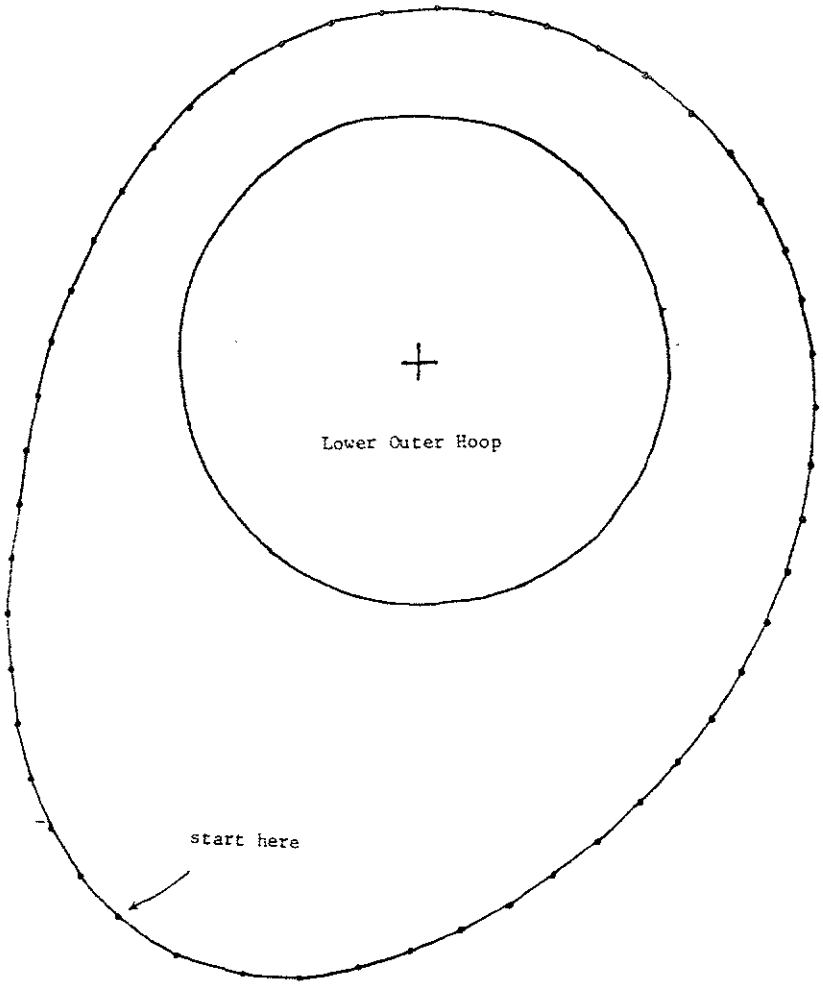

10 eV electron with $\mu = 0$

Perfectly crowbarred fields $\Sigma_\mu = 0$

$\Delta t = 1 \times 10^{-8}$ sec

Figure VI-1

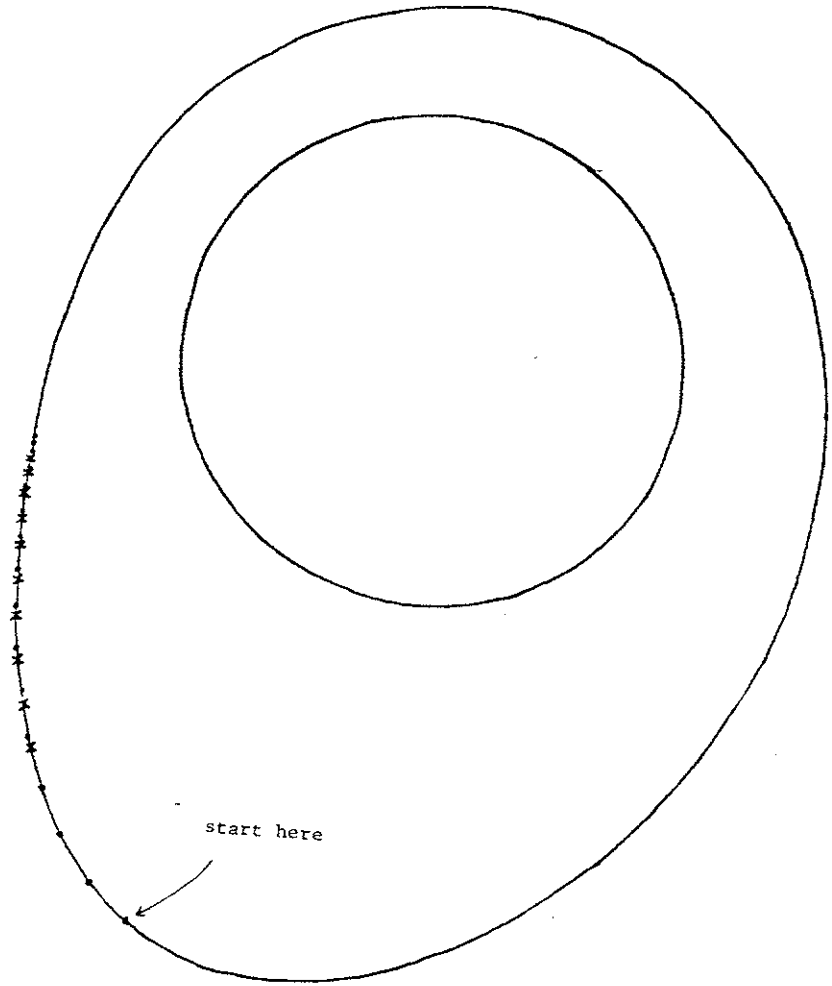

10 eV electron with $\mu = 4.6 \times 10^{-18}$ kg m^4/Wb sec^2

Perfectly crowbarred fields $E = 0$

$\Delta t = 1 \times 10^{-8}$ sec

Figure VI-2

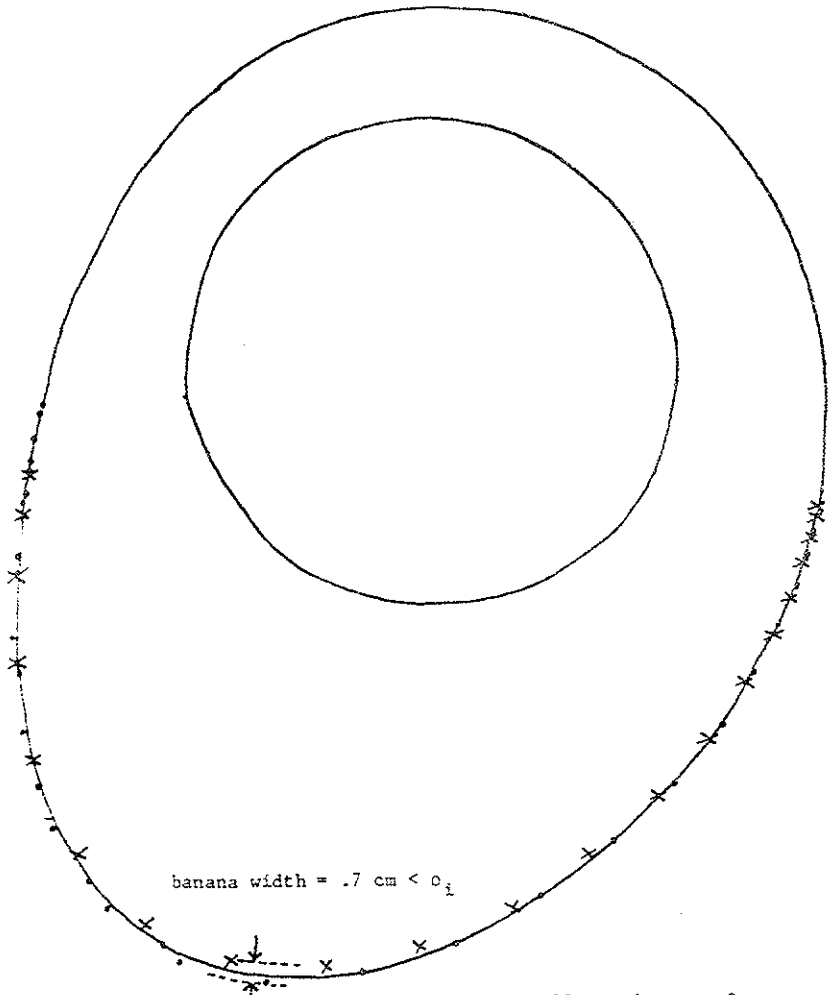

10 eV hydrogen ion with $\mu = 8.4 \times 10^{-19}$ kg m^4/Wb sec^2

Perfectly crowbarred fields E = 0

$\Delta t = .5 \times 10^{-6}$ sec

Figure VI-3

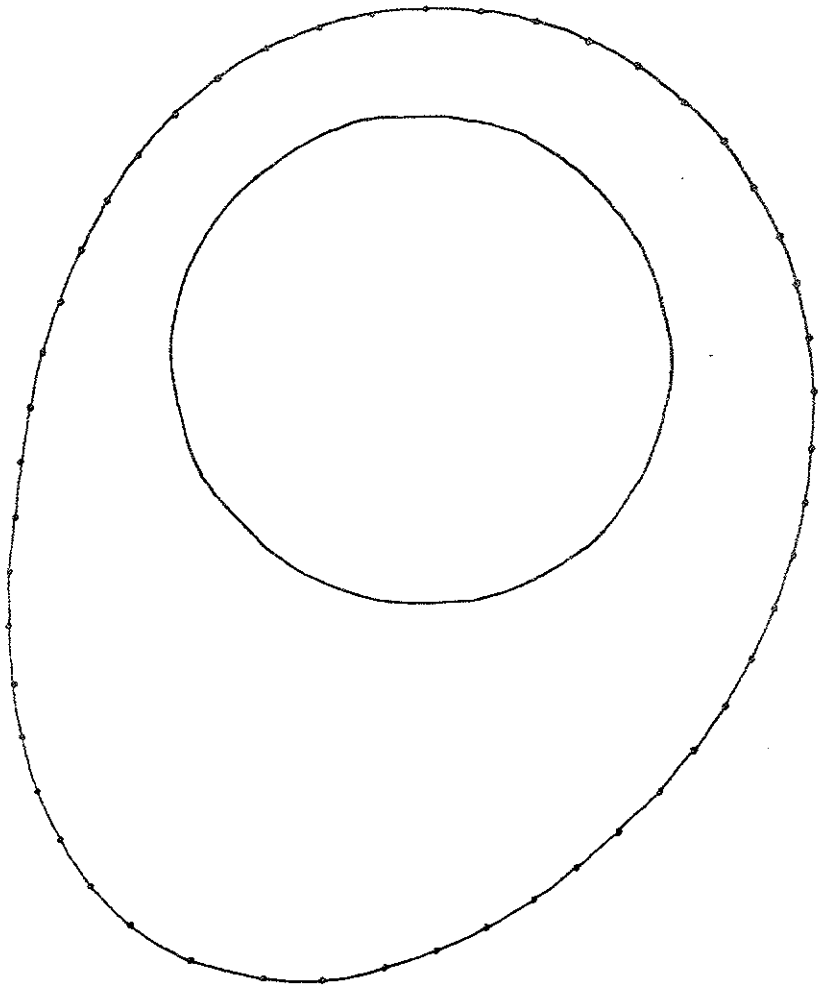

10 eV electron with $\mu = 0$

B_p & B_θ sine wave, 2.5 kV on B_p cap bank

$\Delta t = 1 \times 10^{-8}$ sec

Figure VI-4

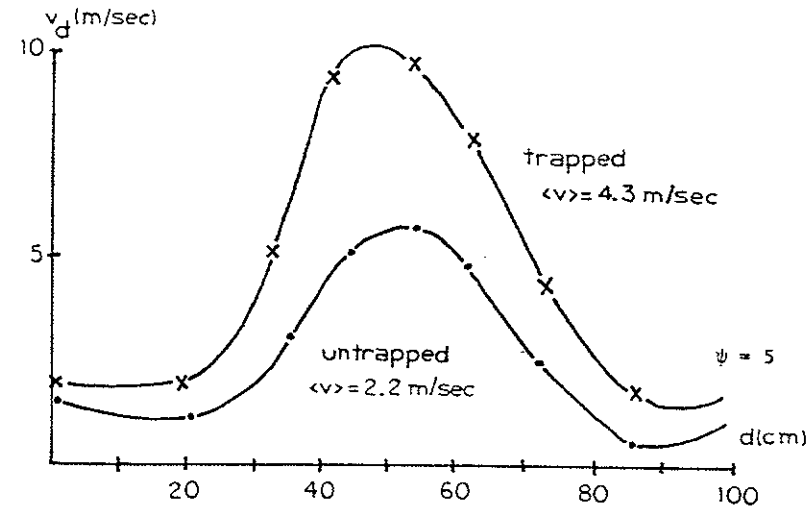

a. Drift velocity due to E x B

B_p and B_θ sine wave, 2.5 kV, 25 msec

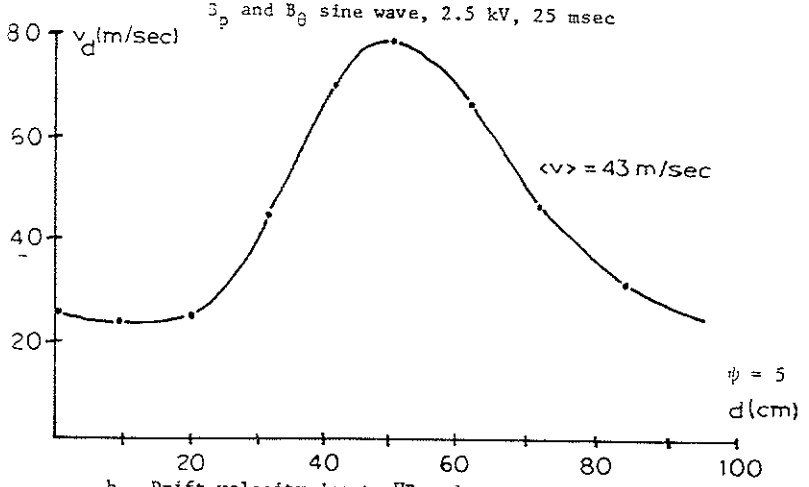

b. Drift velocity due to ∇B and curved field lines

B_p and B_θ sine wave, 2.5 kV, 25 msec

Figure VI-5

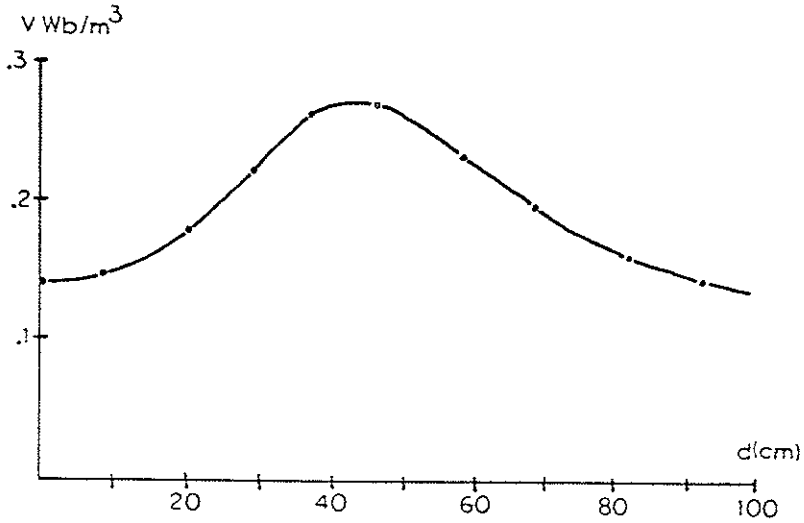

Plot of the quantity $\left|\frac{\vec{B} \times \vec{B}(\vec{E}\ \vec{B})}{B^2}\right|$ versus position on ψ = 5

B_p and B_θ sine wave, 2.5 kV, 25 msec

Figure VI-6

Chapter VII

Theoretical Conductivity

A. Classical Spitzer conductivity

When an electric field is applied to a plasma the electrons are accelerated by the $-e\vec{E}$ force. In steady state the electric force is balanced by a dynamical friction force which is due to collisions between electrons and ions. The resistivity in the steady state is given by

$$\eta = \frac{m\nu_{ei}}{ne^2} \qquad \text{VII-1}$$

where m is the electron mass and n is the plasma density. ν_{ei} is the effective frequency at which electrons suffer collisions which change their direction of travel by 90^0. This leads to ohmic heating whereby the directed energy which the electrons gain from the electric field is converted into random thermal motion. Ohmic heating occurs as a result of electron-ion collisions only since electron-electron collisions do not alter the total momentum and therefore do not contribute to the dynamical friction.

Spitzer[1,2] has shown that the rate of ohmic heating and the dynamical friction force are indirectly influenced by electron-electron collisions since the form of the velocity distributions plays a role in the electron-ion encounters. Electron-electron collisions exchange random energy very efficiently and a Maxwellian distribution tends to be established.

Spitzer showed that ν_{ei} can be decomposed into two terms. The first

term is due to electrons with small impact parameters undergoing large angle scattering from ions. The second term is due to electrons with large impact parameters undergoing small angle scattering. Because of the inverse square Coulomb force the cumulative effect of the small angle scattering at large impact parameters is more important than the effect of occasional large deflections at small impact parameters. Thus one can think of the scattering as being due to numerous small angle encounters which add up to 90^0 after a time τ_{eff}. The effective frequency for 90^0 scattering due to small angle encounters leads to the following form for the conductivity

$$\sigma = \frac{2(2kT)^{3/2}}{\pi^{3/2} m_e^{1/2} Ze^2 c^2 \ell n\Lambda} \qquad \text{cgs units} \qquad \text{VII-2}$$

$$\sigma = 1.9 \times 10^4 \frac{T_e^{3/2}\ (eV)}{\ell n\Lambda} \quad \Omega^{-1} m^{-1} \qquad \text{VII-3}$$

where $\ell n\Lambda$ is the Coulomb logarithm.

$$\Lambda = \frac{\lambda_D}{P_o} \qquad \text{VII-4}$$

$$P_o = \frac{Ze^2}{m_e v_e^2} \qquad \text{VII-5}$$

λ_D is the Debye length. P_o is the impact parameter for a 90^0 Coulomb collision. $\ell n\Lambda$ ranges in value from 10 to 30. σ in eqn. 3 is given in MKS units with Z = 1.

Spitzer conductivity is valid for a fully ionized plasma in which

the applied electric field is low enough so that the directed energy gained by an electron in a mean 90^0 scattering period is much less than the thermal energy. Dreicer[3] has shown that larger electric fields lead to runaway electrons. The Rutherford differential scattering cross section is given by

$$\frac{d\sigma}{d\Omega} = \left(\frac{Ze^2}{4\pi\epsilon_o mv^2}\right)^2 \frac{1}{\sin^4\theta/2} \qquad \text{VII-6}$$

where Z is the ionic charge, θ is the scattering angle and n and v are the electron mass and velocity. Due to the rapid decrease in the cross section at high electron velocities the dynamic friction force, which depends on the electron-ion collisions, also decreases at high electron velocities. The forces which act on electrons can thus be split into two regimes. At low electron velocities the dynamic friction force is high and is able to balance the force due to the electric field. At high electron velocities the dynamic friction force is low and is unable to balance the electric force. High velocity electrons are continuously accelerated by the electric field until they run away subject to relativistic effects.

B. Dreicer critical field for production of runaways[3]

Dreicer likened the dynamic friction force to a fictitious electric field $E' = E_c F(z)$, where E_c is the critical field and z is the ratio of electron drift velocity to electron thermal velocity. The function F(z) is given by

$$F(z) = \frac{\Phi(z) - z\Phi'(z)}{z^2} \qquad \text{VII-7}$$

where $\Phi(z)$ is the error function.

$$\Phi(z) = \frac{2}{\sqrt{\pi}} \int_0^z e^{-t^2} dt \qquad \text{VII-8}$$

F(z) is plotted in Figure 1. In the limit of small z, F(z) takes the form

$$F(z) \to \frac{4}{3\sqrt{\pi}} z \qquad \text{VII-9}$$

In this limit the dynamic friction force is able to balance the force due to the applied electric field and a steady state results in which $\sigma \propto T_e^{3/2}$ as predicted by Spitzer.

In the limit of large z, F(z) takes the form

$$F(z) \to \frac{1}{z^2} \qquad \text{VII-10}$$

In this limit the dynamic friction force is unable to balance the force due to the electric field and the velocity of the electrons increases. Notice from eqn. 10 that the dynamic friction force grows smaller and smaller as the velocity increases and thus the electron velocity runs away.

The critical electric field at which runaway occurs is given by

$$E_c = \frac{\nu_{ei} mv}{e} = 10^{-10} \frac{n(cm^{-3})}{T_e(eV)} \quad V/m \qquad \text{VII-11}$$

E_c is plotted versus density and temperature in Figure 1b. Also plotted are the parameter ranges of the three gun plasmas studied. Notice that the critical field for the high density, low temperature big gun plasma is quite high (≈ 10 V/m) and exceeds the typical induced electric field (≈ .1 V/m) by more than an order of magnitude. The critical field for the low density, high temperature little gun plasma is very small (≈ .01 V/m) and the induced electric field exceeds the critical field by an order of magnitude. The intermediate gun plasma once again shows its intermediate nature. The induced electric field is less than the critical field in some regions and greater than the critical field in other regions.

These considerations lead us to conclude that Spitzer conductivity may not be applicable to the little gun and intermediate gun plasmas because of the large applied electric fields. If we cavalierly apply Spitzer conductivity to the three guns and compare with the experimentally observed conductivities (Chapter VIII) the results below are obtained:

	$n_e(cm^{-3})$	$T_e(eV)$	$\sigma_{Spitzer}(\Omega^{-1}m^{-1})$	$\sigma_{exp}(\Omega^{-1}m^{-1})$
big gun	2×10^{12}	1	1200	10^3
int. gun	2×10^{11}	10	37900	$10^3 - 10^4$
little gun	5×10^{9}	10	37900	$10^2 - 10^3$

Only the big gun results are in agreement with the theoretical prediction based on Spitzer conductivity. Spitzer conductivity cannot be applied to little gun and intermediate gun plasmas.

C. Discussion:

Three points are worthy of discussion in regard to electron runaway.

(1) If the electron distribution is Maxwellian there exists a small fraction of high velocity electrons in the distribution which interact so infrequently with ions that almost any applied electric field will cause them to run away. Even though the electric field is less than E_c for the bulk of the electrons it is greater than E_c for a small number of high velocity electrons in the tail of the distribution. These electrons are said to be in the "slide away" regime[4] because that part of the distribution which sees $E > E_c$ slides away from the rest of the distribution.

(2) If the ohmic heating causes the electron temperature to increase, the bulk of the electrons may eventually run away. This is due to the T_e^{-1} dependence of E_c. Although the applied electric field was originally lower than E_c the increase in T_e due to ohmic heating will eventually cause E to appear higher than E_c to the plasma even though the magnitude of E has not changed.

(3) The runaway electrons cause assymmetries to appear in the electron velocity distribution. These assymetries can act as energy sources for exciting plasma instabilities. The two-stream instability[5] has often been observed when a plasma is subjected to a high electric field. The instability takes energy from the drifting electrons and limits the final velocity which they can achieve.

D. Electron-neutral collisions

Spitzer resistivity was derived from eqn. 1 by assuming ν_{ei} (effective

90^0 scattering frequency) was due to electron-ion interactions. The ν_{ei} is responsible for the so called dynamic friction force seen by the electron. The ν predicted by Spitzer conductivity is obviously too low in the little gun plasma ($\nu_{Spitzer} = 2 \times 10^4\ s^{-1}$, $\nu_{exp} = 10^5 - 10^6\ s^{-1}$). There are other effects besides electron-ion collisions which cause ν to assume higher values.

If the neutral gas background density is high eqn. 1 can be written as

$$\eta = \frac{m\nu_{en}}{ne^2} \qquad \text{VII-12}$$

where ν_{en} is the frequency of electrons scattering off neutrals. ν_{en} differs fundamentally from ν_{ei} in that it is caused mainly by electrons with small impact parameters which undergo large angle scattering from the neutral. Long range interactions like those in Coulomb scattering do not occur in electron-neutral collisions.

Gilardini[6] gives experimental cross sections for momentum transfer in electron-neutral collisions. ν_{en} can be determined from

$$\nu_{en} = n_g v Q_m \qquad \text{VII-13}$$

where n_g is the density of neutral gas, v is the electron velocity and Q_m is the momentum transfer cross section in $\mathring{A}^2$. For a Maxwellian distribution of electron velocities eqn. 13 becomes

$$\nu_{en} = n_g \frac{\int v f(v) Q_m(v) dv}{\int f(v) dv} \qquad \text{VII-14}$$

This calculation was done by Smith[7] for hydrogen neutrals. His results for $T_e = 10$ eV are

$$\nu_{en} = 2 \times 10^{-7}\ n_g\ sec^{-1} \qquad \text{VII-15}$$

where n_g is measured in cm^{-3}.

The little gun plasma was fired through a drift tank before it entered the octupole tank. The drift tank served to delay the entry of streaming neutrals from the gun. Background neutral pressures remained at about 10^{-7} Torr for 20 msec after gun injection. Fast pressure gauge measurements[8] indicate that the background pressure remains less than 10^{-6} Torr until 100 msec after gun injection. At a background pressure of 1×10^{-7} Torr the hydrogen neutral density is $n_g = 3 \times 10^9\ cm^{-3}$. This value substituted in eqn. 15 gives

$$\nu_{en} = 630\ sec^{-1} \qquad \text{VII-16}$$

This is much lower than the electron-ion collision frequency for the little gun plasma with $T_e = 10$ eV.

$$\nu_{ei} = \nu_{Spitzer} = 2 \times 10^4\ sec^{-1} \qquad \text{VII-17}$$

The electron-neutral collision frequency does not become comparable to ν_{ei} until the background pressure of hydrogen rises to 5×10^{-6} Torr.

Combining the effects of electron-ion and electron-neutral collisions gives a resistivity in the following form

$$\eta = \frac{m\nu_{ei}}{ne^2} + \frac{m\nu_{en}}{ne^2} \qquad \text{VII-18}$$

i.e. the resistivities add in series to produce the total resistivity. If $\nu_{ei} >> \nu_{en}$ then the effects of electron-neutral collisions can be neglected. This illustrates a general result: the highest collision frequency causing 90^0 scattering of electrons determines the value of the resistivity.

We can conclude from the above arguments that the anomalously high resistivity observed in the little gun plasma is not due to electron-neutral collisions.

The intermediate density gun fired directly into the octupole without an intervening drift tank. The rise in neutral background in this case occurred more rapidly than for the little gun but the peak background density was not observed to rise higher than 2-3 x 10^{-6} Torr during the field pulse. Again we must conclude that the electron-neutral collision frequency isn't high enough to explain the anomalous resistivity observed with the intermediate gun.

E. Mirror trapping[9,10]

Particle trapping in the octupole magnetic field geometry is caused by the variation in magnetic field strength on a flux surface. Figure 2 is a plot of M versus ψ at peak field. M is the mirror ratio and is defined as the ratio of the maximum field strength on a flux surface to the minimum field strength.

$$M = \frac{B_{max}}{B_{min}} \qquad \text{VII-19}$$

Notice that $M = \infty$ on the separatrix in the B_p only case. This is due

to the field null on the midcylinder separatrix. When a toroidal magnetic field is added there is no longer a field null and M assumes finite values for all ψ-space. With $B_\theta = 300$ Gauss on axis M ranges in value from 2 to 10 in the private flux of the outer hoop and from 4 to 10 in the common flux.

Due to conservation of magnetic moment the charged particles on a flux surface are separated into two groups; trapped and circulating. The circulating particles have sufficient parallel velocity at B_{min} to allow them to pass through B_{max} after conservation of μ is satisfied. The criterion for circulating particles defines a loss cone in velocity space.

$$\sin^2\theta_{lc} = \frac{v_{\perp o}^2}{v_{\perp o}^2 + v_{\parallel o}^2} < \frac{1}{M} \qquad \text{VII-20}$$

where $v_{\perp o}$ and $v_{\parallel o}$ are the perpendicular and parallel velocities evaluated at B_{min}. Any particle within the loss cone is a circulating particle. The fraction of the electrons which are circulating particles is an important parameter. Only the circulating electrons are able to carry a current in response to an applied E field. The trapped electrons gain energy from the electric field during half of their bounce path but give the energy back during the other half. The electric field has no net effect on the trapped fraction of electrons. For an isotropic distribution the fraction of electrons that are circulating is given by

$$f_{ut} = 1 - \sqrt{1 - 1/M} \qquad \text{VII-21}$$

f_{ut} versus ψ is plotted in Figure 2b. f_{ut} is low due to the strong magnetic mirrors in the octupole geometry. On the separatrix less than 10% of the electrons are circulating. f_{ut} ranges from .1 to .3 in other regions of the machine. In a Tokamak geometry the magnetic mirrors are caused by the 1/R variation of the toroidal field. This leads to mirror ratios of about 1.5. f_{ut} for a Tokamak is about .7 which is much higher than values of f_{ut} for the octupole.

If the parallel electric field is strong enough additional electrons can become untrapped in the following manner. If an electron starts at B_{min} with an initial $v_{\perp 0}$ it will gain energy from the electric field and $v_{\parallel}$ will increase. If $v_{\perp 0}$ is low enough the additional parallel energy gained from the electric field will allow the electron to pass through B_{max} and become a circulating particle. Taking into account the detrapping due to the electric field modifies f_{ut} as follows[10]

$$f_{ut} = 1 - \sqrt{1 - 1/M}\, \exp\left(\frac{\gamma}{M-1}\right) \qquad \text{VII-22}$$

where $$\gamma = \frac{eE_{\parallel} L_{bounce}}{kT_e} \qquad \text{VII-23}$$

L_{bounce} is the length along the field line between B_{min} and B_{max}. γ versus ψ is plotted in Figure 3. γ is less than .02 throughout ψ-space and therefore $\exp(\gamma/(M-1))$ is very close to unity. The parallel electric field in this case affects the degree of electron trapping to a negligible extent. This is not the case in the small octupole which has a higher E due to the shorter field pulse and higher magnetic fields. The small octupole value of $\exp(\gamma/(M-1))$ has a small but noticeable effect on electron trapping.

F. Resistivity effects due to mirror trapping

Resistivity effects due to mirror trapping depend on the collisionality of the plasma. Some of the collision frequencies which need to be considered are:

(1) ν_{ei}, the effective 90^0 scattering frequency of electrons due to electron-ion collisions. ν_{ei} is obtained from the value of Spitzer resistivity.

$$\eta_S = \frac{m\nu_{ei}}{ne^2} = \frac{T_e^{-3/2}}{1200} \quad \Omega m \qquad \text{VII-24}$$

where T_e is in eV.

(2) ν_b, the electron bounce frequency

$$\nu_b = v_e / L_m \qquad \text{VII-25}$$

where v_e is the electron thermal velocity and L_m is the mirror length.

(3) $\nu_{\ell c}$, the frequency at which circulating electrons are scattered out of the loss cone. If the scattering is due to electron-ion collisions the small angle collisions cause a random walk of the electrons in velocity space which gives

$$\nu_{\ell c} = \left(\frac{\pi}{2\theta_{\ell c}}\right)^2 \nu_{ei} \qquad \text{VII-26}$$

The value of the resistivity depends on which of the collision frequencies is highest.

(1) $\nu_{ei} >> \nu_b$, highly collisional plasma. An electron can scatter in and out of the loss cone many times during its bounce period. Therefore,

particle trapping effects play no role in determining the value of resistivity. Since ν_{ei} is the highest collision frequency the plasma should exhibit Spitzer resistivity.

(2) $\nu_{ei} \ll \nu_b$, highly collisionless plasma. In this case the electrons divide into a trapped and a circulating fraction. Only the circulating fraction can respond to a parallel electric field and carry a current. The mirrors change the effective collision time to one related to scattering out of the loss cone rather than for 90^0 scattering. This increases the effective frequency to $\nu_{eff} = \nu_{\ell c} = (\pi/2\theta_{\ell c})^2 \nu_{ei}$. The resistivity takes the form

$$\eta_{mirror} = \frac{m\nu_{eff}}{f_{ut} ne^2} = \left(\frac{\pi}{2\theta_{\ell c}}\right)^2 \frac{\eta_S}{f_{ut}} \qquad \text{VII-27}$$

Eqn. 27 says that the mirror dominated resistivity is an enhanced value of Spitzer resistivity. η_{mirror} is position dependant and varies from $13\eta_S$ at the hoop to $100\eta_S$ at the separatrix.

(3) $\nu_{ei} < \nu_b < \nu_{\ell c}$, transition region between collisionless and collisional behavior. This is somewhat of a twilight zone where both mirror effects and electron-ion collisions must be considered. Although circulating electrons are scattered out of the loss cone at a frequency $\nu_{\ell c}$ they continue to act as current carriers until a time L_m/v_e later when they bounce in the mirror. Thus the effective frequency for 90^0 scattering is $\nu_{eff} = v_e/L_m = \nu_b$ and the resistivity takes the form

$$\eta = \frac{mv_e}{ne^2} \frac{1}{f_{ut} L_m} \qquad \text{VII-28}$$

The factor f_{ut} occurs in the denominator because only the circulating fraction of electrons is able to carry the current.

An examination of eqn. 28 shows that the effective mean free path between scattering events, λ_{eff}, is $f_{ut} L_m$. f_{ut} and L_m depend only weakly on plasma parameters. L_m is a property of the magnetic field structure and f_{ut} depends mainly on the mirror ratio. Because of the approximate independence of λ_{eff} from the plasma parameters the transition region is often referred to as the "plateau" regime.

G. Mirror effects in Tokamaks

The three regimes of collisionality just discussed correspond exactly to the three regimes of neoclassical transport theory:[11] banana (collisionless), plateau (transitional), and Pfirsch-Schluter (collisional). Rosenbluth, Hazeltine, and Hinton[12,13] used a variational principle for the rate of entropy production to solve the Boltzman equation for the transport coefficients in a Tokamak geometry. In the banana regime the conductivity was determined to be

$$\eta = \eta_S / f_{ut} \qquad \text{VII-29}$$

In a Tokamak $(\pi/2\theta_{\ell c})^2 \approx 1$ so eqn. 29 agrees with eqn. 27 derived above. f_{ut} is about .7 for a Tokamak so $\eta \approx 1.4\eta_S$. Rosenbluth, Hazeltine, and Hinton assert that this mirror enhancement together with high Z impurities explains the anomalous resistivity (factor of 3-5) measured in the T-3 and ST Tokamaks.

H. Turbulent resistivity[14,15,16]

If a large electric field ($E > E_c$) is applied to a plasma the velocity distribution of electrons will be distorted from a Maxwellian. Two examples of this distortion are a shifted Maxwellian and a Maxwellian with a bump on the tail. The parallel electron drift energy caused by the applied electric field can act as an energy source for exciting plasma instabilities. Detailed observations of such instabilities allows one to relate these instabilities to sources of free energy in the bulk plasma. Some of the free energy sources available for driving instabilities are ∇n, ∇T, and drifting electrons.

In unstable plasmas, fluctuations in density and potential are greatly enhanced over the thermal equilibrium level and scattering of individual particles by collective fluctuation fields due to instabilities can become a major dissipation mechanism. When this occurs ν_{eff} due to electron-fluctuation interactions can become orders of magnitude larger than ν_{ei} or ν_{en} and thus will determine the value of the resistivity. The resistivity is then called turbulent resistivity.

A turbulent plasma is defined as one which exhibits a large number of random collective oscillations which are excited by the presence of an instability. Weak turbulence occurs when $E_f < E_{kin}$, where E_f is the energy density associated with the unstable fluctuations and E_{kin} is the mean particle kinetic energy density.

$$E_{kin} = \frac{3}{2}nkT \qquad \text{VII-30}$$

Strong turbulence occurs when $E_f \approx E_{kin}$. There exists a voluminous literature dealing with weakly turbulent plasmas. Strongly turbulent

plasmas have been studied less due to the theoretical problems in dealing with them.

The little gun and intermediate gun plasmas exhibited weak turbulence. Typical values of $\delta n/n$ of .02 to .03 were observed in ion saturation and electron saturation currents collected by Langmuir probes. Assuming that the total energy in a plasma wave is composed of equal parts of electrostatic energy and kinetic energy gives the fluctuation energy as $E_f \approx .04 - .06E_{kin}$ and thus the conditions for weak turbulence are satisfied.

Weak turbulence theory can be discussed in terms of three basic interactions: the nonlinear wave-wave interaction, the linear (or quasilinear) wave-particle interaction, and the nonlinear wave-particle interaction.

(1) Nonlinear wave-wave interaction: This interaction is sometimes referred to as resonant wave-wave scattering or the decay instability. Resonance conditions for this interaction are

$$\omega_3 = \omega_1 \pm \omega_2 \qquad \text{VII-31}$$

$$\vec{K}_3 = \vec{K}_1 \pm \vec{K}_2 \qquad \text{VII-32}$$

where ω_1, ω_2, ω_3 and $\vec{K}_1$, $\vec{K}_2$, and $\vec{K}_3$ are the frequencies and wave numbers of the three waves involved in the interaction. Eqns. 31 and 32 are the conditions for conservation of energy and momentum when two waves beat to form a third. Two high frequency electron waves (ω_1, $\vec{K}_1$) and (ω_2, $\vec{K}_2$) can beat to form an amplitude envelope traveling at a velocity

$$(\omega_2 - \omega_1)/(\vec{K}_2 - \vec{K}_1) \simeq d\omega/dK = v_g \qquad \text{VII-33}$$

Nonlinear wave-wave interactions must be considered when calculating the turbulent frequency spectrum. Such interactions are only important for dispersion relations $\omega_K = \omega(K)$ for which it is possible to satisfy eqns. 31 and 32 simultaneously. The third wave formed by the two beating waves may have v_g low enough to be affected by wave-particle interactions even though such interactions were not effective at ω_1/K_1 and ω_2/K_2.

(2) Linear (or quasi-linear) wave-particle interaction: Wave-particle interactions are associated with the resonance condition

$$\omega = \vec{K}\cdot\vec{v} \qquad \text{VII-34}$$

where v is the particle velocity. When a particle and a wave satisfy eqn. 34 a resonant interaction occurs in which the electric field of the wave is constant in the particle frame of reference, and therefore a large energy exchange can take place between the particle and the wave.[17] This resonant process only involves particles with velocity $v \simeq v_\phi$, where v_ϕ is the phase velocity of the wave. If a particle has $v < v_\phi$ or $v > v_\phi$ it sees a rapidly fluctuating electric field and cannot effectively exchange energy. This is illustrated in Figure 4 which shows phase-space trajectories for electrons moving in a potential wave.[18] The arrows show the direction of electron motion relative to v_ϕ. Electrons with $v > v_\phi$ move to the right. Electrons with $v < v_\phi$ move to the left. Electrons with $v = v_\phi$ (resonant electrons) remain stationary in the wave frame. Also shown are trajectories for trapped electrons. These trajectories occur for a range of velocities where

the particle kinetic energy is insufficient to climb out of the potential well created by the wave. The particles bounce back and forth in the well and are carried along by the wave.

Particle trapping leads to quasilinear effects. Quasilinear theory is a nonlinear theory because the rate of change of the wave amplitude depends on the distribution function, and the rate of change of the distribution function in turn depends on the wave amplitude.

The change in amplitude of the wave caused by wave-particle interactions is referred to as Landau damping (or growth). Figures 4b, c, and d illustrate the effects of Landau damping on three different initial velocity distributions.

b) Maxwellian velocity distribution. The phase velocity of the wave occurs at a point where $\partial f/\partial v < 0$. The wave is Landau damped. Low energy particles gain energy from the wave and become high energy particles. This causes a high energy tail to appear in the velocity distribution and effectively leads to particle heating.

c) Drifting Maxwellian velocity distribution. The phase velocity of the wave occurs at a point where $\partial f/\partial v > 0$. The wave grows. The energy source is the drift energy of the electrons. Quasilinear effects try to bring the distribution back to a Maxwellian without a drift. As in b) the random particle energy increases leading to a high energy tail. The drift energy is thus divided between wave energy and particle heating. The wave amplitude saturates due to nonlinear effects.

d) Bump on the tail distribution. The phase velocity of the wave occurs at a point where $\partial f/\partial v > 0$. The wave grows. Energy is obtained from the drifting beam. The wave again saturates due to nonlinear effects.

(3) Nonlinear wave-particle interactions: This interaction is sometimes referred to as nonlinear Landau damping. This interaction and the nonlinear wave-wave interaction are referred to collectively as mode coupling. The resonance condition is

$$(\omega_2 \pm \omega_1) = (\vec{K}_2 \pm \vec{K}_1)\cdot v \qquad \text{VII-35}$$

The interaction is similar to the wave-particle interaction except that now the particle maintains a constant phase relative to the beats of the two waves.

I. Experimental turbulent resistivity

Figure 5 shows results obtained from Hamberger[19] and Demidov.[20] Resistivity values are plotted versus applied electric field. The measurements were made in a toroidal discharge chamber. Large values of parallel electric field could be induced by discharging capacitors into circumferential windings around the torus. Density and temperature were $n_e \simeq 10^{12}$ cm^{-3}, $T_e \simeq 2$ eV. With these conditions Spitzer conductivity is $\sigma_S \simeq 10^{13}$ esu and the Dreicer critical field is $E_c \simeq 2$ V/cm. Three regimes of resistivity were observed. Spitzer conductivity was observed when $E < E_c$. For electric fields 1 V/cm $< E <$ 25 V/cm the conductivity exhibited a plateau an order of magnitude lower than Spitzer. For electric fields $E >$ 25 V/cm a second plateau in σ was seen; this one about 2 orders of magnitude below Spitzer.

Hamberger attributes the first plateau to turbulent resistivity due to ion acoustic turbulence. A power spectrum of the fluctuations

observed in this regime is shown in Figure 5b. All of the power occurs at frequencies below f_{pi}. The second plateau is attributed to turbulent resistivity due to the ion-electron two stream instability. A power spectrum of the fluctuations in this regime is shown in Figure 5c. Most of the power occurs near f* which is the predicted fastest growth frequency.

$$f^* = \frac{1}{2}\left(\frac{M}{m}\right)^{1/6} f_{pi} \qquad \text{VII-36}$$

Buneman[9] has studied the effect of the two-stream instability on plasma conductivity. Directed electron energy is dissipated into random energy by "collective collisions" with the ions, i.e., collisions in bunches. A mechanism for the buildup of bunches from small fluctuations was described and the conductivity was predicted to be

$$\sigma_B \simeq \frac{1}{2}\left(\frac{M}{m}\right)^{1/3} \omega_{pe} \qquad \text{VII-37}$$

Using $n_e \simeq 10^{12}$ cm^{-3} gives $\sigma_B \simeq 3 \times 10^{11}$ sec^{-1} which agrees very well with the conductivity observed by Hamberger at high electric fields.

Similar experiments have been performed by Hirose[21,22] on a toroidal glass-walled discharge chamber. Inductive electric fields of $\simeq$ 50 V/cm were applied to an Argon plasma with density $\simeq 10^{12}$ cm^{-3}. Anomalous resistivities (factor 10-100) were observed and these were attributed to current driven ion acoustic instability and beam-plasma instability. At lower values of E the conductivity agreed with that calculated by Dupree.[23]

$$\sigma = \frac{(32\pi)^{1/2}}{K\lambda_D}\,\omega_{pe} \qquad \text{VII-38}$$

where K is an average wave vector parallel to the current flow and λ_D is the Debye length. Dupree derived eqn. 38 by considering the dynamical friction force between ballistic clumps of plasma which are formed through resonant scattering of particles by the waves.

Figure 6 shows experimental conductivity versus electric field in the C stellerator. Anomalously high resistivity (factor of 2-5) is seen when $E < E_c$. Coppi and Mazzucato[24] have explained this anomaly in terms of out-of-phase density and temperature fluctuations associated with current driven instabilities which lead to a decrease in the electric field which is effective in driving the current. The instabilities were drift-type modes which occur in plasmas having density and temperature gradients. The modes were found to be excited when the electron drift velocity exceeded a threshold which was on the order of the ion acoustic velocity.

References for Chapter VII

1. L. Spitzer Jr., Physics of Fully Ionized Gases, 2nd ed., Wiley, N.Y., 1962
2. L. Spitzer and R. Harm, Phys. Rev., 89,977(1953)
3. H. Dreicer, Phys. Rev., 115,238(1959)
4. A. A. M. Oomens, L. T. M. Ornstein, R. R. Parker, F. C. Schuller and R. J. Taylor, Phys. Rev. Lett., 36,255(1976)
5. O. Buneman, Phys. Rev., 115,503(1959)
6. A. Gilardini, Low Energy Collisions in Gases, John Wiley & Sons, N.Y., 1972
7. P. K. Smith, PLP 682 (1976)
8. D. A. Brouchous, PLP 648 (1975)
9. D. E. Lencioni, Univ. of Wisc. Ph.D. Thesis, PLP 276 (1969)
10. J. F. Etzweiler, Univ. of Wisc. Ph.D. Thesis, PLP 738 (1977)
11. A. A. Galeev and R. Z. Sagdeev, Sov. Phys.-JETP, 26,233(1968)
12. R. D. Hazeltine, F. L. Hinton, and M. N. Rosenbluth, Phys. of Fluids, 16,1645(1973)
13. R. D. Hazeltine, F. L. Hinton, and M. N. Rosenbluth, Phys. of Fluids, 15,116(1972)
14. B. B. Kadomtsev, Plasma Turbulence, Academic Press, N.Y., 1965
15. V. N. Tsytovich, Theory of Turbulent Plasma, Consultants bureau, N.Y., 1977
16. A. A. Galeev and R. Z. Sagdeev, Nonlinear Plasma Theory, W. A. Benjamin, N.Y., 1969

17. L. D. Landau, J. Phys (USSR), 10,25(1946)

18. F. F. Chen, Introduction to Plasma Physics, Plenum Press, N.Y., 1974, Chapt. 7

19. S. M. Hamberger and J. Jancarik, Phys. of Fluids, 15,825(1972)

20. B. A. Demidov, et. al., Sov. Phys. Doklady, 12,467(1967)

21. A. Hirose, et. al., Phys. Rev. Lett., 28,1185(1972)

22. A. Hirose, et. al., Phys. Rev. Lett., 36,252(1976)

23. T. H. Dupree, Phys. Rev. Lett., 25,789(1970)

24. B. Coppi and E. Mazzucato, Phys. of Fluids, 14,134(1971)

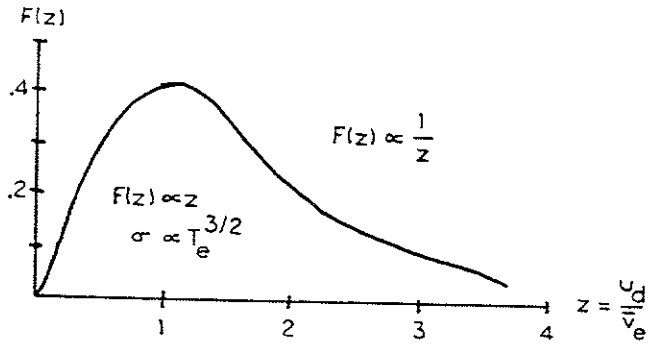

a. Dynamic friction force versus $z = u_d/v_e$

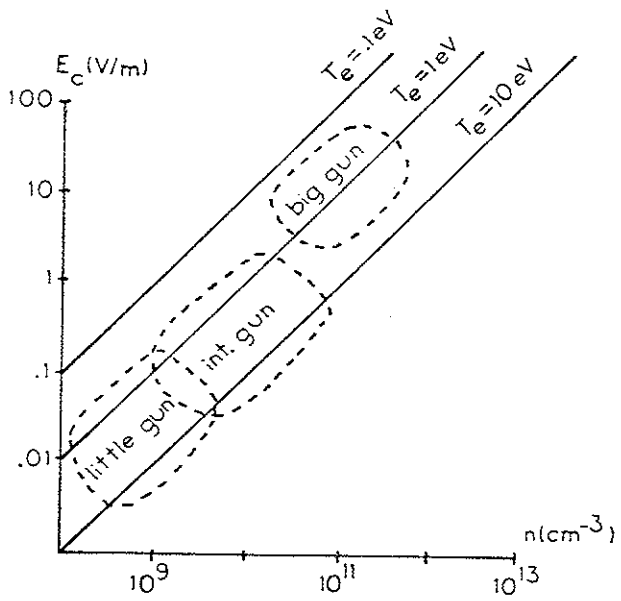

b. Critical electric field versus density and temperature

Figure VII-1

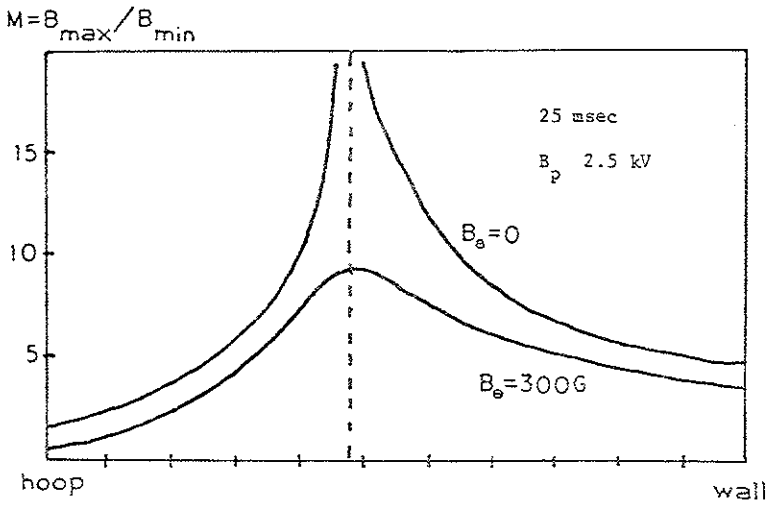

a. Mirror ratio versus position

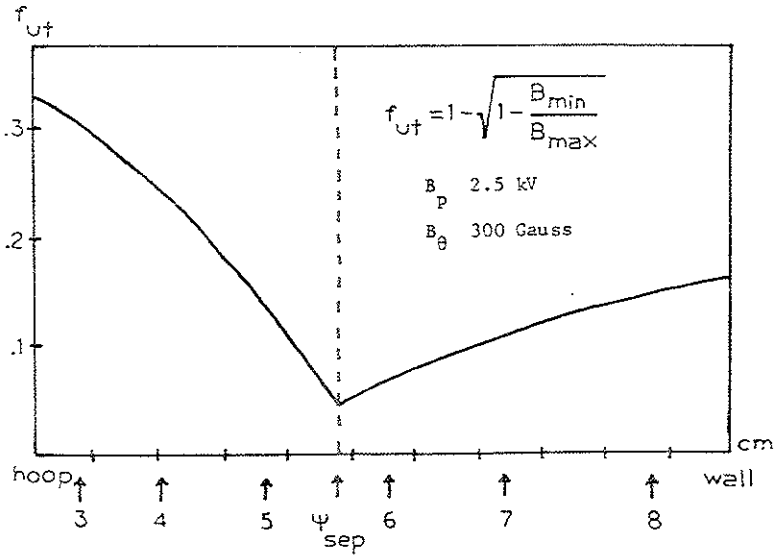

b. Circulating electron fraction versus position

Figure VII-2

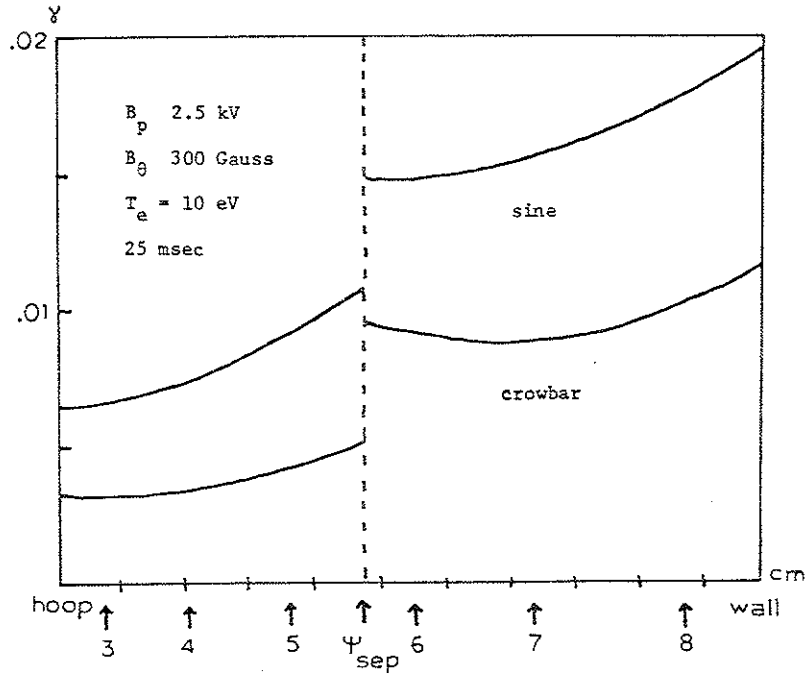

γ versus position in the bridge. $\gamma = \frac{qE_{\parallel}L_{bounce}}{kT_e}$

Figure VII-3

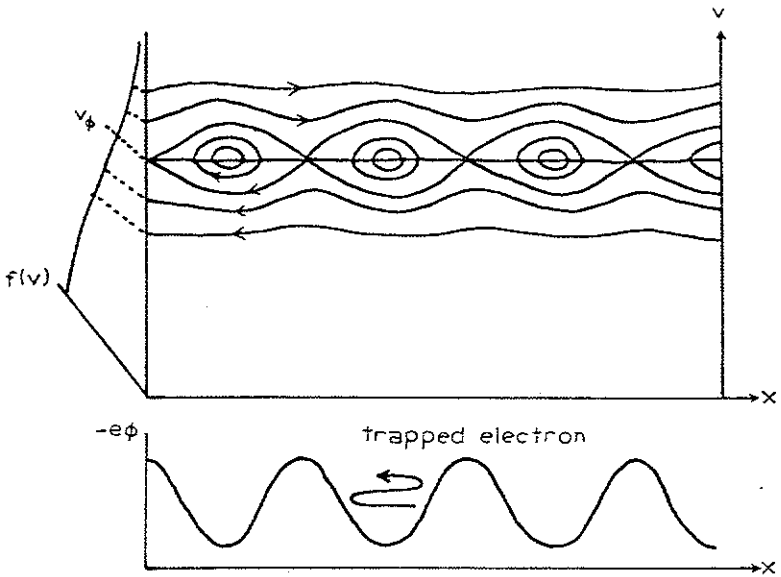

a. Phase space trajectories of electrons moving in a potential wave. Maxwellian velocity distribution.

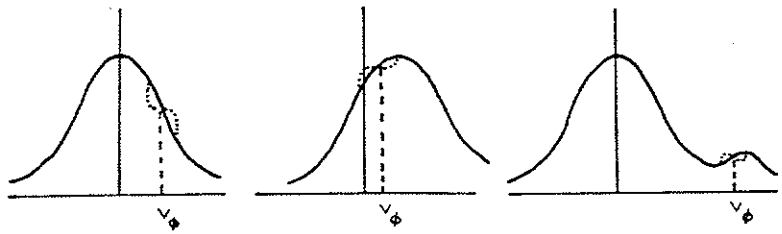

b. Maxwellian Landau damped

c. Drifting Maxwellian Landau growth

d. Bump on tail Landau growth

Figure VII-4

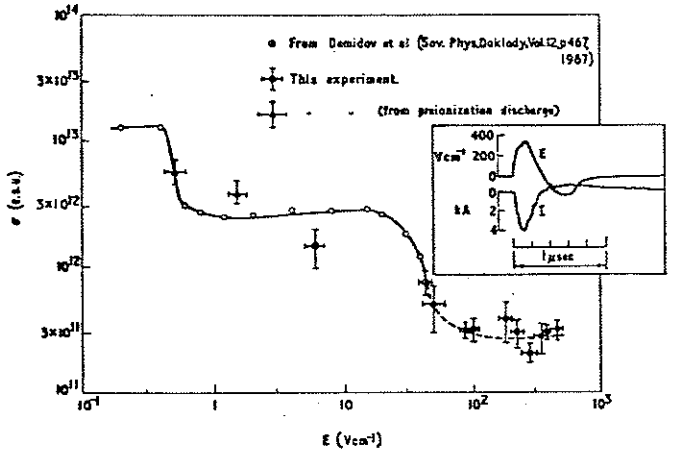

a. Conductivity versus electric field.

Hamberger & Friedman, Phys. Rev. Lett., 21,674(1968)

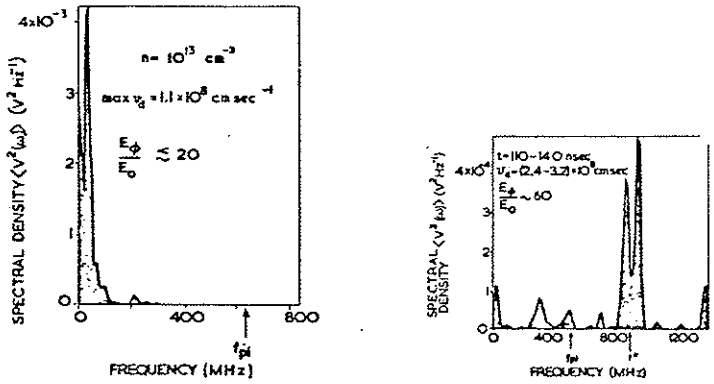

b. Ion acoustic turbulence spectrum

c. Two-stream spectrum

Figure VII-5

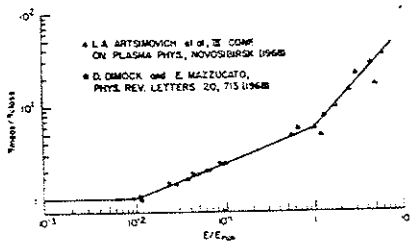

a. Resistivity versus electric field

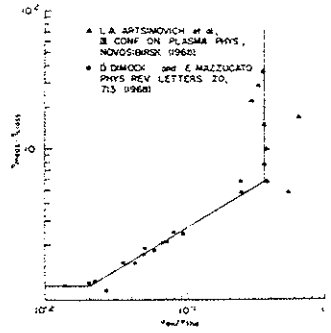

b. Resistivity versus electron drift velocity

Figure VII-6

Chapter VIII

Experimental Conductivity

The three plasma sources used in this research offered a wide range of plasma parameters. T_e varied from .2 eV in the big gun plasma to 10 eV in the little gun plasma. Density varied from 10^9 cm^{-3} in the little gun plasma to 10^{12} cm^{-3} in the big gun plasma. Using the conductivity theory of Chapter VII and the measured values of n_e and T_e allows us to predict the conductivity which we would expect each of the plasmas to exhibit. This is illustrated in Figure 1 for the big gun. ν_{ei} and ν_b were calculated from measured n_e and T_e and are plotted versus position in the octupole. The points with error bars are calculated values of $\nu_{ei} + \nu_{en}$ and show uncertainties due to measurement of T_e, n_e, and n_g. From Figure 1 it is seen that $\nu_{ei} > \nu_b$ throughout the octupole and we would therefore expect the big gun plasma to exhibit Spitzer conductivity.

Figure 2 shows a similar plot for the little gun plasma. ν_b is much greater than it was for the big gun plasma because of the higher electron temperature, $T_e \approx 10$ eV. The discontinuity in ν_b at the separatrix is due to the discontinuity in the length of the field line there ($\nu_b = v_e/L_m$). ν_{ei} is much lower than it was for the big gun plasma because of the lower plasma density. For the little gun parameters $\nu_b > \nu_{ei}$ throughout the octupole and we would therefore expect the little gun plasma to exhibit mirror conductivity.

Figure 3a shows the calculated ν_{ei}, ν_b, and $\nu_{\ell c}$ which occur at injection time for the intermediate gun plasma. The points with error

bars are calculated values of $\nu_{ei} + \nu_{en}$. It is seen that throughout most of the octupole volume the condition $\nu_{\ell c} > \nu_b > \nu_{ei}$ holds and therefore plateau resistivity should occur. Near the separatrix, however, the condition $\nu_{ei} > \nu_b$ is satisfied and Spitzer conductivity should be seen in this region. After about 10 msec the intermediate gun plasma density decays while T_e remains about the same and the conditions illustrated in Figure 3b occur. Once again $\nu_b > \nu_{ei}$ as in the little gun plasma and mirror conductivity should occur.

Using the above analysis allows us to predict ahead of time the plasma current density which will flow in response to an applied electric field once the source parameters n_e and T_e are known. Diagnostics with the required sensitivity to detect these currents can then be constructed.

The experimentally observed scaling of the plasma conductivity with the collisionality and also with T_e and density will be discussed in this chapter. Conductivity is defined as the ratio of the current density to the electric field.

$$\sigma = \frac{J}{E} \qquad \text{VIII-1}$$

where E is the induced electric field parallel to the magnetic field and J is the measured plasma current density parallel to the magnetic field.

The current density varies along the field line as can be seen in Figure 4, which shows a tube of magnetic flux circling the hoop. With a toroidal field added the tube is not closed but this will not affect the following argument. The continuity equation is

$$\oint \vec{J} \cdot d\vec{S} = -\frac{\partial}{\partial t}\int \rho dV = 0 \qquad \text{VIII-3}$$

$$J_1 S_1 = J_2 S_2 \qquad \text{VIII-4}$$

From this we see that the current density varies along the field line, being greatest where the flux tube narrows. Substituting $J = nev$ into eqn. 4 gives

$$n_1 e v_1 S_1 = n_2 e v_2 S_2 \qquad \text{VIII-5}$$

$$v_1 S_1 = v_2 S_2 \qquad \text{VIII-6}$$

Eqn. 6 results because the plasma density is constant along a field line ($n_1 = n_2$). Eqn. 6 resembles the equation of continuity for the flow of an incompressible fluid. This is illustrated in Figure 4b where the piston driving the fluid through the tube is equivalent to the average parallel electric field. Since J varies along a flux tube we must also substitute the average value of J into eqn. 1 in order to obtain the conductivity

$$\sigma = \frac{\langle J \rangle}{\langle E \rangle} \qquad \text{VIII-7}$$

$$\text{where} \quad \langle J \rangle = \frac{\oint \vec{J} \cdot d\vec{\ell}}{L} \qquad \text{VIII-8}$$

Several measurements of J along a field line are required to evaluate eqn. 8. This hardship can be avoided as follows.[1,2,3]

By conservation of magnetic flux we obtain

$$B_1 S_1 = B_2 S_2 \qquad \text{VIII-9}$$

Dividing eqn. 4 by eqn. 9 gives

$$\frac{J_1}{B_1} = \frac{J_2}{B_2} \qquad \text{VIII-10}$$

or J/B = constant along the flux tube. The conductivity can now be calculated as

$$\sigma = \frac{\langle J \rangle}{\langle E \rangle} = \frac{\oint \vec{J}/B \cdot d\vec{\ell}}{\oint \vec{E}/B \cdot d\vec{\ell}} = \frac{J}{B} \frac{\oint \vec{B} \cdot d\vec{\ell}}{\oint \vec{E} \cdot d\vec{\ell}} \qquad \text{VIII-11}$$

J and B are the current density and magnetic field at a point in space. $\oint \vec{B} \cdot d\vec{\ell}$ is the average B once around poloidally. $\oint \vec{E} \cdot d\vec{\ell}$ is the voltage generated once around poloidally.

$$V_{\parallel} = \oint \vec{E} \cdot d\vec{\ell} = \langle E \rangle L \qquad \text{VIII-12}$$

Thus the fact that J/B is constant along a flux tube allows us to determine σ from a local measurement of J.

A. Big gun conductivity

Figure 5a is a plot of big gun density versus time. Initial density on the separatrix is $n_e = 10^{12}$ cm^{-3}. With a He plasma the ions and electrons quickly cool to about .2 eV and then remain fairly constant. Due to the high collision frequency the temperatures rapidly equilibrate so that $T_e \approx T_i$. Current densities were measured with paddle probes and Rogowsky loops. The conductivity was determined by means of eqn. VIII-11. Conductivity versus position is plotted in Figure 5b. Also plotted is the Spitzer conductivity[4] for T_e = .2 eV. The data are seen to agree well with the Spitzer value except near the wall where the measured value of conductivity is low. The disagreement near the wall may be due to several factors:

(1) The plasma density is low near the wall and thus Spitzer conductivity may not be applicable. If the density is less than 10^{10} cm^{-3} the electric field (.1 - 1 V/m) becomes comparable to the Dreicer field.[5]

(2) Low frequency oscillations in the plasma density were observed outside ψ_{crit} in the region where the plasma was flute unstable. Interactions between the fluctuations and the drifting electrons could cause an enhanced resistivity.

Figure 6 illustrates the scaling of big gun conductivity versus density. The data are averaged measurements obtained on the bridge separatrix and midcylinder separatrix. The conductivity was measured while the density decayed from 10^{12} cm^{-3} to 10^{10} cm^{-3}. The conductivity

remained constant at about 100 $\Omega^{-1}m^{-1}$ which agrees with Spitzer conductivity for $T_e = .2$ eV. Spitzer conductivity has a small n_e dependence due to the $\ell n\ \Lambda$ term (Chapter VII, eqn. 3). For a three order of magnitude change in density, σ_S changes by a factor of 1.5 for $T_e = .2$ eV. Due to the large errors in measuring J for the big gun it was not possible to verify the Spitzer scaling of density.

B. Intermediate gun conductivity

Figure 7a is a plot of intermediate gun density on the separatrix versus time. Initial density is $n \simeq 2 \times 10^{11}$ cm^{-3} with $T_e \simeq 7$ eV and $T_i \simeq 25$ eV. Figure 8 shows oscilloscope traces of electron saturation current and paddle probe current for the intermediate density gun. For the first two msec the current density was $J \simeq 1200$ amp/m^2. The current density then falls abruptly to values on the order of 50 amp/m^2. The fluctuations in the electron current turn on at about the same time that the current drops. These fluctuations are discussed in Chapter X.

The conductivity versus density is plotted in Figure 7b. For the first 5 msec the conductivity agrees with Spitzer conductivity for $T_e \simeq 5$ eV. At later times the conductivity is 1 to 2 orders of magnitude lower than Spitzer. The conductivity varies linearly with density.

$$\sigma(\Omega^{-1}m^{-1}) \simeq 10^{-8}\ n(cm^{-3}) \qquad \text{VIII-15}$$

T_e remains fairly constant in the intermediate gun plasma; $T_e \simeq 7$ eV initially and $T_e \simeq 5$ eV 20 msec later. The scaling of conductivity versus T_e could not be determined due to the small range of T_e.

C. Little gun conductivity

Figure 9a illustrates little gun density versus position and time in the bridge region. Initial density on the separatrix was $n \simeq 5 \times 10^9$ cm^{-3} with $T_e \simeq 10$ eV and $T_i \simeq 30$ eV. Figure 9b shows parallel current density measured with a paddle probe. Both the plasma density and current density are seen to peak slightly inside the separatrix.

To determine conductivity scaling versus density the little gun plasma was fired into weaker magnetic field configurations. This does not change T_e, but because of lower trapping efficiency the initial density is lower. The density can be varied by more than an order of magnitude while keeping T_e constant. Figure 10 shows the scaling of conductivity versus density. Conductivity is seen to be proportional to density.

$$\sigma(\Omega^{-1}m^{-1}) \simeq 2 \times 10^{-8}\ n(cm^{-3}) \qquad \text{VIII-16}$$

The proportionality constant in eqn. 18 is approximately equal to that obtained for the intermediate gun plasma.

The scaling of the little gun conductivity with electron temperature was obtained by observing the change in conductivity as the electrons cool. The conductivity is written in the form

$$\sigma \propto nT_e^{\,a} \qquad \text{VIII-17}$$

The exponent in eqn. 19 can be obtained from

$$a = \ell n \frac{n I \sigma_o}{n_o T_o \sigma} \qquad \text{VIII-18}$$

where n_o, T_o, and σ_o are measured density, electron temperature, and conductivity at one time and n, T, and σ are the corresponding quantities at a later time when $T < T_o$. T_e varied from 10 eV at injection time to 5 eV 20 msec later. The value of the exponent was determined to be

$$a = -.5 \pm .2 \qquad \text{VIII-19}$$

The large uncertainty resulted from errors in measuring T_e, n, and σ.

D. Summary

Figure 11 is a summary of the data presented in this chapter. Conductivity is plotted versus density for the three guns. The conductivity of the big gun plasma agrees with Spitzer conductivity. The little gun and intermediate gun conductivity vary linearly with density according to

$$\sigma(\Omega^{-1}m^{-1}) \simeq 10^{-8}\, n(cm^{-3}) \Big/ \sqrt{T_e}\ (eV) \qquad \text{VIII-20}$$

Mirror conductivity is plotted for two values of T_e. As discussed in the introduction of this chapter the little gun plasma density and electron temperature are in the regime where mirror conductivity should be seen. Instead, the experimental conductivity is less than mirror conductivity and scales linearly with density. The intermediate gun plasma behaves similarly, showing the linear dependence on n_e late in time when mirror conductivity is expected.

The linear dependence on n_e corresponds to a constant mean free path in the conductivity formula.

$$\sigma = \frac{e^2 n_e}{m_e \nu_e} \lambda_{mfp} \qquad \text{VIII-21}$$

where λ_{mfp} is the effective distance between 90^0 scattering events. This is similar to the plateau conductivity discussed in Chapter VII.

$$\sigma = \frac{e^2 n_e}{m_e \nu_e} f_{ut} L_m \qquad \text{VIII-22}$$

where $\lambda_{mfp} = f_{ut} L_m$ is determined mainly by the magnetic field configuration. The data illustrated in Figure 11 were obtained on the separatrix and agreed with plateau conductivity scaling. Conductivity data were also obtained off the separatrix to see if plateau scaling held throughout the machine. Figure 12 is a plot of resistivity versus $m_e \nu_e / e^2 n_e$ on $\psi = 5$ with $f_{ut} L_m = .19$ m. Plateau resistivity should plot as a straight line with slope given by $\lambda_{eff} = f_{ut} L_m$. The experimental data points obtained from the little gun and intermediate gun plasmas agree well with the plateau resistivity. As an added check the value of $f_{ut} L_m$ was changed by decreasing B_θ and taking the data on $\psi = 7$ in the common flux region so that $f_{ut} L_m \simeq .3$ m. The results are illustrated in Figure 13 and again show agreement with plateau scaling.

A possible explanation of the constant mean free path may be the hoop supports. There are a total of 16 hoop supports in the big octupole which can act as obstacles to the plasma and thus impose an effective mean free path which is machine size dependent. The magnitude of this effect can be estimated as follows:

$$\lambda_{eff} = \frac{V}{A} = \frac{8.6\ m^3}{754\ cm^2} \approx 10^4\ cm \qquad \text{VIII-23}$$

where V is the machine volume and A is the total area of the 16 supports. This is three orders of magnitude greater than the λ_{mfp} observed experimentally. The hoop supports could be removed by a pneumatic mechanism for periods up to 20 msec while the hoops remained in position due to their inertia. The presence or absence of hoop supports in the plasma confinement region was found not to effect the resistivity scaling.

The probes used for measuring plasma density, temperature, and current also acted as obstacles to the plasma. Inserting probes into the midcylinder of the machine resulted in a decrease in plasma density and plasma current due to plasma loss to the probes but the resistivity scaling was not affected. From these measurements it appears that the constant mean free path observed in the collisionless regime is due entirely to the magnetic field structure and does not depend on obstacles in the plasma.

References for Chapter VIII

1. F. L. Hinton and C. Oberman, Nucl. Fus., 9,319(1969)
2. D. E. Lencioni, Univ. of Wisc. Ph.D. Thesis, PLP 276 (1969)
3. J. F. Etzweiler, Univ. of Wisc. Ph.D. Thesis, PLP 738 (1977)
4. L. Spitzer Jr., Physics of Fully Ionized Gases, 2nd ed., Wiley, N.Y., 1962
5. H. Dreicer, Phys. Rev., 115,238(1959)
6. K. Evans, PLP 503 (1973)

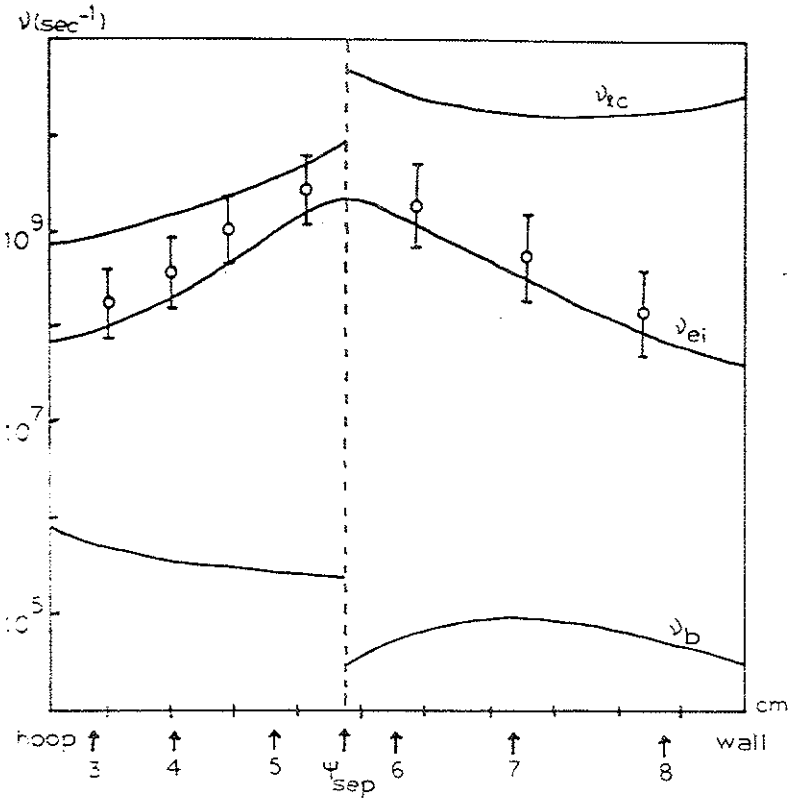

Figure VIII-1

Values of ν_{ei}, $\nu_{\ell c}$, and ν_b for big gun

$n_e \approx 10^{12}$ cm^{-3} $T_e \approx .2$ eV

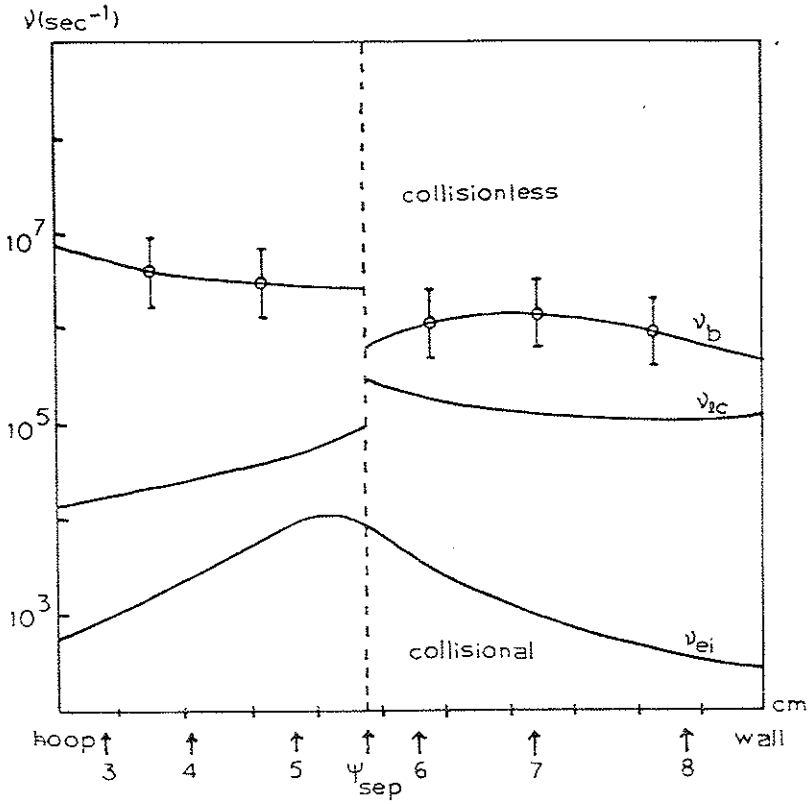

Figure VIII-2

Values of ν_{ei}, $\nu_{\ell c}$, and ν_b for little gun

$n_e \approx 5 \times 10^9$ cm^{-3} $T_e \approx 10$ eV

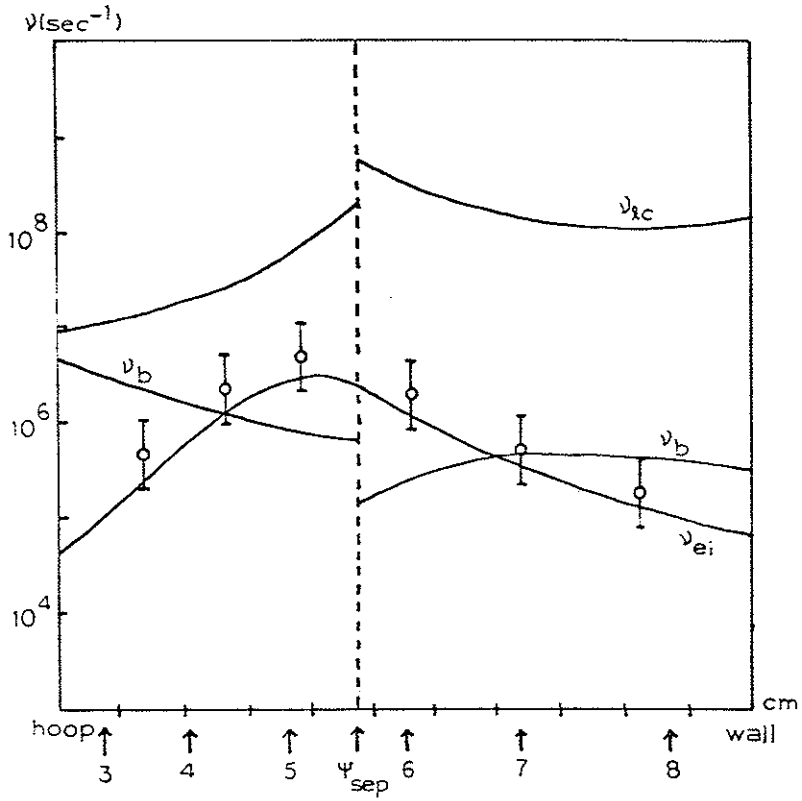

Figure VIII-3a

Values of ν_{ei}, $\nu_{\lambda c}$, and ν_b for intermediate gun at inj.

$n_e \approx 2 \times 10^{11}$ cm^{-3} $T_e \approx 7$ eV

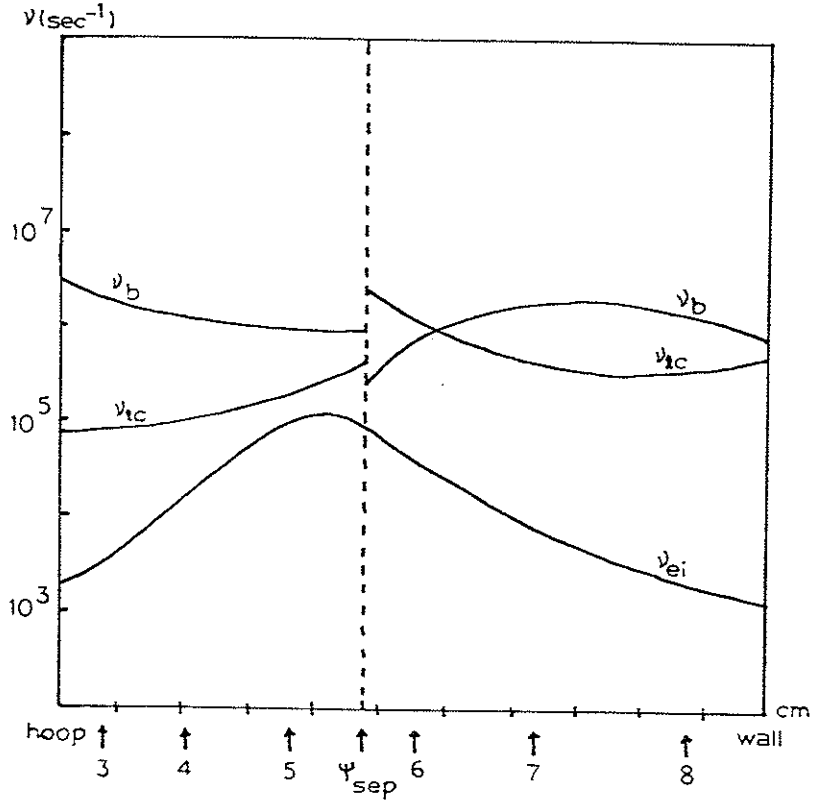

Figure VIII-3b

Values of ν_{ei}, $\nu_{\lambda c}$, and ν_b for intermediate gun 10 msec after inj.

$n_e \approx 5 \times 10^{10}$ cm^{-3} $T_e \approx 5$ eV

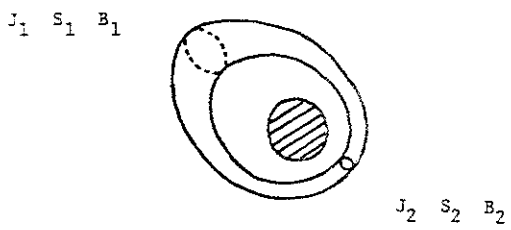

a. Flux tube circling the hoop

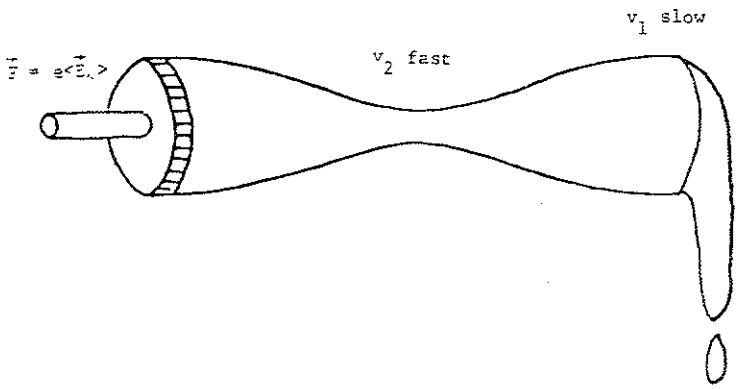

b. Fluid dynamics analogy

driving force = average parallel electric field

Figure VIII-4

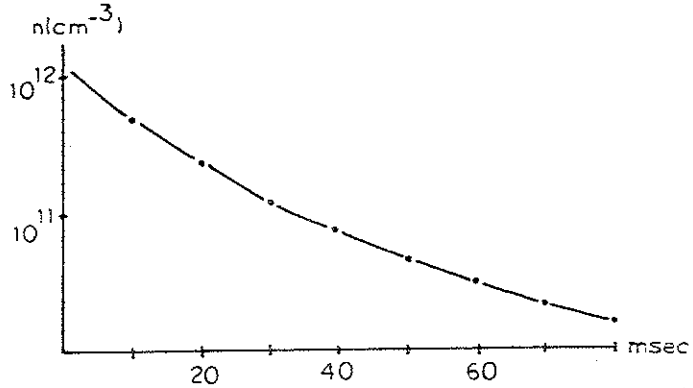

a. Density versus time on separatrix

Big gun, He plasma

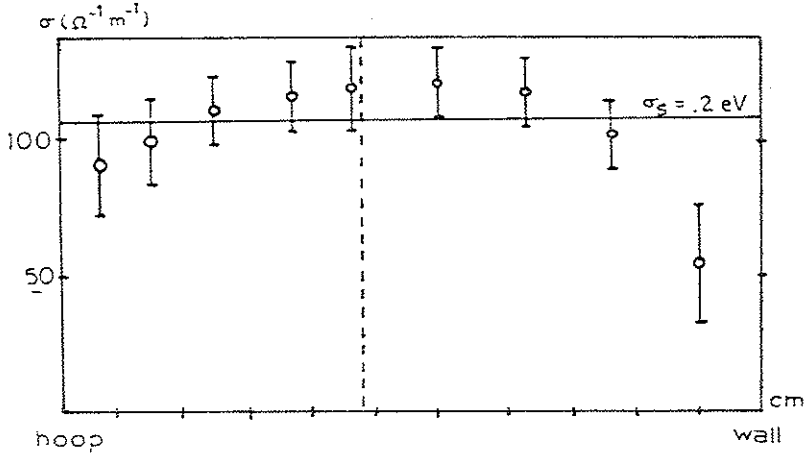

b. Big gun conductivity versus position in bridge

Figure VIII-5

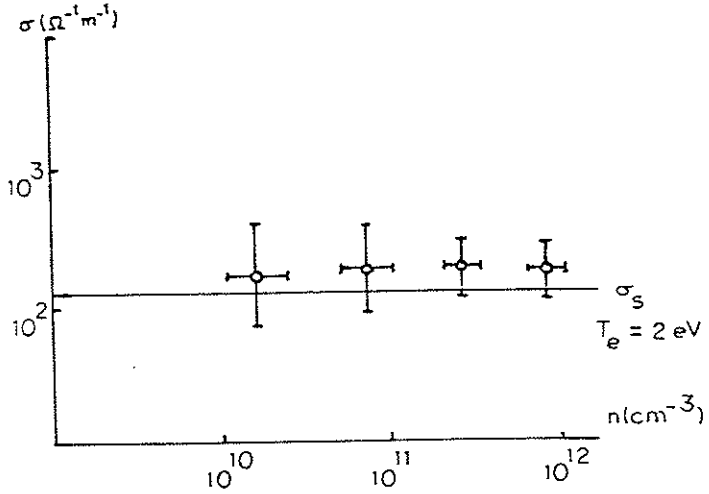

Figure VIII-6

Conductivity versus density, big gun, He plasma

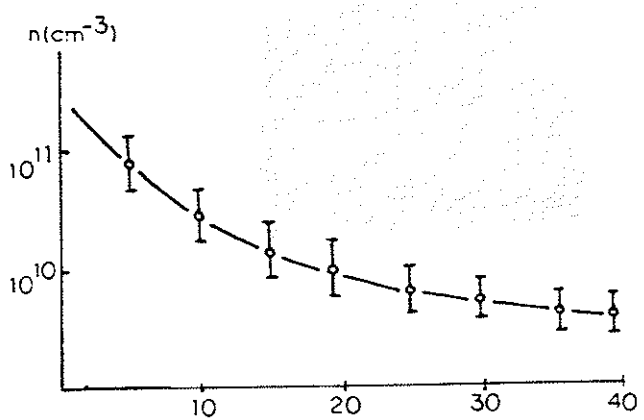

a. Intermediate gun density on separatrix

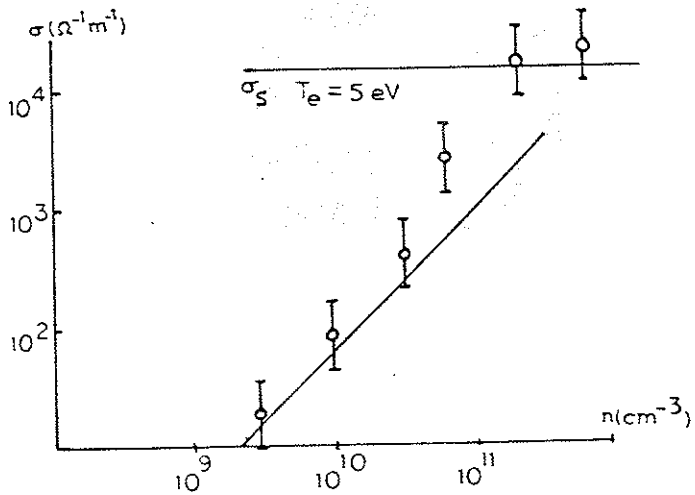

b. Intermediate gun conductivity versus density

Figure VIII-7

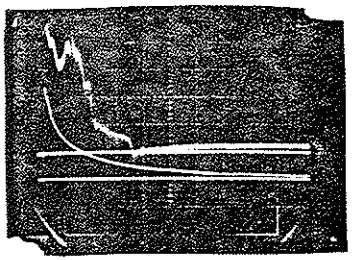

a. current density

300 Amp/m^2/div

2 msec/div

Midcylinder separatrix

gun inj. at 27 msec

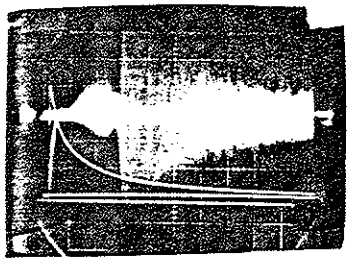

b. current fluctuations

2 msec/div

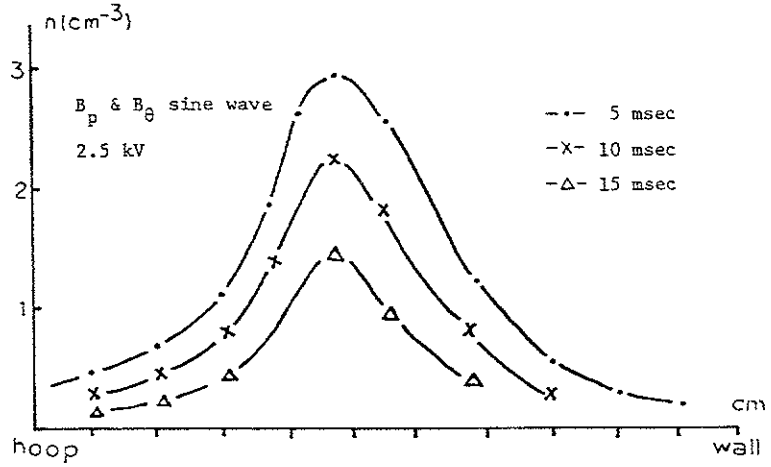

a. Little gun density versus position and time

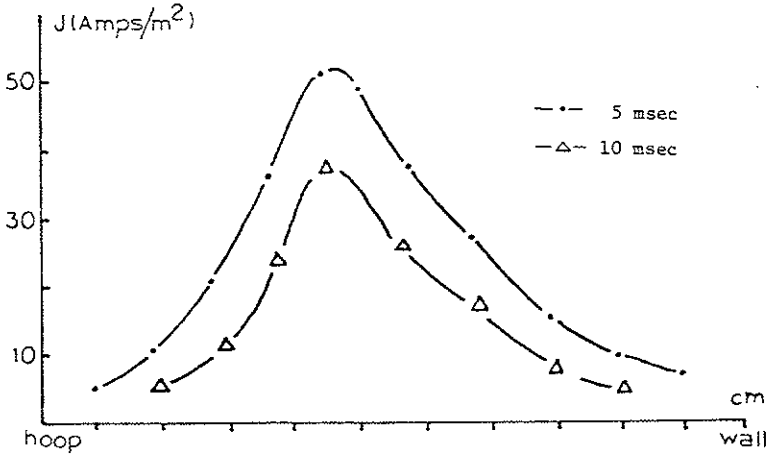

b. Little gun current density versus position and time

Figure VIII-9

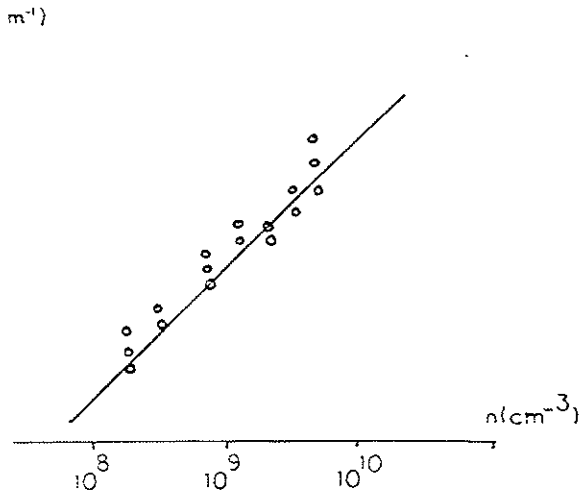

Figure VIII-10

.ittle gun conductivity versus density

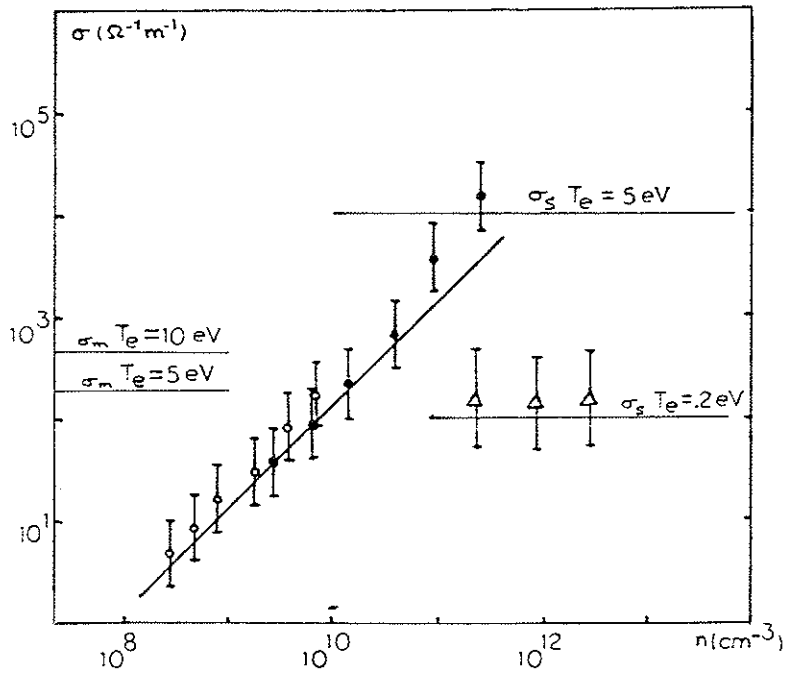

Conductivity versus density - bridge separatrix

-o- little gun, -•- intermediate gun, -Δ- big gun

Figure VIII-11

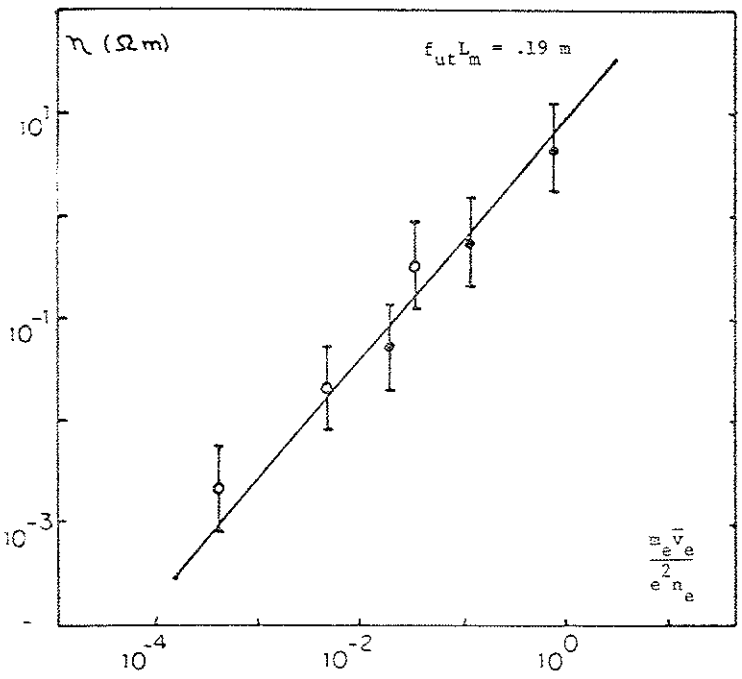

Resistivity versus $m_e\bar{\nu}_e/e^2n_e$

ψ = 5, B_p 2.5 kV, B_g = 300 G, 25 msec

Figure VIII-12

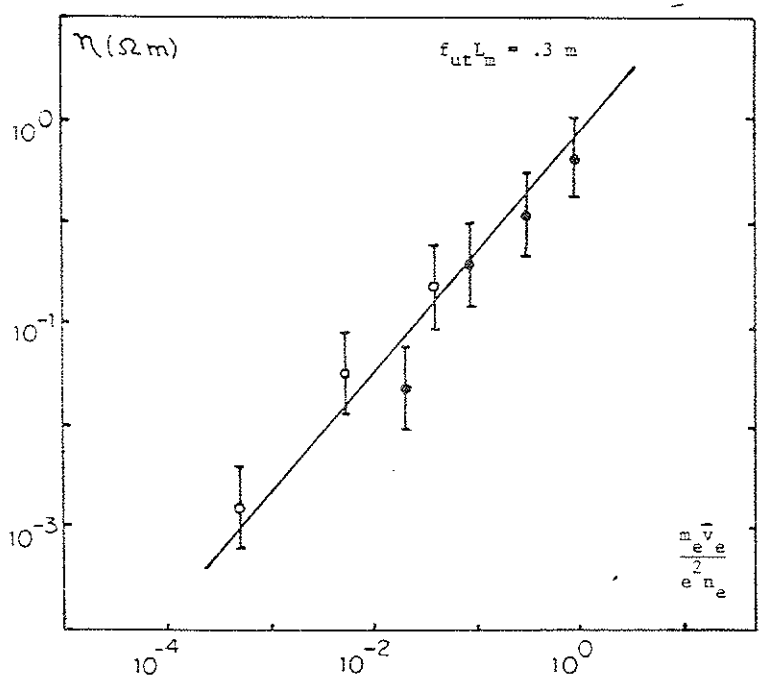

Resistivity versus $m_e\bar{\nu}_e/e^2n_e$

ψ = 7, B_p 2.5 kV, B_g = 100 G, 25 msec

Figure VIII-13

Chapter IX

Current Driven Instabilities

A. Ion acoustic instability[1-6]

An electric field applied to a plasma causes the electrons and ions to drift in opposite directions. The plasma can be represented by two drifting Maxwellians; one for the ions and one for the electrons. Since the electrons have a higher mobility than the ions it is reasonable to set the ion drift velocity equal to zero and consider only the electrons to be drifting.

The Vlasov equation and Poisson equation are

$$\frac{\partial f_j}{\partial t} + v\frac{\partial f_j}{\partial x} - \frac{e_j}{m_j}\frac{\partial \phi}{\partial x}\frac{\partial f_j}{\partial v} = 0 \qquad \text{IX-1}$$

$$\frac{\partial^2 \phi}{\partial x^2} = -4\pi \Sigma_j e_j \int_{-\infty}^{+\infty} f_j dv \qquad \text{IX-2}$$

The summation in eqn. 2 is over electrons and ions. Eqns. 1 and 2 are linearized by substituting $f_j(x,v,t) = f_{0j}(v) + f_{1j}(x,v,t)$ and neglecting second order terms. The following dispersion relation is obtained

$$1 = \frac{4\pi}{K^2}\sum_j \frac{e_j^2}{m_j}\left[P\int_{-\infty}^{+\infty}\frac{\partial f_{oj}/\partial u}{u-\omega/K}\,du + i\pi\frac{df_{oj}(\omega/K)}{du}\right] \qquad \text{IX-3}$$

P stands for the principal Cauchy integral. The electric field varies as $e^{i(K\cdot x - \omega t)}$ so that Im $\omega > 0$ causes instability. Drifting Maxwellians of the form below are used.

$$f_{0j}(u) = n_j\left(\frac{\beta_j}{\pi}\right)^{1/2} e^{-\beta_j(u-u_j)^2} \qquad \text{IX-4}$$

where $\beta_j = m_j/2kT_j$ IX-5

Substituting eqn. 4 into eqn. 3 gives the following dispersion relation

$$K^2 + \sum_j \frac{G(z_j)}{D_j^2} = 0 \qquad \text{IX-6}$$

where $D_j^2 = \frac{kT_j}{4\pi n_j e_j^2}$ IX-7

$$z_j = (\beta_j)^{1/2}\left[(\omega/K) - u_j\right] \qquad \text{IX-8}$$

$$G(z) = \frac{1}{\pi^{1/2}}\int_c \frac{qe^{-q^2}}{q-e}\,dq \qquad \text{IX-9}$$

The contour in eqn. 9 is from $-\infty$ to $+\infty$ below the poles. Expanding G(z) gives

$$G(z) \simeq -\frac{1}{2z^2} \qquad |z| \to \infty \qquad \text{IX-10}$$

For $T_i = 0$ eqn. 6 gives the dispersion relation for an ion acoustic wave.

$$0 = 1 - \frac{\omega_{pi}^2}{\omega^2} + \frac{\omega_{pi}^2}{K^2 c_s^2}Z\left[1 + i\frac{\pi m_e}{2m_i}\left(\frac{\omega}{|K|c_s} - \frac{u_d}{c_s}\cos\theta\right)\right] \qquad \text{IX-11}$$

where $c_s = (T_e/m_i)^{1/2}$ is the ion sound velocity, u_d is the electron drift velocity, and θ is the angle between u_d and $\vec{K}$. In the long wavelength limit, the phase velocity is equal to c_s and in the short wavelength

limit the frequency is equal to the ion plasma frequency. The dispersion relation is illustrated in Figure 1.

The second term on the right hand side of eqn. 3 corresponds to Landau damping[7,8] when $\partial f_{0j}/\partial u < 0$ and Landau growth when $\partial f_{0j}/\partial u > 0$. $\partial f_{0j}/\partial u$ is evaluated at the phase velocity $v_\phi = \omega/K$. Note that Landau damping can be caused by both electrons and ions.

Figure 1b illustrates the case where the wave grows due to electron Landau growth but damps due to ion Landau damping. For $T_i = T_e$ the wave is strongly damped. Growth of the wave can be encouraged if $T_e > T_i$ or by increasing the current $\vec{J} = ne\vec{u}_d$ flowing through the plasma. These two cases are illustrated in Figures 1c and d.

Figure 1c shows little ion Landau damping occurring when $T_i < T_e$. Although v_ϕ falls on a part of the ion distribution where $\partial f_i/\partial v < 0$, there are so few ions in this region that the damping is negligible. A similar effect is obtained by increasing the current flow and shifting the electron distribution further to the right.

The onset of the ion acoustic instability versus T_e/T_i and u_d/v_e is illustrated in Figure 2. In general, the electron drift velocity u_d must exceed the phase velocity $v_\phi = \omega/K$ enough to permit electron Landau growth to balance ion Landau damping.

If the electron distribution is shifted even further to the right the ion Landau damping becomes negligible and Im ω will be positive due to the large positive slope of f_e. This growing wave is just the two-stream instability which is seen to be an unstable ion oscillation.

Oblique ion acoustic waves:[9] When $T_e > T_i$ ion acoustic waves propagating at an angle to B can be shown to have critical drifts less than

the critical drifts of parallel ion acoustic waves. These oblique waves are low frequency $\omega < \Omega_i$ where Ω_i is the ion cyclotron frequency.

B. Two-stream instability[10]

Buneman compares the two-stream instability with the amplifying mechanism of a traveling wave tube.[11,12] The free energy source is the drift energy of the electrons. The electron beam traverses the traveling wave tube formed by the ions. The ions take the place of the helical slow wave structure and propagate a wave with velocity ω_{pi}/K. The fluctuating field $\vec{E}$ causes ion velocities $e\vec{E}/i\omega M$ and from the continuity equation, ion charge density fluctuations $(e^2n/\omega^2M)\vec{\nabla}\cdot\vec{E}$. The electrons are initially drifting with velocity u and the frequency with which they encounter the fluctuating field is doppler shifted by $\vec{K}\cdot\vec{u}$ where $\vec{K}$ is the wave vector. Electron velocities are $-eE/i(\omega - \vec{K}\cdot\vec{u})^2m$ and their charge density fluctuations are $[e^2n/(\omega - \vec{K}\cdot\vec{u})^2m]\vec{\nabla}\cdot\vec{E}$. A dispersion relation is obtained by substituting the charge density fluctuations into Poisson's equation.

$$1 = \frac{\omega_{pi}^2}{\omega^2} + \frac{\omega_{pe}^2}{(\omega - \vec{K}\cdot\vec{u})^2} \qquad \text{IX-12}$$

Maximum growth rate is given by

$$\gamma = \frac{\sqrt{3}}{2}\,\omega_{pe}\left(\frac{m}{2M}\right)^{1/3} = .0562\omega_{pe} \quad \text{for H} \qquad \text{IX-13}$$

The onset of the two-stream instability versus T_e/T_i and u_d/v_e is illustrated in Figure 2.

C. Ion cyclotron instability[6,13,14]

The ion acoustic instability only occurs in a plasma with $T_e > T_i$. For $T_i \approx T_e$ ion acoustic waves are strongly damped by the resonant ions and the growth of oscillations is possible only for $u_d > v_e$ (two-stream instability). However, in the presence of a magnetic field, ion cyclotron oscillations can be excited at smaller values of u_d. An ion cyclotron wave is just an ion wave traveling obliquely to the magnetic field in such a manner that its parallel phase velocity is not resonant with ions and therefore experiences little Landau damping.

Drummond and Rosenbluth derived the ion cyclotron dispersion relation for a plasma with $\beta = 8\pi P/B^2 < 1$. A homogeneous infinite collisionless plasma is assumed with ions and electrons having Maxwellian distributions and the electrons drifting due to an applied electric field. In addition to the acoustic restoring force the electrons and ions are also subject to a v x B Lorentz restoring force. Drummond and Rosenbluth obtain the dispersion relation

$$\omega = \Omega_i\{1 + \frac{T_e}{T_i} e^{-s} I_1(s) + i\sqrt{\pi} \frac{T_e}{T_i} e^{-s} I_1(s) \frac{K_z u - \Omega_i}{K_z v_e}\} \qquad \text{IX-14}$$

where $\Omega_i = eB/m_i$ is the ion cyclotron frequency, $s = K_\perp^2 \rho_i^2$, and $I_1(s)$ is the Bessel function of imaginary argument. Eqn. 14 is valid only for waves with small $K_\parallel$ since ion Landau damping can be neglected only for $K_\parallel < (\omega - \Omega_i)/3v_i$. From eqn. 14 it can be determined that $\omega - \Omega_i$ has a maximum value of $\approx .2\Omega_i T_e/T_i$ at $s \approx 1.5$ so that the condition on $K_\parallel$ becomes

$$K_\parallel < \frac{1}{15} \frac{T_e}{T_i} \frac{\Omega_i}{v_i} \qquad \text{IX-15}$$

The dispersion relation for the ion cyclotron instability is plotted in Figure 3. The onset of the ion cyclotron instability versus T_e/T_i and u_d/v_e is illustrated in Figure 2.

D. Drift waves[15-17]

The instabilities discussed above were derived for a homogeneous plasma. If a magnetized plasma has gradients of density or temperature, the particles have associated drifts. These drifts may excite instabilities which propagate across the field with a phase velocity on the order of the drift velocity. The free energy source for the instability is the drift energy of the plasma caused by the density or temperature gradient. If a current is flowing in the plasma due to an applied electric field the energy in the drifting electrons can also serve as a free source for the drift waves.

Drift cyclotron instability:[18,19] Both drift modes and cyclotron modes propagate predominantly perpendicular to the magnetic field and thus couple effectively. The characteristic frequency associated with a gradient in density is

$$\omega = \frac{K}{2\alpha\Omega} \frac{1}{n} \frac{dn}{dx} \qquad \text{IX-16}$$

where Ω is the cyclotron frequency, $\alpha = n/2kT$, and K is the wave vector. For frequencies near the ion cyclotron frequency $\omega \approx \Omega_i$ eqn. 16 gives

$$\frac{K}{2\alpha\Omega_i}\frac{n'}{n} \simeq \Omega_i \qquad \text{IX-17}$$

$$K\rho_i \simeq \frac{L}{\rho_i} \qquad \text{IX-18}$$

where ρ_i is the ion gyroradius and L is the scale length of the density gradient, $L = n/n'$. Since $L/\rho_i > 1$, eqn. 18 predicts modes with wavelengths smaller than the ion gyroradius.

Krall gives the dispersion relation

$$1 + K^2\lambda_{Di}^2 + \frac{K\,T_i n'}{\omega\, eBn} - \frac{1}{(\pi K^2\rho_i^2)^{1/2}}\,\frac{\omega - Kg/\Omega_i + KT_i n'/eBn}{\omega - \Omega_i - Kg/\Omega_i} \qquad \text{IX-19}$$

where $g = 3T_i/R_c m_i$ is a term due to the curved field lines. The growth rate is given by

$$\gamma = \Omega_i\left|\left(\frac{Kn'}{2\alpha\Omega_i} - \lambda\Omega_i - Kv_d\right)\frac{2\alpha\Omega_i}{K^2\rho_i(n' - 2/R_c)}\right|^{1/2} \qquad \text{IX-20}$$

R_c is the curvature of the field lines. It is seen that magnetic well curvature has a stabilizing effect, especially on the longer wavelengths. Another effect of the curved field lines is to shift the unstable frequency below Ω_i.

Ohkawa[20] has observed drift cyclotron instabilities in the DC Octupole. Frequencies observed were 200 - 500 kHz and were less than the ion cyclotron frequency. Fluctuation levels were low, 200 mV pp floating potential where n' was maximum and decreasing to zero on the separatrix.

Ohkawa notes that the high frequency of this mode makes it likely to

persist even when the steepness of the magnetic well has stabilized the interchange mode.

Yamada[21] has calculated the growth rate of the drift cyclotron instability when there is a drifting component of electrons due to an applied electric field. The threshold value of u is

$$\frac{u_d}{v_i} = 2\sqrt{2}\left(1 + \frac{T_i}{T_e}\frac{1}{A_n}\right)\left[\lambda n\left[\left(\frac{m_i}{m_e}\right)^{1/2}\left(\frac{T_e}{T_i}\right)^{3/2}A_n\right]\right]^{1/2} \qquad \text{IX-21}$$

where $A_n = I_n(K^2T_i/m_i\Omega_i)\exp(K^2T_i/m_i\Omega_i)$ IX-22

In this case the mode corresponds to the Drummond-Rosenbluth ion cyclotron wave but due to coupling with the drift mode it has a lower threshold for all values of T_e/T_i.

Oblique drift waves:[22-24] Oblique drift waves, $K\cdot B \neq 0$, in addition to depending on the gradient drifts, are also able to tap the thermal energy of the plasma by resonating with particles streaming along B. The resonant particles have velocities $\vec{v}\cdot\vec{B}/B$ similar to the phase velocity $\omega/K_\parallel$ of the wave. Rudakov and Sageev have shown that oblique drift waves transform into ion acoustic waves as the angle between the wave vector and the magnetic field decreases.

Kadomtsev[16] gives the dispersion equation for oblique drift waves as

$$\omega^2 - \omega\omega^* - K_\parallel^2 c_s^2 = 0 \qquad \text{IX-23}$$

where ω^* is the drift frequency and c_s is the ion acoustic velocity. ω versus K is plotted in Figure 4. Curve 1 refers to a wave propagating in the direction of the electron diamagnetic drift and is called the

accelerated wave. Curve 2 refers to the decelerated wave which propagates in the direction opposite to the electron diamagnetic drift. The two waves differ as $K_{\parallel} \to 0$; the frequency of the accelerated wave approaching ω^* while the decelerated wave frequency goes to zero. The transverse phase velocity of the accelerated wave for $K_{\parallel} \to 0$ is equal to the electron diamagnetic drift velocity. For $K_{\parallel} > K_{\perp}$ both waves become acoustic waves.

When $T_i = T_e$ ion acoustic waves are not expected to propagate because of the strong Landau damping. A drift wave, however, may propagate in an inhomogeneous plasma with $T_i = T_e$ with a frequency $\omega \simeq \omega^*$. The phase velocity of this wave parallel to the magnetic field may considerably exceed v_i and is therefore not subject to ion Landau damping. This effect is illustrated in Figure 4b. A pure ion acoustic wave with phase velocity $v_\phi = c_s$ is seen to experience electron Landau growth and ion Landau damping. The electron distribution function has a drift due to an applied electric field. The oblique drift wave is able to shift its parallel phase velocity far enough to the right so as to make the ion Landau damping term negligible. The oblique drift wave is thus able to experience the best of two worlds: it is able to tap energy from the ∇n drift and also from the electrons drifting parallel to B due to the applied electric field. The fastest growing wave will be the one that adjusts v_ϕ so as to minimize ion Landau damping.

References for Chapter IX

1. D. F. Smith and J. V. Hollweg, J. Plasma Phys., 17,105(1977)
2. E. A. Jackson, Phys. Fluids, 3,786(1960)
3. B. D. Fried and R. W. Gould, Phys. Fluids, 4,139(1961)
4. T. E. Stringer, Plasma Phys. 6,267(1964)
5. I. B. Bernstein and R. M. Kulsrud, Phys. Fluids, 3,937(1960)
6. J. M. Kindel and C. F. Kennel, J. Geophys. Res., 76,3055(1971)
7. L. Landau, J. Phys. (U.S.S.R.), 10,25(1946)
8. D. Bohm and E. P. Gross, Phys. Rev., 75,1864(1949)
9. D. G. Lominadze and K. N. Stepanov, Sov. Phys. Tech. Phys., 9,1408(k965)
10. O. Buneman, Phys. Rev., 115,503(1959)
11. J. R. Pierce, Proc. IRE, 37,980(1949)
12. J. R. Pierce, Traveling Wave Tubes, D. Van Nostrand Co., Inc., N.Y., 1950
13. W. E. Drummond and M. N. Rosenbluth, Phys. Fluids, 5,1507(1962)
14. N. D'Angelo, J. Geophys. Res., 73,6313(1968)
15. N. A. Krall, Advances in Plasma Physics, Simon & Thompson eds., Interscience Publishers, N.Y., 1968, Vol. 1
16. B. Kadomtsev, Plasma Turbulence, Academic Press, N.Y., 1965
17. A. B. Mikhailovskii, Theory of Plasma Instabilities, Consultants Bureau, N.Y., 1974, Vol. 2
18. N. A. Krall and M. N. Rosenbluth, Phys. Fluids, 5,1435(1962)
19. N. A. Krall and T. K. Fowler, Phys. Fluids, 10,1526(1967)

20. T. Ohkawa and M. Yoshikawa, Phys. Rev. Lett., 17,685(1966)

21. M. Yamada and H. W. Hendel, Princeton Plasma Physics Laboratory MATT-1249 (1977)

22. N. A. Krall and M. N. Rosenbluth, Phys. Fluids, 8,1488(1965)

23. F. C. Hoh, Phys. Fluids, 8,1741(1965)

24. L. I. Rudakov and R. Z. Sagdeev, Sov. Phys. Doklady, 6,415(1961)

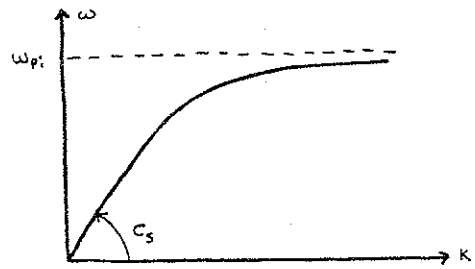

(a) Dispersion relation for ion acoustic waves

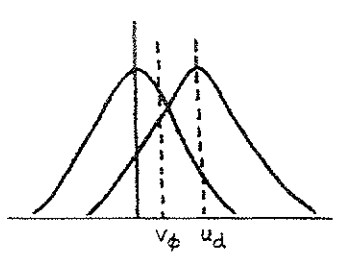

(b) $T_e = T_i$ damped wave

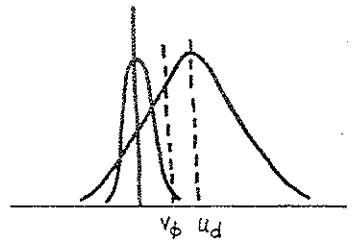

(c) $T_e > T_i$ growing wave

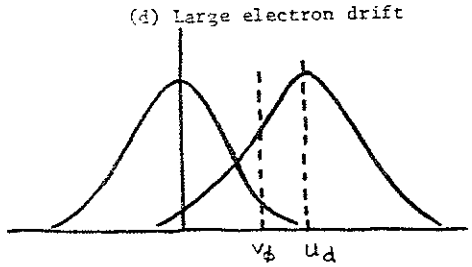

Figure IX-1

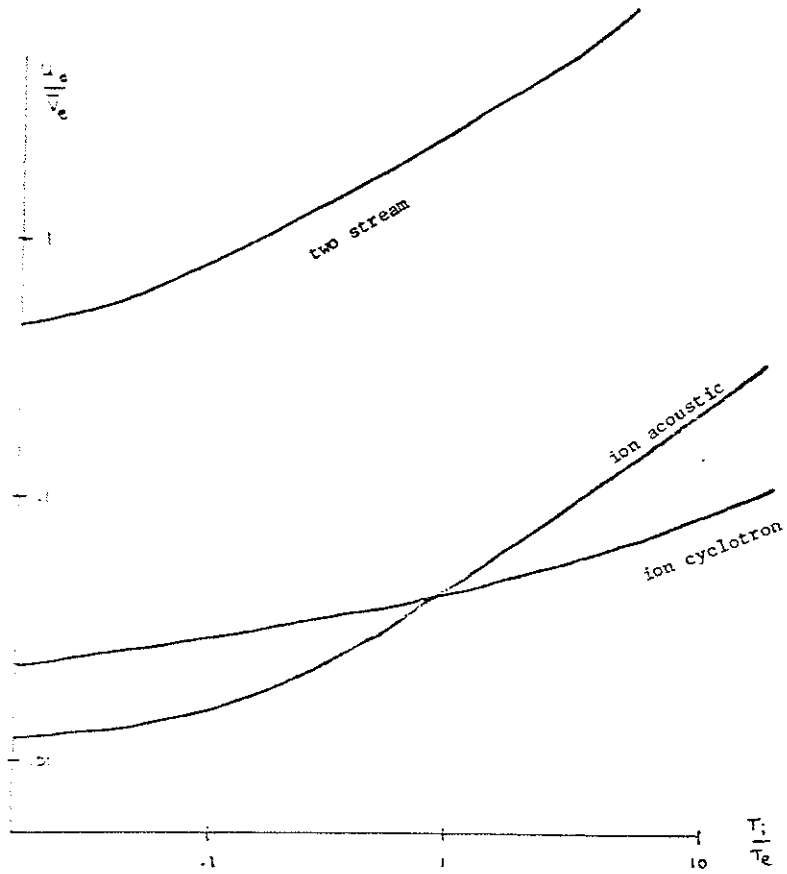

Instability threshold for current driven instabilities.

Modes are unstable above the lines.

J. M. Kindel and C. F. Kennel, J. Geophys. Res. 76,3055(1971)

Figure IX-2

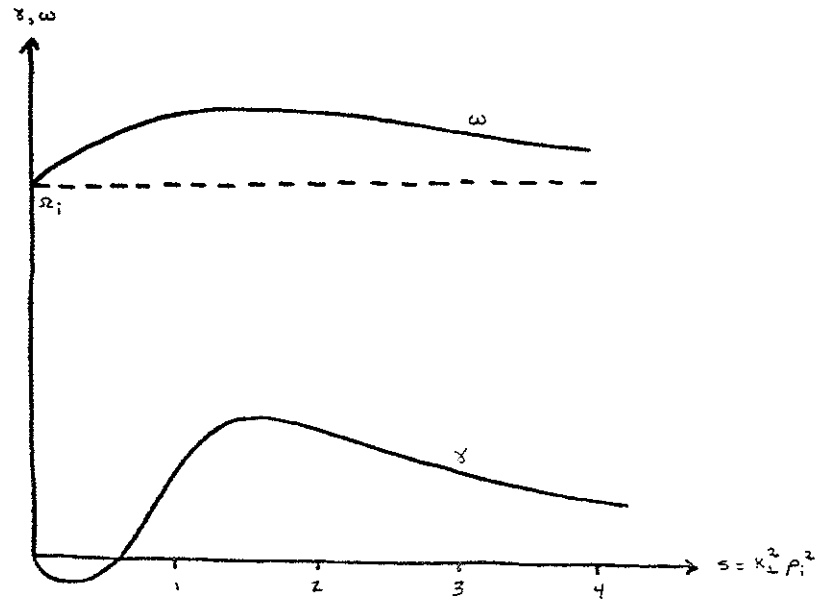

Frequency versus wavelength and growth rate versus wavelength for ion cyclotron instability.

Figure IX-3

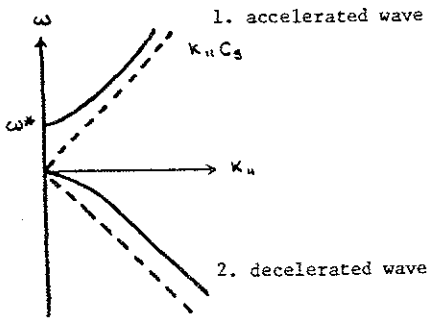

(a) Dispersion relation for oblique drift waves.

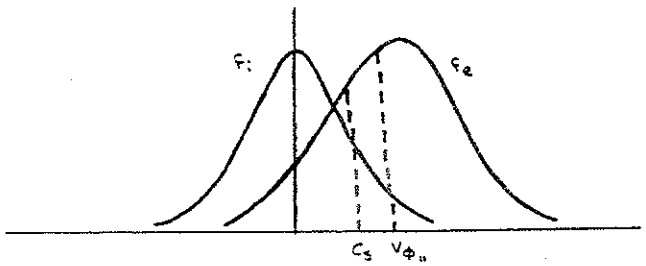

(b) Landau damping of an oblique drift wave.

Figure IX-4

Chapter X

Observed fluctuations

A. Little gun fluctuations

Density fluctuations were observed in the little gun plasma with frequencies near the ion cyclotron frequency and its harmonics. The fluctuations were observed in the electron saturation current, floating potential, and for high $E_\parallel$ ($\simeq$1 V/m) in the ion saturation current. Figure 1 contains oscilloscope traces of the fluctuations obtained from two probes oriented parallel and perpendicular to the B_θ field line on the midcylinder separatrix. The parallel and perpendicular wavelengths can be obtained from this data.[1] When the probe tips are oriented parallel to the field line as in Figure 1a little phase shift is seen between the two signals indicating a long parallel wavelength. Cross correlation of two digitized signals indicate a parallel wavelength greater than 1 meter which is in agreement with eqn. IX-15 evaluated at the little gun parameters.

$$K_\parallel < \frac{1}{15}\frac{T_e}{T_i}\frac{\Omega_i}{\nu_i} \qquad \text{X-1}$$

Figure 1b shows the case when the probe tips are oriented perpendicular to the magnetic field line. A phase shift of 70^0 is seen between the two signals. This indicates a perpendicular wavelength of $\lambda_\perp \simeq 4.5$ cm. With $B_\theta = 300$ Gauss the ion gyroradius is $\rho_i = 2.4$ cm. Thus the perpendicular wavelength is on the order of an ion gyroradius and $K_\perp \rho_i \simeq 1$. The phase velocity of the wave is given by

$$v_\phi = \frac{\omega}{K_\perp} = 1.6 \times 10^4 \text{ m/sec} \qquad \text{X-2}$$

Early in time (first 5 msec) the power spectrum of the oscillations is sharp and there is little power in the harmonics. ω and K can be determined from oscilloscope traces such as those in Figure 1. Later in time the power spectrum becomes broader and harmonics start to appear. The harmonics make it difficult to determine ω and K from examination of oscilloscope traces. In order to obtain a phase shift between two signals the signals must be digitized and cross correlated. This is illustrated in Figures 2 and 3.

Figure 2 shows data obtained 3 msec after gun injection. The two signals show a fundamental frequency and a small first harmonic. The cross correlation of the two signals is illustrated in Figure 2c. Only the fundamental appears in the cross correlation. The first harmonic in the two signals does not correlate. The cross power spectrum is illustrated in Figure 2d. Note the sharpness of the spectrum; most of the power occurs in a 100 kHz band. No harmonics are seen in the spectrum. The phase shift in Figure 2c again gives $K_\perp \rho_i \simeq 1$.

Figure 3 shows data obtained 15 msec after gun injection. Examination of the two signals shows a high harmonic content. The harmonics also show up in the cross correlation of the two signals indicating that the harmonics are also correlated. The cross power spectrum is illustrated in Figure 3d. Note how much broader this power spectrum is than the one in Figure 2d. Noticeable power also appears in the harmonics. The phase shift in Figure 3c is a combination of the phase shift in the fundamental and the phase shift in the harmonic. The cross correlation

of two signals preserves the shared frequency components.[2] Each of the shared frequencies, ω_j, will cause a shift at $\tau = 0$ equal to the phase difference between the two signals at that frequency.

The two phase differences can be obtained from the cross correlation function in the manner described in the appendix. The following equation is used

$$\phi_k = \text{Tan}^{-1} \frac{\text{Im } \tilde{C}(\omega_k)}{\text{Re } \tilde{C}(\omega_k)} \qquad \text{X-3}$$

where ϕ_k is the phase difference between the two signals with frequency ω_k and Re $\tilde{C}(\omega_k)$ and Im $\tilde{C}(\omega_k)$ are the real and imaginary parts of the Fourier transform of the cross correlation function.

From this data, ω and $K_\perp$ can be determined for the harmonics. For the first harmonic, $\omega \simeq 2\Omega_i$, it was determined that $\lambda_\perp \simeq 2$ cm, which is about half the wavelength of the fundamental. Thus the harmonic has approximately the same phase velocity as the fundamental.

Figures 4 and 5 show power spectra obtained at different values of magnetic field strength. Figure 4 shows the power spectra 3 msec after the little gun was fired. The spectra are sharp and have most of the power in the fundamental. Figure 4a shows an autocorrelation function obtained at $B_\theta = 300$ Gauss. The peak at $\tau = 0$ is due to broadband noise as described in the appendix. The noise quickly decorrelates to zero and only the correlated signal remains. The signal is seen to slowly decrease in amplitude corresponding to a decorrelation time of $T \simeq 25$ μsec which is determined by fitting an exponential $e^{-\tau/T}$ to the envelope of the oscillations.

Figure 5 shows power spectra obtained 15 msec after gun injection. The spectra are broad and show pronounced harmonics. Figure 5a shows an autocorrelation function obtained at B_θ = 300 Gauss. Note the large peak at τ = 0 which corresponds to broadband noise. The τ = 0 peak is a factor of 7 bigger than the correlated signal whereas the noise signal at 3 msec was only twice the correlated signal. The correlated signal at 15 msec also shows that the harmonics are correlated.

Kadomtsev[3] has calculated the power spectrum for a current driven ion cyclotron instability for the case $K_\perp \rho_i \simeq 1$ and $K_\parallel < T_e \Omega_i / 15 T_i v_i$. The long parallel wavelength allows the wave to grow without being subject to ion Landau damping. Those modes grow which satisfy

$$v_i < \frac{\Omega_i}{K_\parallel} < v_e \qquad \text{X-4}$$

Oscillations with a frequency slightly larger than Ω_i set up beats at frequencies close to zero and to $2\Omega_i$ (i.e. harmonics of Ω_i). The oscillations with very low frequency are able to transfer energy to the ions through nonlinear Landau damping and this process will lead to the limitation of the oscillation amplitude.

By considering nonlinear ion Landau damping and the formation of a plateau in the electron distribution function, Kadomtsev was able to derive the following estimate of the equilibrium spectral function.

$$dK_\perp \int I_k dK_\parallel = A \frac{T_e T_i}{e^2} \left(\frac{v_d^2}{v_e v_i^2 \Omega_e \tau_e} \right)^{1/2} \frac{dK_\perp}{K_\perp^2} \qquad \text{X-5}$$

where A ≃ 1, $\Omega_e = eB/m_e$, and τ_e is the electron collision time. Eqn. 5 gives I_k in terms of K. From the dispersion relation we can evaluate I in terms of ω

$$\omega = \Omega_i \left(1 + \frac{T_e}{T_i} e^{-s} I_1(s) + i\sqrt{\pi} \frac{T_e}{T_i} e^{-s} I_1(s) \frac{K_\parallel v_d - \Omega_i}{K_\parallel v_e}\right) \qquad \text{X-6}$$

where $s = K_\perp^2 \rho_i^2$ and $I_1(s)$ is the Bessel function of imaginary argument. There exist tables of $e^{-s} I_1(s)$.[4]

Figure 6 shows a comparison between the Kadomtsev spectrum and experimentally obtained spectra at 3 msec and 15 msec after gun injection. The experimental spectra are 5 shot averages. The Kadomtsev spectrum is seen to be narrower than the experimental spectrum. At 3 msec the Kadomtsev spectrum predicts a full width at half max of $\Delta\omega$ = 24 kHz whereas the observed spectrum has $\Delta\omega$ = 40 kHz. Similarly at 15 msec Kadomtsev predicts $\Delta\omega$ = 32 kHz while $\Delta\omega$ = 80 kHz is observed.

Although disagreeing in magnitude, the Kadomtsev spectrum does predict the general trend of the spectrum broadening later in time. This is a result of the T_e/T_i term in eqn. 6. The range in K space where unstable oscillations occur increases as T_e/T_i increases. As ΔK increases so does $\Delta\omega$.

Kadomtsev considered only nonlinear ion Landau damping and plateau formation in the derivation of eqn. 5. Tsytovich[5] has shown that nonlinear wave-wave interactions can also lead to spectrum broadening. Tsytovich refers to this process as plasmon-plasmon interaction and the spectrum broadening is called correlation broadening. Correlation

broadening leads to a spectrum of the form

$$I_k \propto \frac{1}{(\omega - \omega_k)^2 + \gamma_k^2} \qquad \text{X-7}$$

$$\gamma_k < \omega \qquad \text{X-8}$$

i.e., the peak is shifted and broadened. Correlation broadening has been applied to Langmuir turbulence and ion acoustic turbulence but there exists a paucity of theory on correlation broadening applied to the ion cyclotron instability.

B. Intermediate gun fluctuations

Figure 7 shows oscilloscope traces of electron saturation current and paddle probe current for the intermediate density gun. Fluctuations in the electron current are observed to turn on 2 msec after gun injection when $v_d \simeq .05\ v_e \simeq 5\ v_i$. The fluctuations separate into two regions which will be called early and late.

The early fluctuations occur from 2 msec to 6 msec and were identified as an ion cyclotron mode similar to the fluctuations observed in the little gun plasma. From figure IX-2 it is seen that the ion cyclotron mode is driven unstable when $v_d > .03\ v_e$ and $T_i > T_e$. This condition is satisfied in both the little gun plasma and the intermediate gun plasma.

Power spectra for the oscillations are illustrated in Figure 8. 3 msec after gun injection the power spectrum shows a narrow peak near the ion cyclotron frequency. This mode was found to propagate perpendicular to the magnetic field with $K_\perp \rho_i \simeq 1$ and $\lambda_\parallel > 1$ meter in a similar

manner to the mode observed in the little gun plasma. The long parallel wavelength allows the mode to satisfy the condition

$$v_i < \frac{\omega}{K_\parallel} < v_e \qquad \text{X-9}$$

This allows the fluctuations to gain energy by resonance with the drifting electrons while avoiding Landau damping from the ions.

Figure 8b shows the power spectrum 5 msec after gun injection. The spectrum is seen to be about twice as broad as that in Figure 8a. This is due to the increasing value of T_e/T_i as was discussed previously in explaining the broadening of the little gun spectra. Figure 8c shows the power spectrum 7 msec after gun injection. The spectrum has spread considerably and a harmonic has appeared. A large percentage of the power occurs at frequencies below f_{ci}. This behavior was not noticed in the little gun plasma.

Figure 8d shows the power spectrum 10 msec after gun injection (i.e. during the late fluctuation region). Fluctuations occur from 100 kHz to 1 MHz. The fluctuations at and above f_{ci} were determined by cross correlation methods to be ion cyclotron modes. When $T_e > T_i$ the fundamental and harmonic peaks become so broad that they overlap each other and form a continuous spectrum.

The low frequency oscillations ($< f_{ci}$) did not conform to the ion cyclotron dispersion relation. $K_\perp$ and ω were found to vary so that the phase velocity remained constant at $v_\phi \simeq 10^4$ m/sec. This is close to the diamagnetic drift velocity for the intermediate gun plasma.

$$v_d = \frac{kT_e}{eB}\frac{\nabla n}{n} \approx 1 \times 10^4 \text{ m/sec for B = 300 Gauss} \qquad \text{X-10}$$

$$\approx 4 \times 10^4 \text{ m/sec for B = 1 kGauss}$$

$\lambda_\perp$ was found to vary from 1 cm to 50 cm. The mode was determined to propagate in the elctron diamagnetic drift direction. Schmidt[5] has observed a similar mode in the quadrupole when the plasma was subjected to a large $E_\parallel$. Because of the $\omega/K \approx v_\phi \approx$ constant dispersion relation he referred to the mode as an ion acoustic - drift mode.

Both drift waves and ion cyclotron waves propagate predominantly perpendicular to the magnetic field and thus can couple effectively. It is hard to tell in Figure 8 where the ion cyclotron mode ends and where the ion acoustic - drift mode begins. If one uses $K_\perp \rho_i \approx 1$ for the ion cyclotron mode then $v_\phi \approx v_d$ when f < 300 kHz. The broadening of the ion cyclotron power spectrum can generate frequencies of this order and thus the ion cyclotron mode and the drift mode are identical.

Although it can be argued in this manner that the late oscillations are generated by the broadening of the ion cyclotron peaks into a continuous spectrum the early and late oscillations will be considered as two different modes. There are two reasons for proceeding in this manner.

First, Figure 7 shows that the amplitudes of the two modes differ. $\delta n/n$ is a factor of two greater for the late oscillations than it is for the early oscillations. The late oscillations have an additional free energy source. $\lambda_\perp$ is adjusted so that the mode can tap energy from the

diamagnetic drift. $\lambda_\parallel$ was found to be large so that $\omega/K_\parallel$ can still resonate with the drifting electrons due to $E_\parallel$.

Second, the ion temperature decays rapidly in the intermediate gun plasma so that $T_e > T_i$ when the late oscillations were observed. Figure IX-2 shows that ion acoustic oscillations are able to be excited if v_d is high enough. As explained in section IX-D an ion acoustic mode in an inhomogeneous plasma can propagate obliquely to the magnetic field so that $\lambda_\perp$ enables the mode to interact with the diamagnetic drift while $\lambda_\parallel$ is such that $\omega/K_\parallel = c_s$. Unfortunately $\lambda_\parallel$ was so large in this experiment that an accurate value for $K_\parallel$ could not be determined (i.e., it appeared as though $K_\parallel = 0$).

Figure 9 illustrates energy balance in the intermediate gun plasma. The curve labelled v_{din} is the predicted value of the parallel electron drift velocity if all of the $E_\parallel \cdot J_\parallel$ energy went into the drifting electrons. v_{din} is determined as follows

$$\int_0^\tau E_\parallel J_\parallel dt = n\tfrac{1}{2}mv_{din}^2 \qquad \text{X-11}$$

$\int_0^\tau E_\parallel J_\parallel dt$ is the total amount of energy per unit volume that is deposited in the plasma up to a time $t = \tau$ msec. $J_\parallel$ versus time and position was obtained from paddle probe measurements. $E_\parallel$ versus time and position was calculated from the changing B fields as described in Chapter V. The average v_{din} over the octupole cross section is plotted in Figure 9. Notice that v_{din} initially rises very rapidly due to the large $J_\parallel$ at early times. At 5 msec $J_\parallel$ drops to a low value and v_{din} increases slowly afterwards. The measured value of v_d averaged over the octupole

cross section is also plotted. v_d and v_{din} are in agreement for the first 2 msec but then v_d falls below v_{din} when the fluctuations occur.

The energy in the fluctuations was determined as follows. It is known that $\hat{n}/n = e\hat{\phi}/kT_e$ for drift waves. Fluctuations in the floating potential of $\hat{\phi} = .1$ Volt were observed in the late oscillations which agree with $\hat{n}/n = .03$ for $T_e = 10$ eV. Thus the energy in the density fluctuations is equal to the energy in the potential fluctuations (i.e. kinetic energy = potential energy). The same relation was assumed to hold for the ion cyclotron oscillations. The total fluctuation energy averaged over the octupole cross section is plotted in Figure 9.

The sum of the drift energy and the fluctuation energy is plotted as the dotted line in Figure 9. The drift energy and fluctuation energy account for only 60% of the input energy. The remaining 40% can be accounted for as follows. Both ion acoustic and ion cyclotron oscillations cause a plateau to form in the electron distribution. This was discussed in section VIII-H. The parallel phase velocity of the instability resonates with the drifting electrons. Drift energy is transferred to the instability and also to the random electron velocity thereby causing a high energy tail.

The electron velocity distribution was examined with the E x B energy analyzer. The analyzer didn't have enough resolution to see the plateau in the distribution but a high energy tail was observed. This is shown in Figure 10. 2 msec after gun injection the electron velocity distribution was observed to be Maxwellian with $T_e = 9$ eV. 15 msec after injection the bulk electron temperature was observed to be $T_e = 6$ eV

with a high energy tail of $T_e = 20$ eV. The energy in the tail can be obtained by subtracting a 6 eV Maxwellian from Figure 9. The density of the 6 eV Maxwellian is

$$10^{10}\ \text{cm}^{-3} = n = \int f(v)dv \qquad \text{X-12}$$

The total energy in the remaining 20 eV tail was determined to be

$$E_{tail} = 10^{-4}\ \text{Joule/m}^3 \qquad \text{X-13}$$

This value was determined on the midcylinder separatrix and was arbitrarily taken to represent the average over the octupole cross section. It was difficult to determine E_{tail} from the distribution function at earlier times so E_{tail} was assumed to be constant in time at the value given in eqn. 13.

The dotted line in Figure 9 is the sum of the energy in v_d, the fluctuations, and the high energy electron tail. This sum accounts for about 80% of the input energy. The remaining 20% can be accounted for by various processes such as ionization of background neutrals, excitation radiation, and particle losses to hoops, walls, and supports.[7] Ions are heated due to ion Landau damping. Skimmer probes do not offer enough resolution to measure this heating. Also, Figure 9 does not account for the energy in the fluctuations which came from the diamagnetic drift.

References for Chapter X

1. S. Yoshikawa, Methods of Experimental Physics, Griem & Lovberg, eds. Academic Press, N.Y., 1970, Vol. 9A, Chapt. 8
2. C. J. Armentrout, Univ. of Wisc. Ph.D. Thesis (Physics), PLP 794
3. B. B. Kadomtsev, Plasma Turbulence, Academic press, N.Y., 1965
4. M. Abramowitz and I. A. Stegun, eds., Handbook of Mathematical Functions, Nat. Bureau of Standards, 1972
5. V. N. Tsytovich, Theory of Turbulent Plasma, Consultants Bureau, N. Y., 1977
6. G. L. Schmidt, Univ. of Wisc. Ph.D. Thesis (Physics), PLP 633 (1975)
7. W. C. Guss, Univ. of Wisc. Ph.D. Thesis (Physics), PLP 689 (1975)

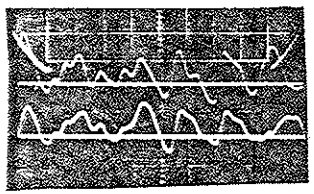

2 μsec/cm

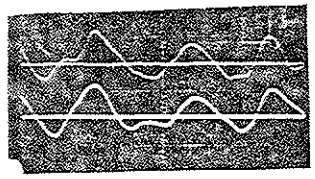

1 μsec/cm

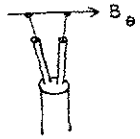

Tips parallel to B_θ on midcylinder sep.

B_θ = 300 Gauss, B_p 2.5 kV

tip separation = 1.1 cm

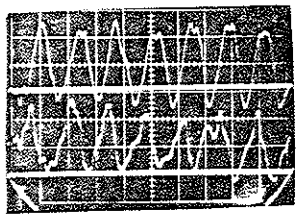

2 μsec/cm

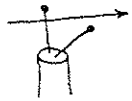

Tips perpendicular to B_θ

tip separation = .85 cm

Figure 1

little gun plasma fluctuations

5 msec after inj.

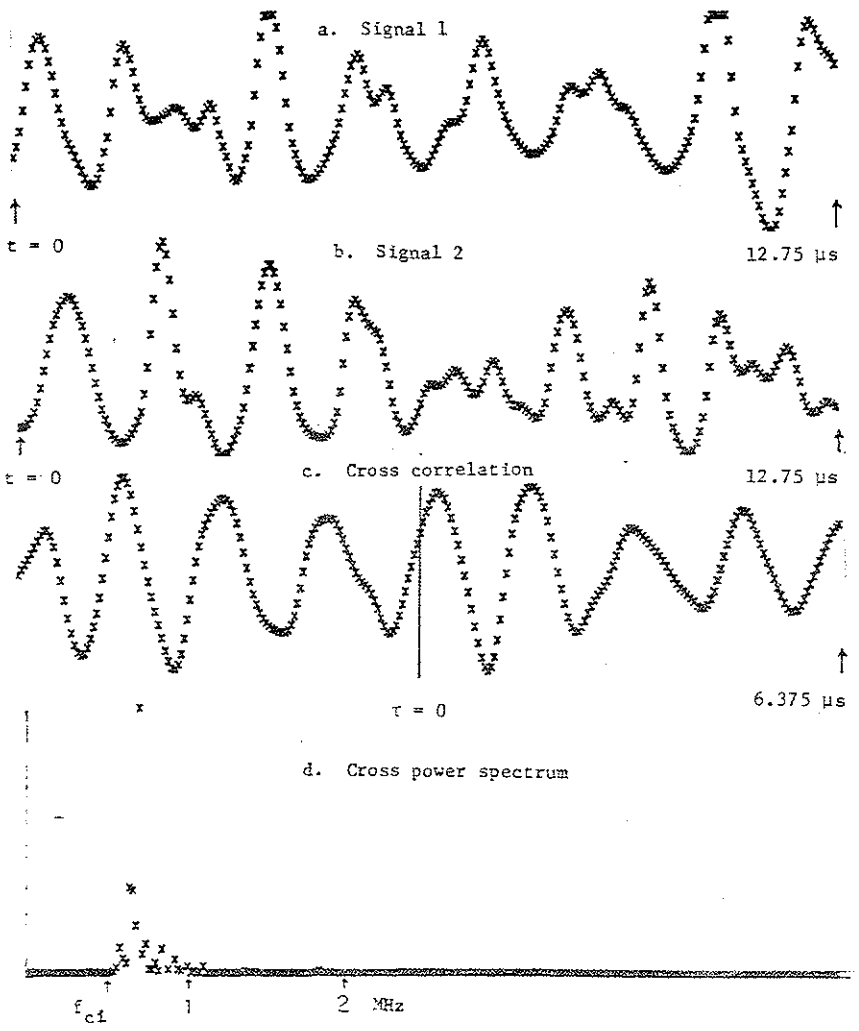

Figure 2

Little gun plasma, B_p 2.5 kV, B_g = 300 Gauss, ⊥ wavelength measured

Signals obtained 3 msec after gun on midcylinder sep.

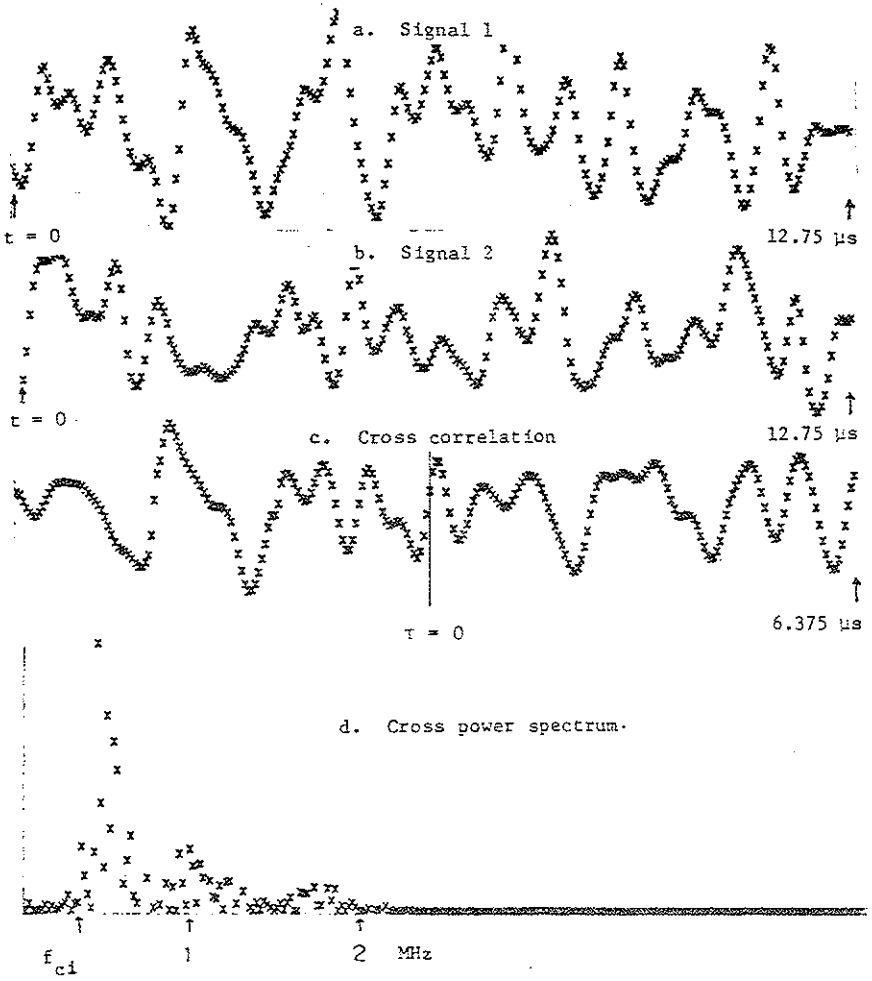

Figure 3

Little gun plasma, B_p 2.5 kV, B_g = 200 Gauss, ∥ wavelength measured

Signals obtained 15 msec after gun on midcylinder sep.

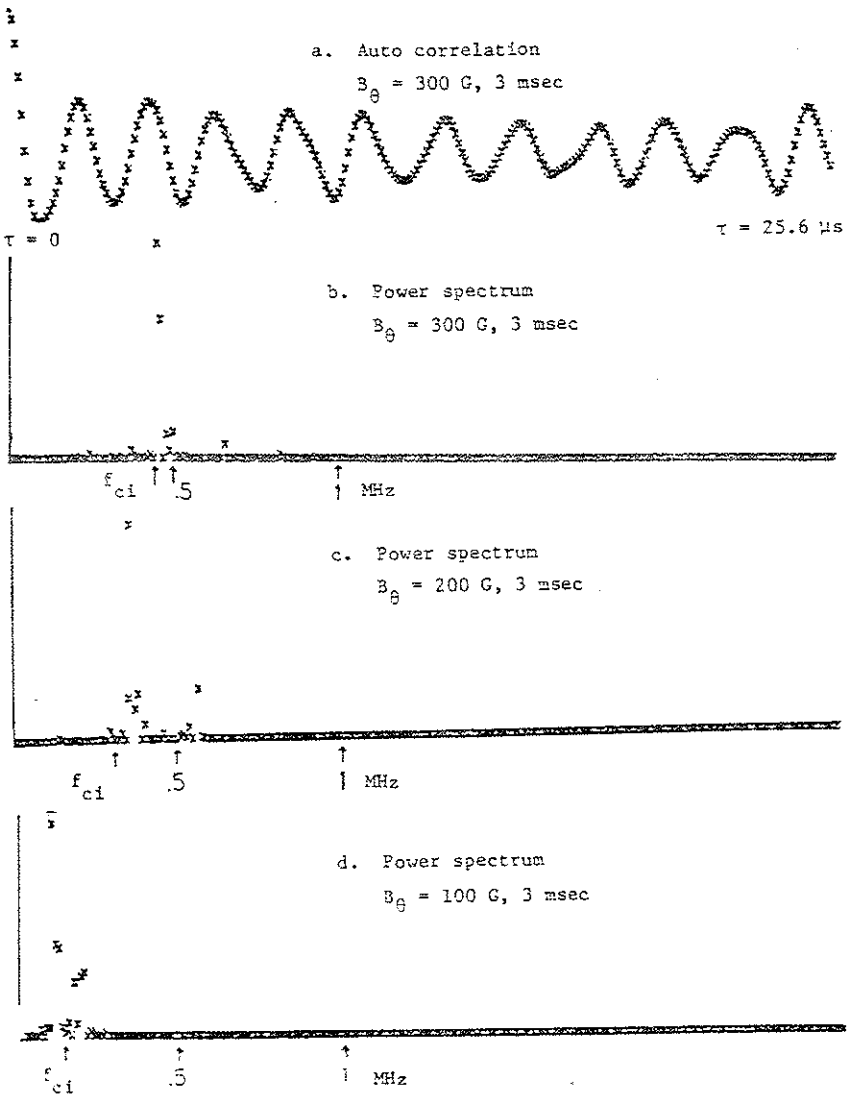

Figure 4

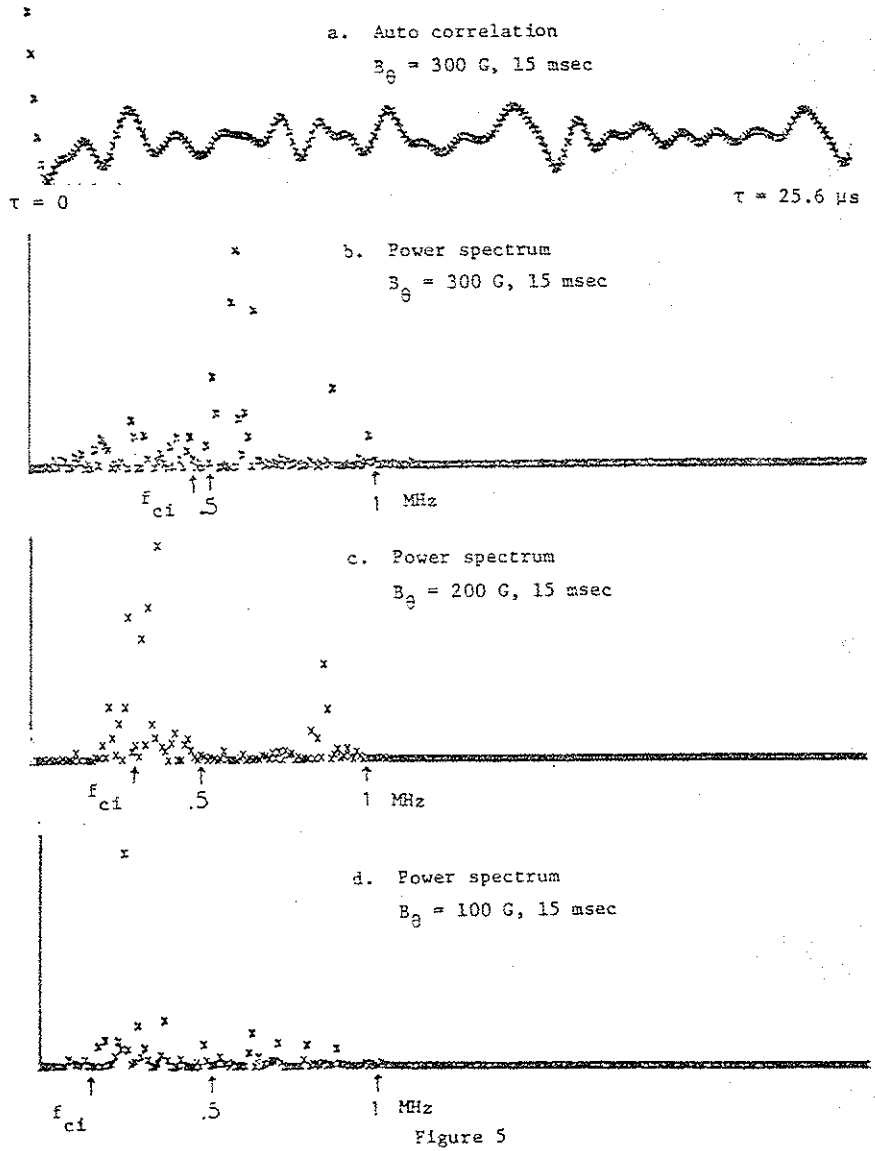

Figure 5

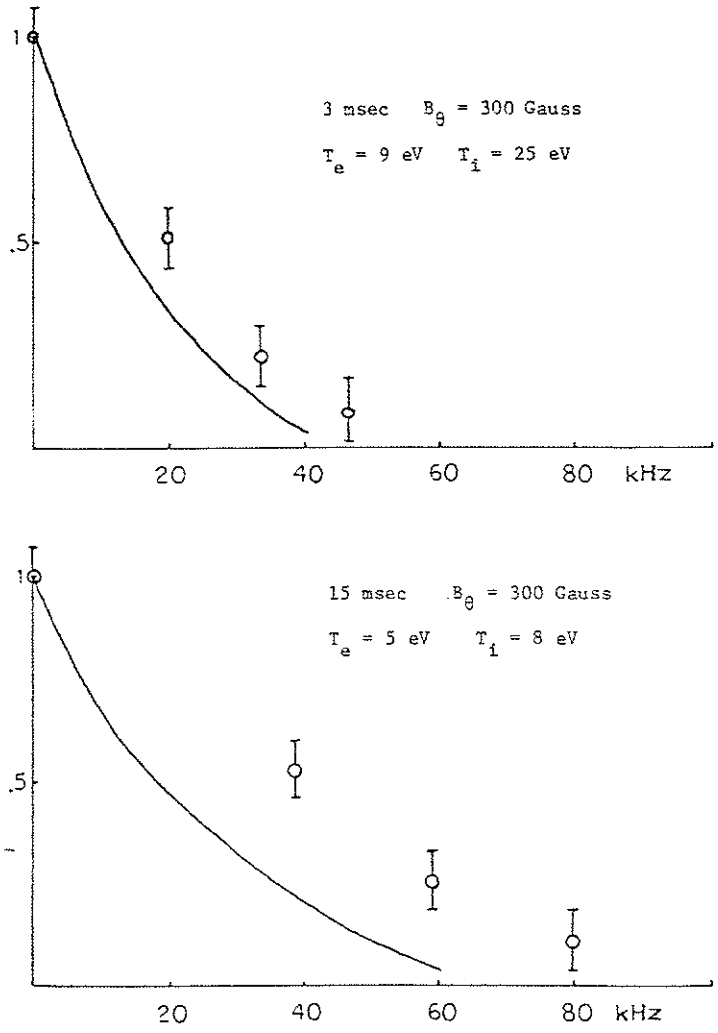

Figure 6

Little gun power spectra compared to Kadomtsev spectra

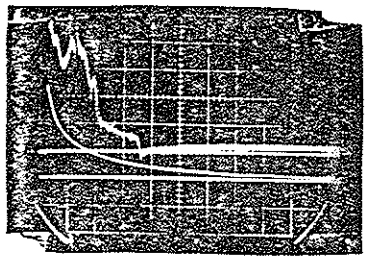

a. current density

300 Amp/m^2/div

2 msec/div

Midcylinder separatrix

gun inj. at 27 msec

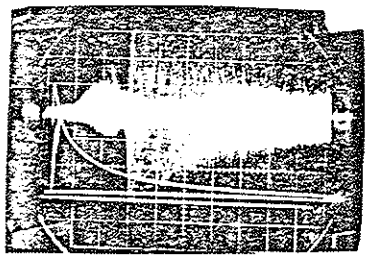

b. current fluctuations

2 msec/div

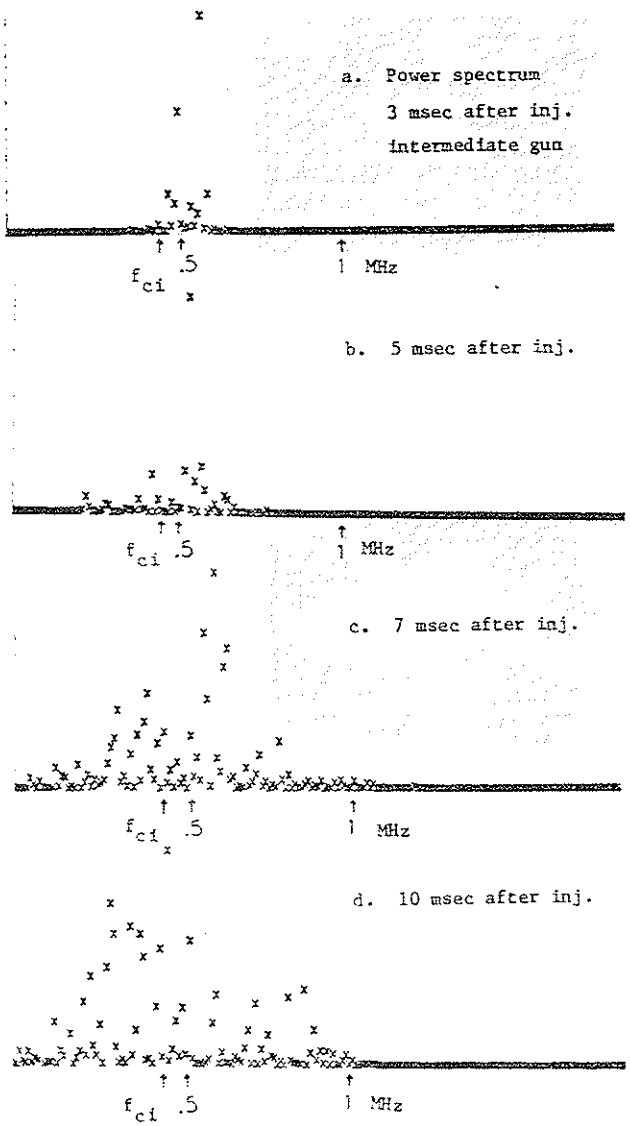

Figure 8

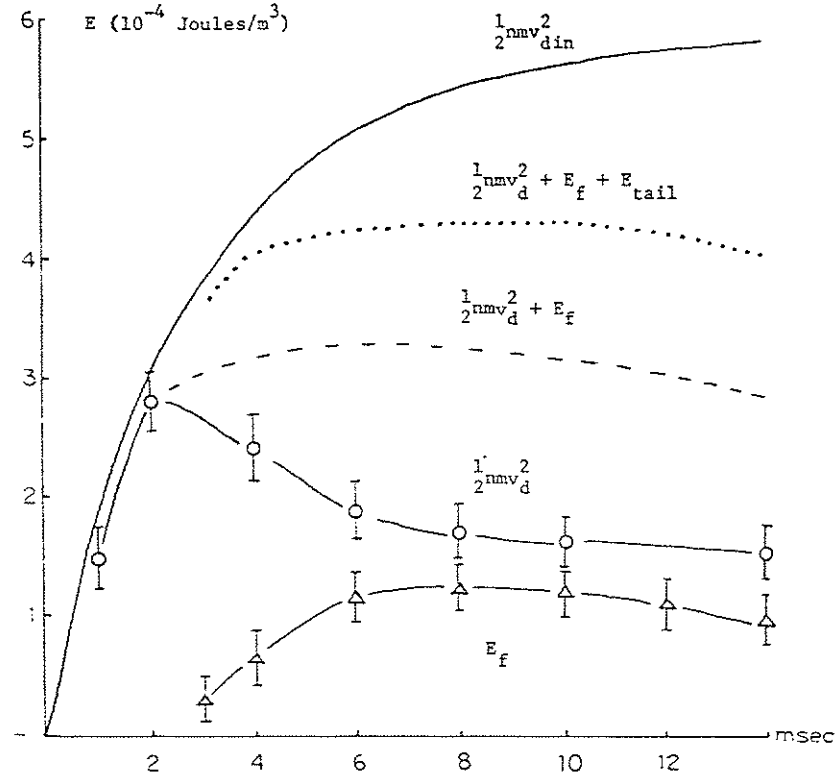

Figure 9

Energy balance in the intermediate gun plasma

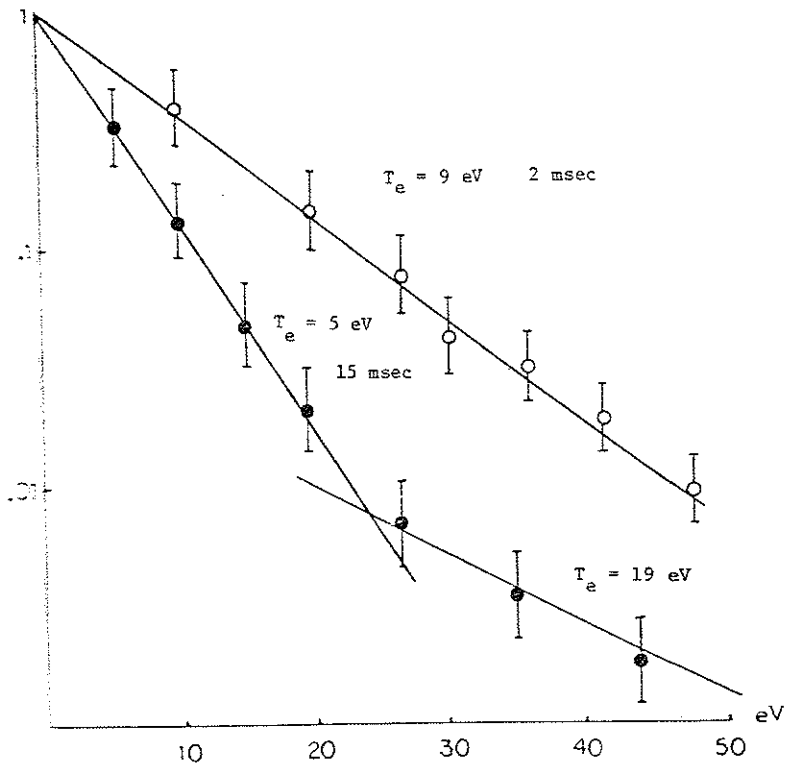

Figure 10

Electron velocity distribution for int. gun plasma

Chapter XI

Turbulent-mirror conductivity

A. Summary

Figure 1 summarizes the results obtained for the conductivity of the three plasma sources. Resistivity is plotted versus collision frequency. The collision frequency is normalized to the electron bounce frequency, ν_b, and is divided into 3 regimes of collisionality: collisional, transition, and collisionless.

In the collisional regime, mirror effects are not expected to play any part in determining the conductivity and Spitzer conductivity should hold. The resistivity of the big gun was indeed found to obey Spitzer resistivity, scaling like $(T_e)^{-3/2}$ and independent of density.

The collisionality of the intermediate gun is initially transitional and later becomes collisionless after the density decays. For the first 2 msec after injection the conductivity of the intermediate gun satisfies Spitzer conductivity with T_e = 5 eV although the electron temperature was determined to be 7 eV. Later in time the current density dropped abruptly and the resistivity was observed to scale like $\eta \propto \sqrt{T_e}/n$ which agrees with the transitional resistivity scaling.

The little gun plasma is collisionless and mirror effects are expected to have a significant effect on the conductivity. Mirror trapping reduces the number of circulating particles and should cause an enhanced resistivity

$$\eta_{mirror} = \left(\frac{\pi/2}{\theta_{\ell c}}\right) \frac{\eta_{Sp}}{f_{ut}} \qquad \text{XI-1}$$

The little gun resistivity was determined to scale like $\eta \propto \sqrt{T_e}/n_e$ which does not agree with the prediction of eqn. 1

Figure 2 illustrates resistivity scaling versus density for the little gun and intermediate gun plasmas. Lencioni[1] and Etzweiler[2] resistivity scaling is also indicated. They observed resistivity in the little octupole to scale like $\eta \propto \sqrt{T_e}/n$ but a factor of 2 to 3 greater in magnitude than the large octupole resistivity. Also plotted are resistivity values for Spitzer, mirror and two turbulent resistivity predictions. The Buneman resistivity occurs when the electron-ion two stream instability is excited. As discussed in section VIII-I the directed electron energy is dissipated into random energy by interactions with the fluctuating fields. Buneman gives the conductivity value as

$$\sigma = \frac{1}{2}\left(\frac{M}{m}\right)^{1/3} \omega_{pe} \qquad \text{esu} \qquad \text{XI-2}$$

This value is plotted in Figure 2. The resistivity scaling is $\eta \propto n^{-1/2}$ and is 2 to 3 orders of magnitude higher than the experimentally observed values. The two stream instability is only excited when $u_d > v_e$. Drift velocities of this magnitude were not observed and the two stream instability is not expected to play a role in the conductivity.

Sagdeev resistivity[4] is predicted to occur when the ion acoustic instability is excited. The dynamic friction force acting on electrons in the presence of the ion acoustic instability is

$$\frac{nmu}{\tau_{eff}} = \frac{\partial}{\partial t}\int mv f_e dv = \int mv S(f_e) dv \qquad \text{XI-3}$$

where τ_{eff} is the effective scattering time, f_e is the electron distribution function and S is a collision operator which has the form

$$S(f) = \frac{e^2}{m^2}\frac{\partial}{\partial \vec{v}}\cdot\Sigma\,\vec{K}\left(\frac{\vec{K}}{K^2}\cdot\frac{\partial}{\partial \vec{v}}\right)\delta(\omega - \vec{K}\cdot\vec{v})\,|E_k|^2 \qquad \text{XI-4}$$

where K is the wave number and E_k is the energy in the k mode. Eqn. 4 is difficult to solve but a quasi-linear approach leads to a kinetic equation for N_k, the wave spectrum

$$2\nu_k N_k + \frac{\omega_{pi}^2}{\omega^2}\frac{T_i T_e}{(enm_i)^2} N_k S(f) = 0 \qquad \text{XI-5}$$

Eqn. 5 can be solved for S(f) and thus τ_{eff} if N_k and ν_k are known. ν_k is the growth rate of the mode and is approximated by

$$\nu_k \simeq \nu = \frac{T_i}{2}\frac{\omega_{pi}^2\omega}{K^2}\frac{\partial f}{\partial v}\Big|_{v=\omega/K} \simeq \omega\frac{u_d}{v_e} \qquad \text{XI-6}$$

$\nu < \omega$ is required in order for eqn. 6 to be a good approximation. Sagdeev obtains for τ_{eff} due to ion acoustic instability

$$\tau_{eff} = 10^2\frac{T_i}{T_e}\frac{c_s}{u_d}\frac{1}{\omega_{pi}} \qquad \text{XI-7}$$

where c_s is the ion acoustic velocity and u_d is the electron drift velocity due to a parallel electric field. Experimental values of τ_{eff} have been found which are in agreement with eqn. 7. The factor of 10^2 in eqn. 7 is only approximate and experimental values range from 10^2 to 10^3 depending on the apparatus.[5,6]

Sagdeev resistivity is obtained from

$$\eta = \frac{m}{ne^2\tau_{eff}} = \frac{m}{ne^2} 10^{-2} \frac{T_e}{T_i} \frac{u_d}{c_s} \omega_{pi} \qquad \text{XI-8}$$

This resistivity is plotted in Figure 2 and is seen to scale like $\eta \propto n^{-1/2}$. The magnitude is a factor of 2 to 20 greater than the experimental values but if the factor 10^3 is used in eqn. 7 the magnitudes agree well except for the different scaling with density.

Sagdeev resistivity was derived for a plasma in a homogeneous magnetic field and thus takes no account of mirror effects. If eqn. 7 is solved for ν_{eff} the following table is obtained.

Table XI-1

$n(cm^{-3})$	ν_{eff}	ν_b (T_e = 10 eV)	$\nu_{\ell c} = (\pi/2\theta_{\ell c})^2 \nu_{eff}$
10^8	5×10^5 sec^{-1}	2×10^6 sec^{-1}	$10^6 - 10^7$ sec^{-1}
10^{10}	5×10^6 sec^{-1}	2×10^6 sec^{-1}	$10^7 - 10^8$ sec^{-1}

ν_b is comparable or greater than ν_{eff} from $n = 10^8$ cm^{-3} to $n = 10^{10}$ cm^{-3} and thus mirror effects must be taken into account when considering the Sagdeev conductivity since the value of the conductivity depends on the scattering process with the highest frequency. In particular, the table shows that the conditions for transition resistivity are satisfied

$$\nu_{eff} < \nu_b < \left(\frac{\pi/2}{\theta_{\ell c}}\right)^2 \nu_{eff} \qquad \text{XI-9}$$

This leads us to the definition of turbulent-mirror conductivity (as opposed to Spitzer-mirror conductivity) which may be a possible explanation of the $\eta \propto \sqrt{T_e}/n_e$ scaling where Spitzer-mirror conductivity is expected. ν_{ei} due to electron-ion collisions is very low and is replaced by ν_{eff} from eqn. 7. The enhanced resistivity can be explained in either of two complementary ways:

(1) Electron interactions with current driven turbulence cause the electrons to undergo small angle scattering. In a homogeneous magnetic field a resistivity similar to that given in eqn. 8 would be expected. The presence of mirrors enhances the resistivity since a small angle scatter into the trapped region of phase space is equivalent to a 90^0 scatter.

(2) The presence of the instability enhances the role of the mirrors. The small angle scattering due to the instability opens up a larger portion of phase space to the mirror effects.

Either of the two explanations leads to a turbulent-mirror resistivity scaling like transitional resistivity $\eta \propto \sqrt{T_e}/n_e$ for the frequencies listed in Table XI-1.

The above arguments are based on τ_{eff} derived for current driven ion acoustic turbulence. The fluctuations actually seen in the electron current corresponded to ion cyclotron instability and a current driven drift wave. However, all of the arguments leading up to eqns. 7 & 8 were based on quasilinear effects, e.g. plateau formation in the electron distribution, wave-wave scattering, and wave-particle scattering. All of these processes occur in ion cyclotron modes. Also, the condition

for eqn. 6 to hold is satisfied for the ion cyclotron instability.[7]

$$\gamma < \omega_{ci} \frac{u_d}{v_e} \qquad \text{XI-10}$$

Thus, τ_{eff} for current driven ion cyclotron instability is not expected to differ much from eqn. 7.

Experimental evidence for the validity of turbulent-mirror resistivity is as follows:

(1) Experimental resistivity at low plasma densities is observed to scale like $\eta \alpha \sqrt{T_e}/n_e$ in contradiction to the expected mirror scaling

$$\eta_{mirror} = \left(\frac{\pi/2}{\theta_{\lambda c}}\right)^2 \frac{\eta_{Spitzer}}{f_{ut}}$$

(2) Fluctuations in the electron current were observed when the anomalous resistivity was seen.

(3) u_d/v_{thi} and T_e/T_i satisfied the conditions for excitation of current driven ion cyclotron modes.

(4) A high energy tail was observed in the electron distribution. This tail can be explained in terms of particle heating due to the formation of a plateau.[5]

References for Chapter XI

1. D. E. Lencioni, Univ. of Wisc. Ph.D. Thesis, PLP 276 (1969)
2. J. F. Etzweiler, Univ. of Wisc. Ph.D. Thesis, PLP 738 (1977)
3. O. Buneman, Phys. Rev., 115,503(1959)
4. R. Z. Sagdeev, Symp. Appl. Math., 18,281(1965)
5. J. Scharer, et. al., Association Euratom-C.E.A. EUR-CEA-FC-545 (1970)

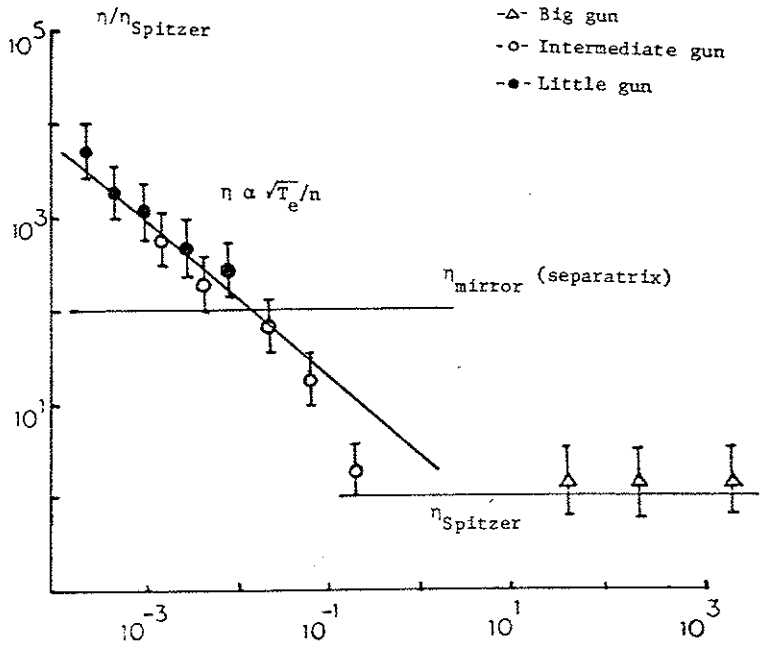

Collisionless

$\nu_b > \nu_{\lambda c}$

$\eta = \left(\frac{\pi/2}{\vartheta_{\lambda c}}\right)^2 \frac{\eta_{Spitzer}}{f_{ut}}$

Transition

$\nu_{ei} < \nu_b < \nu_{\lambda c}$

$\eta = \frac{m_e \nu_e}{e^2 n_e} \frac{1}{L_m} \alpha \sqrt{T_e}/n$

Collisional

$\nu_b < \nu_{ei}$

$\eta = \eta_{Spitzer}$

Figure XI-1

Resistivity scaling versus collisionality

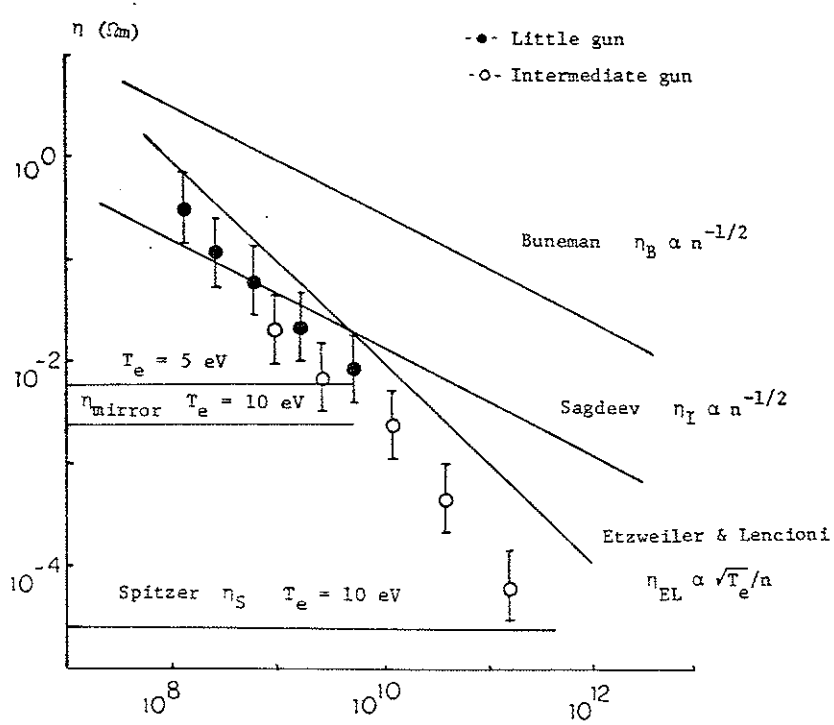

Figure XI-2

Resistivity scaling versus density

Appendix

Data Analysis

Figure 1 illustrates the data taking system used on the octupole. Fluctuation data obtained from probes are filtered and amplified by the Tektronix 501 module. The signal is amplified to the proper level by the op amp buffer circuit in front of the Camac modules. Three Camac modules were equipped with Lecroy 2256 waveform analyzers. 1024 samples with 8 bit accuracy can be obtained. The fastest sampling period is $T = 50$ nsec. The digitized signal is read out of the buffer memory by the PDP-11/20 computer and is stored in core memory. A number of things can now be done with the digitized signal.

1) The raw data signal can be stored on a floppy disk.
2) The data can be analyzed: An autocorrelation can be performed on the signal followed by an FFT to give the power spectrum. A cross correlation can be performed on two signals from probes at different positions in the octupole.
3) The analyzed data can be displayed on the CRT or plotted on the xy plotter.

Nyquist sampling rate: A signal to be digitized is composed of frequencies from $f = 0$ to $f = f_m$, where f_m is the highest frequency component of the signal. The Nyquist sampling theorem states that aliasing can be avoided if the sampling rate T is chosen such that

$$T < \frac{1}{2f_m}$$

e. g. if $f_m = 10$ MHz then $T < 50$ nsec. Conversely, if the fastest sampling rate of the ADC is T seconds then the input signal to the ADC must be filtered so that it contains no components with frequencies higher than $f_m = (2T)^{-1}$. The fastest sampling rate on the Lecroys was $T = 50$ nsec so that $f_m = 10$ MHz.

Leakage: Leakage is illustrated in Figure 2. A periodic waveform in a) is sampled and the digitized sample illustrated in d) is stored in the computer memory. The FFT calculation requires a periodic signal. This is obtained by repeating the sample as illustrated in e). Discontinuities cause sidelobes to appear in the power spectrum. This is referred to as leakage. The sidelobes are an effect of the sampling and do not correspond to any frequency components in the input signal to the ADC. The discontinuities result in the appearance of high frequency components in the power spectrum in order to build up the steps. The discontinuities may also result in a DC component if the signal no longer averages to zero. There are several ways to reduce the leakage.

1) Make sure the sample contains an integer number of wave periods. Experimentally this is difficult to achieve. The phase of the sample at the beginning and end of the sample window will vary and one will need to reject a majority of the data before matching phases are found.

2) Average the autocorrelation over a number of shots. In this way the phase difference will average to zero.[1]

3) Multiply the sampled data by a Hanning function.[2] The Hanning function forces the phases to match at the beginning and end of the

sample window.

Correlation function:

The correlation function is defined as the time average of the product of two signals.

$$C(f,g,\tau) = \lim_{T\to\infty} \frac{1}{T} \int_{-T/2}^{T/2} f(t)g(t-\tau)dt \qquad A\text{-}1$$

If the signals are digitized the digital equivalent of eqn. 1 is

$$C(f,g,\tau) = \frac{1}{n-m} \sum_{k=0}^{n-m} f_k g_{k+\tau} \qquad A\text{-}2$$

where n is the number of sample points and n-m is the correlation window with $m < n$.

If $f = g$ then $C(f,f,\tau)$ is the autocorrelation of a signal. The Weiner-Khinchin theorem[3] states that the power spectrum is the Fourier transform of the autocorrelation

$$\tilde{C}(\omega) = \int_{-\infty}^{\infty} C(f,f,\tau)e^{i\omega\tau}\, d\tau \qquad A\text{-}3$$

If f and g are different (e.g. signals from different positions) then $C(f,g,\tau)$ is the cross correlation function and $\tilde{C}(\omega)$ is the cross spectral power density. Any random fluctuations not common to both f and g average to zero and only common frequencies show up in $\tilde{C}(\omega)$.

Some of the commonly observed correlations and power spectra are illustrated in Figure 3. These illustrations are familiar to anyone who has examined a table of Fourier transforms. Figure 3a illustrates a perfectly correlated sine wave. Neither the amplitude of the wave

nor the frequency change in time. The power spectrum shows that all the power occurs at frequency ω_o.

Figure 3b illustrates a wave which decorrelates after a certain time. The decorrelation time T is the time at which $C(f,f,\tau)$ falls to 1/e of its value at $\tau = 0$. The autocorrelation function is always maximum at $\tau = 0$. The power spectrum is broadened with $\Delta\omega \approx 1/T$. Thus the decorrelation time is related to the width of the power spectrum. The broadening of the power spectrum (and hence the decorrelation time) are often caused by turbulent processes in a plasma and for a given instability the broadening can be predicted.

Figure 3c illustrates the autocorrelation and power spectrum of broadband noise. The noise quickly decorrelates to zero in a time T. Most of the power in the power spectrum occurs at frequencies less than T^{-1}.

Figure 3d shows the autocorrelation of a sine wave signal with broadband noise added to it. In all likelihood one would not be able to look at the raw data signal and tell that it contained a pure sine wave buried in all the noise. The pure sine wave is easily seen in the autocorrelation. The broadband noise decorrelates to zero in a time T and the sine wave is the only signal remaining. The power spectrum shows power in the low frequencies $< T^{-1}$ corresponding to the noise and a spike at ω_o corresponding to the sine wave.

As a final example, Figure 4 illustrates the cross correlation of two signals containing a fundamental frequency and one harmonic. Signal 1 is given by

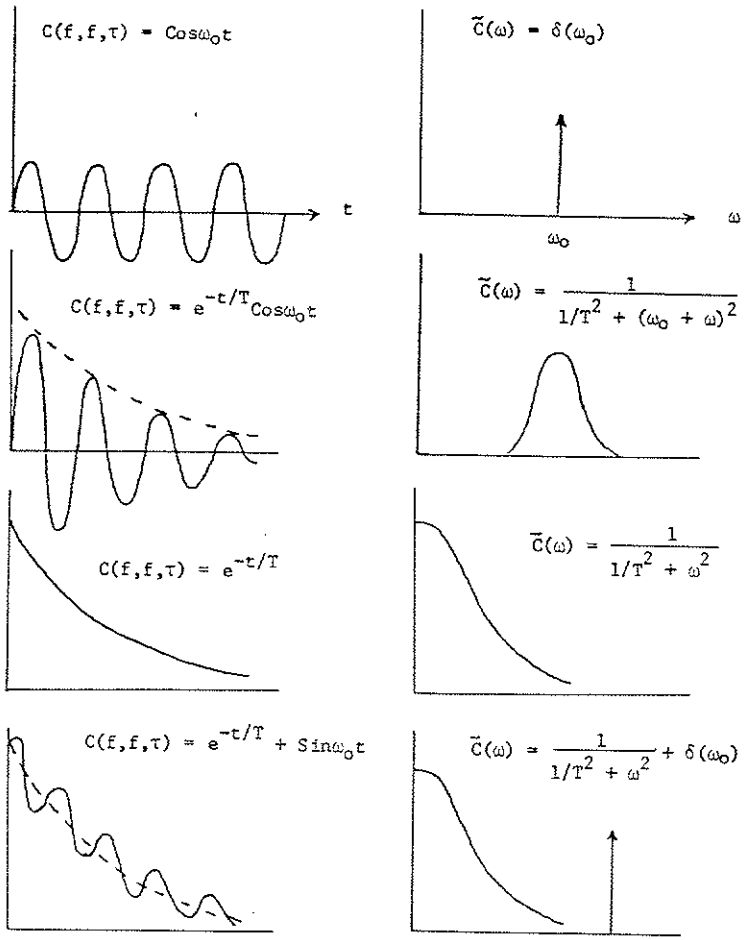

Figure A-3

Examples of autocorrelation functions and power spectra

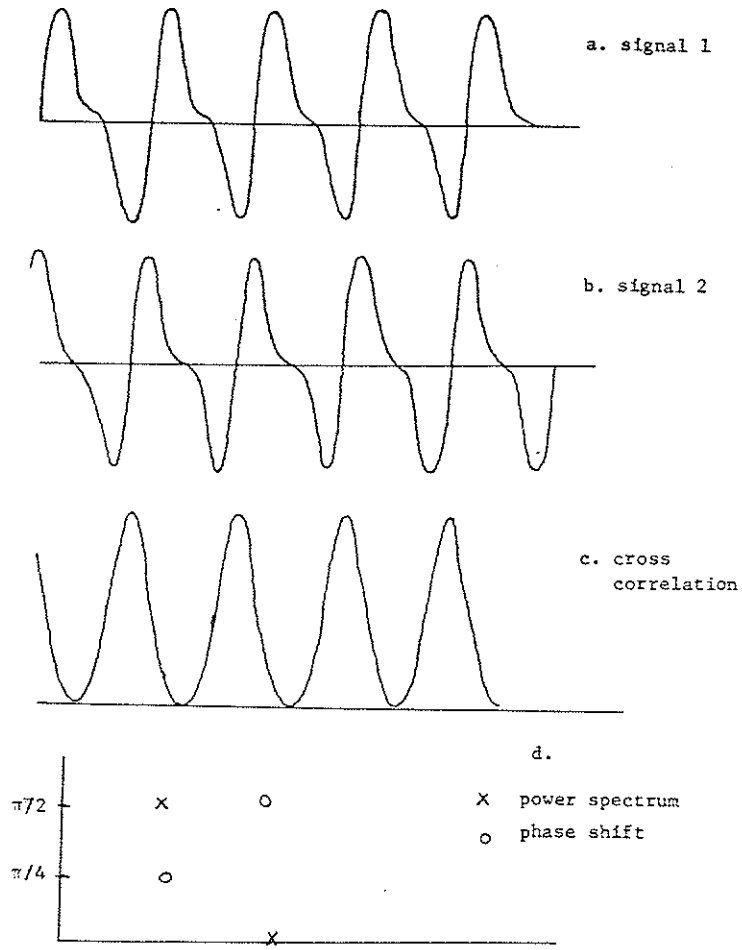

Figure A-4

Cross correlation of two signals